UNIVERSITÉ DU QUÉBEC À MONTRÉAL

SYNTHÈSE DE MATÉRIAUX À BASE DE CARBONE ET DE PHOSPHAZÈNE COMME RETARDATEUR DE FLAMMES ET SUPERCONDENSATEURS

THÈSE

PRÉSENTÉE

COMME EXIGENCE PARTIELLE

DU DOCTORAT EN CHIMIE

PAR

KHALED RHILI

FÉVRIER 2024

UNIVERSITÉ DU QUÉBEC À MONTRÉAL
Service des bibliothèques

Avertissement

REMERCIEMENTS

Cette thèse est la synthèse de mes travaux de recherche effectués au sein de l'Université du Québec à Montréal dans le département de Chimie-Biochimie. Durant cette période j'ai pu renforcer mes connaissances, tant sur le plan professionnel que personnel, j'ai collaboré avec plusieurs personnes que je tiens à remercier.

En premier lieu, j'exprime ma sincère gratitude à mon directeur de recherche, le Professeur Mohamad Siaj, qui m'a patiemment guidée et assistée tout au long de mes études à l'UQAM. Merci de m'avoir fait confiance. Je suis honorée, d'avoir été supervisée par un professeur spécialisé dans plusieurs domaines et qui possède un immense savoir scientifique.

Également, je tiens à remercier le Dr Rami Abdelhaq pour ses précieux conseils, sa patience et ses encouragements à poursuivre jusqu'à la réussite.

J'exprime ma gratitude au Professeur Ahmad Samih ElDouhaibi de la faculté de science à Liban pour ses conseils et ses savoirs qui ont permis de mener à bien une collaboration fructueuse.

Je remercie les membres du jury d'évaluation de ma thèse, le Pr. Ricardo Izquierdo, le Pr. David Dewez et le Pr. Rafik Naccache.

J'aimerais remercier mes collègues du laboratoire du Pr Siaj ; Dre Siham, Thai, Dr Hassan, Amir, Hichem, Zhiyuan, Maziar, Abeer et Issa. Merci aussi à tous les techniciens et techniciennes de laboratoire, merci au service de caractérisation, particulièrement à Gwenaël Chamoulaud et à Galyna Shul pour leurs orientations.

Je remercie les employées et les employés du magasin de chimie et de l'administration, Pascale Beauchemin et Élisabeth Lindsay de la Faculté des sciences.

Mes remerciements chaleureux les plus sincères vont à ma famille bien-aimée qui a toujours cru en moi, m'a encouragée et qui a été toujours à mes côtés. J'ai obtenu ce doctorat grâce à l'amour et au soutien de ma famille. Ma très chère maman, mon très cher défunt papa, mes frères et mes sœurs, mes neveux ; un très grand merci et une gratitude infinie. Sincères remerciements à une personne chère, Siham Chergui pour son soutien, sa patience et ses encouragements tout au long de mon doctorat.

DÉDICACE

Tous les mots ne sauraient exprimer la gratitude, l'amour, le respect et la reconnaissance de mes chers parents

À ma très chère mère

Autant de phrases aussi expressives soient-elles ne sauraient montrer le degré d'amour et d'affection que j'éprouve pour toi. Tu m'as comblé avec ta tendresse et affection tout au long de mon parcours. Tu n'as cessé de me soutenir et de m'encourager durant toutes les années de mes études, tu as toujours été présente à mes côtés pour me consoler quand il fallait. En ce jour mémorable, pour moi ainsi que pour toi, reçoit ce travail en signe de ma vive reconnaissance et ma profonde estime.

Que Dieu, le tout puissant, t'accorde une longue vie et surtout une très bonne santé et te garde pour nous.

À la mémoire de mon très cher père

Je dédie ce travail marquant de ma vie à la mémoire de mon père disparu trop tôt. J'espère qu'il apprécie cet humble geste comme preuve de reconnaissance de la part d'un fils qui a toujours prié pour le salut de son âme. Espérant très cher papa que tu es fier de moi.

Je prie le bon Dieu de te garder dans son vaste paradis.

TABLE DES MATIÈRES

LISTE DES FIGURES

LISTE DES TABLEAUX

ABRÉVIATIONS

RF	Retardateurs de flamme
CO	Monoxyde de carbone
HCN	Cyanure d'hydrogène
PCB	Polychlorobiphényle
ATH	Trihydroxyde d'aluminium
MDH	Hydroxyde de magnésium
TBBA	Tetarbromobisphénol-A
PBDE	Polybromodiphényléther
ALOOH	Boehmite
SiO_2	Dioxyde de silicium
TiO_2	Dioxyde de titane
Al_2O_3	Alumine
Fe_2O_3	Oxyde de fer
H_2O	Eau
DI	Eau déionisée
H_3PO_4	Acide phosphorique
HCl	Acide Chlorhydrique
$KMnO_4$	Permanganate de potassium
H_2O_2	Peroxyde d'hydrogène
CO2	Dioxyde de carbone
K_2CO_3	Carbonate de potassium
NH_3	Ammoniac

RoHS	Restriction of the use of certain hazardous substances in electrical and electronic equipment
REACH	Registration, Evaluation, Authorisation and Restriction of Chemicals
SC	SC supercondensateur
EDCL	Double Couche Électrochimique
PPE	Polypropylène
OG	Oxyde de graphène (Graphene oxide)
rGO	Oxyde de graphène réduit (Reduced graphene oxide)
PN-rGO	Oxyde de graphène réduit co-dopé phosphore/ azote
FGO	Oxyde de graphène fonctionnalisé
HCCP	Hexachlorocyclotriphosphazène
TEA	Triéthylamine
C-PPZs	Cyclomatrix-polyphosphazenes microspheres
POPs	Amorphous porous organic polymers
CVD	Dépôt chimique en phase vapeur
CV	Voltamétrie cyclique
GCD	Galvanostatic charge/discharge
EIS	Spectroscopie d'impédance électrochimique
R_{ct}	Résistance de transfert de charge
R_s	Résistance à la solution
Ag/AgCl	Silver chloride electrode
PMMA	Polyméthacrylate de méthyle
KOH	Hydroxyde de potassium
p-PDA	*p*-Phénylèndiamine
EP	Résine époxy
m-PDA	*m*-Phénylènediamine
DGEBA	Éther diglycidylique de bisphénol-A

RMN	Magic angle spinning
MAS	Milieu de culture Luria-Bertani
MEB	Microscope électronique à balayage
TEM	Microscopie électronique à transmission
XPS	Spectroscopie de rayons X à dispersion d'énergie
DRX	Diffraction des Rayons X
EDX	Spectroscopie de rayons X à dispersion d'énergie
AFM	Microscope à force atomique
FT-IR	Spectroscopie infrarouge à transformée de Fourier
MEB	Macroscopie à balayage
ATG	Analyse thermogravimétrique
$Ni (OH)_2$	Hydroxyde de nickel (II)
$([PCl_2N]_3)$	Cyclic polyphosphazene
Cl	Chlore
N	Azote Oxyde de graphène
P	Phosphore
B	Bore
S	Soufre

SYMBOLES ET UNITÉS

L	Litre
u.a	Unité Arbitraire
2D	Bidimensionnel
E	Énergie
A	Ampère
cm^2	Centimètre carré
ΔV	Différence de potentiel
Δt	Discharge time
Hr	Heure
Hz	Hertz
S	Seconde
F	Farad
Min	Minute
Ml	Millilitre
mV	Millivolt
$mV\ s^{-1}$	Millivolt par seconde
Nm	Nanomètre
nM	Nanomolaire
Nmol	Nanomole
G	Gramme
C	Capacitance
W·h/kg	Wattheure par kilogramme
I	Courant

M	Masse
V	Voltage
eV	Electronvolt
Ω	Ohm
o	Degré
ºC	Degré Celsius
%	Pourcentage

RÉSUMÉ

Dans ce travail de recherche, nous avons synthétiser et fonctionnaliser des matériaux 2D à base de l'oxyde de graphène (OG), de l'hexachlorocyclotriphosphazène (HCCP) et du *p*-Phénylèndiamine (*p*-PDA) en tant que retardateur de flamme (RF) et en tant que supercondensateurs à haute performance. En effet, les RF sont des composés chimiques utilisés dans les polymères. Étant donné leurs ignifugations, ils sont utilisés dans le mobilier et les composés électroniques pour prévenir et empêcher la propagation de l'incendie. Les polymères ou les monomères réactifs à base de phosphazène sont ignifugeants, grâce à la présence des éléments P et N. Ils peuvent être employés seuls ou être ajoutés en masse aux polymères commerciaux courants, pour augmenter leur stabilité thermique et le retardement de flamme. De plus, le dopage de l'oxyde de graphène réduit par l'azote et le phosphore (P, N-rGO) permet la conception de supercondensateur à haute performance. Les supercondensateurs sont des dispositifs de stockage possédant une densité de puissance importante de l'ordre de plusieurs kW/kg.

Dans ce sens, une synthèse d'un retardateur de flamme à base OG fonctionnalisé avec le (HCCP) et de la (*p*-PDA) a été réalisée avec succès. L'oxyde de graphène fonctionnalisé (FGO) a démontré une efficacité en tant que retardateur de flamme. L'analyse thermogravimétrique a démontré que l'ajout d'HCCP à l'OG lui permet une grande stabilité thermique et une meilleure résistance à la température ce qui lui confère une application comme retardateur de flamme. Le FGO obtenu a été incorporé dans la résine époxy pour former des composites. Les propriétés ignifuges, le comportement de dégradation thermique et la combustion des composites ont été étudiés par TGA et par une flamme de brûleur Bunsen.

La synthèse de l'OG utilisé dans la première partie de cette thèse a été réalisée par la méthode d'Hummers modifiée. L'OG obtenu a été caractérisé par différentes techniques spectroscopiques et d'imageries, telles que la microscopie à force atomique (AFM), la microscopie électronique à transmission (MET), la microscopie électronique à balayage (MEB), la spectrométrie de résonance magnétique nucléaire de l'état solide du carbone -13 (^{13}C-ES-RMN), la spectroscopie de Raman, la spectroscopie infrarouge à transformée de Fourier (FT-IR), la spectroscopie de photoélectrons induits par rayons X (XPS) et l'analyse thermogravimétrique (ATG).

Deuxièmement, une synthèse des matériaux carbonés poreux à dopage multiples d'hétéroatomes (l'azote et le phosphore) pour la conception des électrodes de supercondensateurs. Les matériaux synthétisés qui présentaient une surface spécifique enlevée ont été évalués en utilisant la voltamétrie cyclique (CV) à différentes vitesses de balayage potentielles et des essais de charge / décharge galvanostatiques (GCD) à différentes densités de courant.

Cette thèse a permis de développer une approche pour préparer des matériaux à base de carbone et des hétéroatomes pour une utilisation en tant que retardateurs de flammes et comme des électrodes pour supercondensateurs.

Mots clés: Oxyde de graphène, hexachlorocyclotriphosphazène, dopage, matériaux 2D, retardateurs de flamme, supercondensateurs.

CHAPITRE I

INTRODUCTION GÉNÉRALE

Dans ce chapitre, une introduction générale sur la synthèse des matériaux à base de carbone dopé via des hétéroatomes (N/P/O), des retardateurs de flamme et des supercondensateurs a été présentée. Étant donné que l'oxyde de graphène présente une surface spécifique élevée, des groupes fonctionnels oxygénés jumelés avec une excellente stabilité chimique, il a été utilisé comme substrat prometteur pour la fonctionnalisation et le dopage.

1.1   Matériaux à base de carbone

Le carbone est le quatrième élément le plus abondant dans l'univers après l'hydrogène, l'hélium et l'oxygène. Il est présent sur Terre à l'état de corps simple (charbon et diamants), de composés inorganiques (CO_2). Le carbone a toujours joué un rôle déterminant dans l'évolution de la société humaine. En effet, l'histoire de l'humanité ne pourrait pas être écrite sans parler du carbone. Néanmoins, c'est un des éléments les plus importants. Le carbone se trouve sur la deuxième ligne et à la sixième colonne et dans la classification périodique de Mendeleïev et porte le numéro atomique Z=6. Sa configuration électronique est donc $1s^2 2s^2 2p^2$. Il possède six électrons, dont quatre sur sa couche de valence. Cependant, le carbone est souvent retrouvé sous forme hybridée. Ainsi, sa structure peut être différente d'une hybridation à une autre. Ces différentes hybridations lui permettent d'exister sous différentes formes allotropiques à l'état

naturel. Les formes naturelles les plus connues du carbone sont le carbone amorphe (Jenkins 1973), le graphite (Sparavigna 2018) et le diamant (Meyer, Geim et al. 2007) (figure 1.1). Les scientifiques ont cependant réussi à mettre en évidence de nouvelles formes de carbone : les fullerènes (Kroto, Heath et al. 1985), les nanotubes de carbone (Iijima 1991) et la récente découverte le graphène qui n'existent pas à l'état naturel (Wallace 1947, Marcano, Kosynkin et al. 2010). Ces allotropes de carbone par leurs propriétés électriques et leur résistance mécanique élevées, ainsi que pour leur stabilité chimique ont fait l'objet de très nombreuses études, autant dans le domaine fondamental que celui appliqué. La découverte de matériaux avec de nouvelles propriétés, ne cessent de croitre et cela le but de révolutionner le monde des technologies.
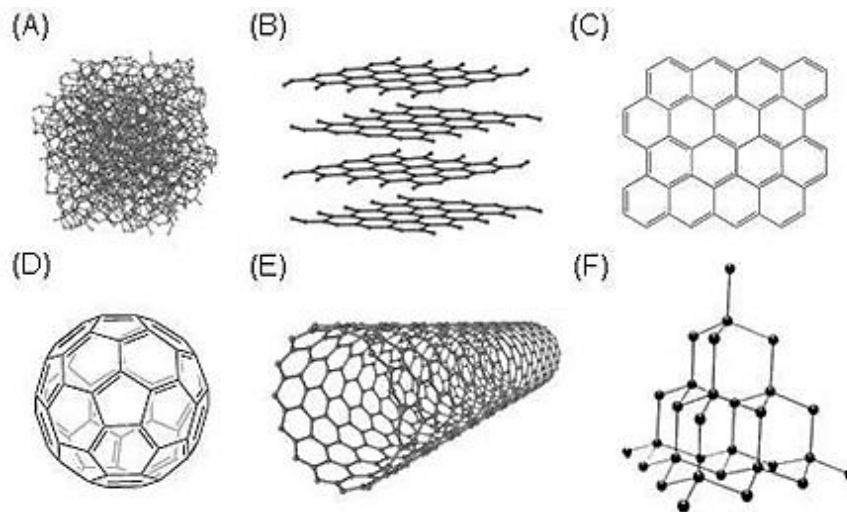
Figure 1.1   Allotropes du carbone: (A) carbone amorphe, (B) graphite, (C) graphène, (D) fullerène (C60), (E) nanotube de carbone et (F) diamant (Tiwari, Kumar et al. 2016)

1.2 Oxyde de graphène (OG)

L'oxyde de graphène (OG) est l'un des derniers nés de cette lignée d'allotropes de carbone qui a été relativement négligé, sauf comme intermédiaire pour produire du graphène par exfoliation chimique à partir du graphite.

D'après le modèle de Lerf, la structure de l'OG se compose d'un réseau hexagonal en nid d'abeilles (figure 1.2) à base de carbone, ayant à la fois des atomes de carbone hybridés sp2 et d'atomes de carbone hybridés sp3. Il possède de nombreuses fonctions oxygénées sous forme hydroxyle et époxyde sur le plan basal des feuillets de graphène, ainsi que de groupements carbonyles et carboxyles sur le bord des feuilles fait de ce matériau un réactif potentiel pour nombreuses applications chimiques.
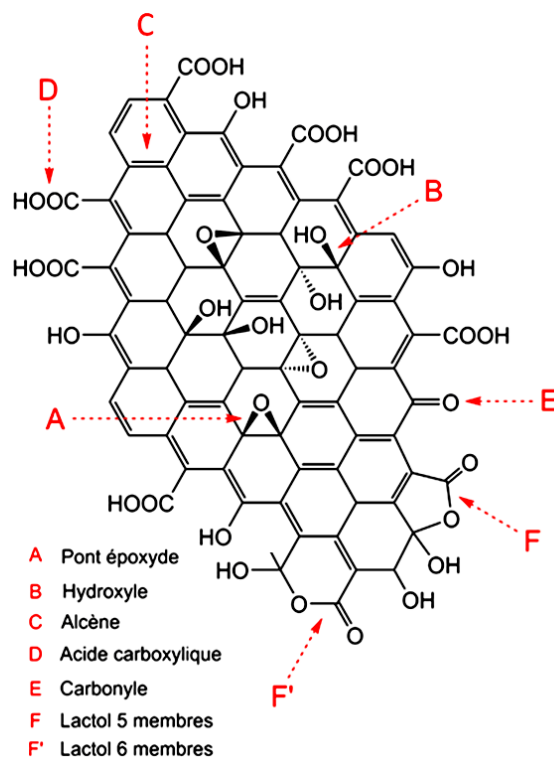
Figure 1.2   Structure de l'oxyde de graphène selon le modèle le plus récent de Lerf-Klinowski incluant les modifications apportées par Gao et ses collaborateurs (Brisebois and Siaj 2020)

L'oxyde de graphène est électriquement isolant et chimiquement actif en raison de la présence de groupements fonctionnels oxygénés formés au cours de procédé d'oxydation de graphite. Ces fonctions oxygénées lui confèrent des propriétés amphiphiles, donc une dispersion facile dans l'eau et dans les solvants organiques (Bissessur and Scully 2007, Compton and Nguyen 2010), il présente un comportement de désactivateur de fluorescence envers les biomolécules qui pourrait être utilisé pour comprendre leur changement de dynamique au cours de l'interaction entre le système biomacromoléculaire et les surfaces de l'OG (Liu, Robinson et al. 2008, Wang, Li et al. 2011).

L'interaction non covalente telle que la liaison hydrogène, les forces de Van der Waals, la liaison cation-π et l'empilement π-π se produisant entre l'OG et les biomolécules pourraient être utilisées comme membrane sélective dans les techniques de séparation (Yang, Zhang et al. 2008, Lu, Yang et al. 2009, Chergui, Rhili et al. 2020). L'OG peut aussi être fonctionnalisé à l'aide de ces fonctions oxygénées pour d'autres applications comme la purification de l'eau (Chen, Feng et al. 2012) ou bien en tant que retardateur de flamme (Rhili, Chergui et al. 2021).

1.3   Différentes méthodes de synthèse de l'oxyde de graphène

L'histoire de l'oxyde de graphène s'étale sur une période de plus de 150 ans. En 1859, l'OG a été préparé par le chimiste Brodie ou il s'intéressait à la réactivité du graphite en utilisant le chlorate de potassium ($KClO_3$) dans l'acide nitrique fumant (HNO_3) comme réactif (Brodie 1859). Brodie avait déterminé par analyse élémentaire que le matériau obtenu après cette étape a une masse plus grande et est composé de carbone (C), d'hydrogène (H) et d'oxygène (O) avec un ratio environ de 61 : 2 : 37.

Près de 40 ans après la découverte de Brodie, Staudenmeier a reproduit la méthode Brodie, en y modifiant certains paramètres. Sa méthode consiste à ajouter le chlorate

de potassium lentement tout au long de la réaction pour éviter les dangers reliés à étape de réaction exothermique. Le mélange est maintenu sous agitation durant 1 semaine dans un milieu refroidi. Durant ce temps du dioxyde de chlore (ClO_2) se forme et est évacué à l'aide de gaz inerte (N_2). Contrairement à la procédure de Brodie il fit une réaction progressive. Ce qui permettait entre autres d'augmenter le taux d'oxydation des feuillets de graphite (Staudenmaier 1898).

La synthèse de Staudenmaier se trouvant être longue et dangereuse due à la libération gazeuse de NO_2 et/ou de N_2O_4 (vapeurs jaunâtres), Hummers et Offeman développèrent un processus alternatif de l'oxydation du graphite nature en utilisant un excès de permanganate de potassium et d'acide sulfurique en présence d'une petite quantité de chlorate de sodium à une température d'environ 45 °C durant 2H. (William, Hummers et al. 1958).

Plusieurs variantes de cette réaction ont été faites à partir de la synthèse de Hummers (figure 1.3). Ces variations impliquent le changement de stœchiométrie ou le changement d'un réactif.

Tableau 1.1   Sommaire des différentes méthodes de synthèses d'oxydation de graphite (Compton and Nguyen 2010)

Synthèse	Brodie	Staudenmaier-Hoffman	Hummers	Hummers modifié	Hummers améliorée
Réactifs	$KClO_3$ HNO_3	$KClO_3$ HNO_3, H_2SO_4	$3KMnO_4$ $0.5NaNO_3$, H_2SO_4	$6KMnO_4$ $0.5NaNO_3$, H_2SO_4	$6KMnO_4$ $1H_3PO_4$, $9H_2SO_4$

1.3.1   Synthèse de l'OG par la méthode d'Hummers modifiée

L'oxyde de graphène a été préparé selon la méthode de Hummers modifiée (Marcano, Kosynkin et al. 2010). Brièvement, 3 g de flocons de graphite ont été mélangés avec 360 ml de H_2SO_4 concentrés et 40 ml de H_3PO_4 à 85%. Puis, 18 g de permanganate de potassium ($KMnO_4$) ont été ajoutés progressivement sur une période de 10 minutes.

Le mélange réactionnel a été chauffé à 50 °C pendant 4 heures dans un bain-marie sous agitation constante. Quatre périodes d'ultrasonication de 15 min ont été appliquées à la solution pour une exfoliation *in situ* de l'oxyde de graphite. Ensuite, le mélange a été maintenu sous agitation à température ambiante. La solution a été neutralisée avec un mélange de glace et 10 ml de peroxyde d'hydrogène (H_2O_2 30%). Le H_2O_2 permet de convertir le permanganate de potassium résiduel et le MnO_2 formés par la réaction en $MnSO_4$, espèce soluble en solution. À cette étape, les particules d'OG sont de couleur jaune clair dans le mélange réactionnel, mais elles ne sont pas complètement exfoliées. Les impuretés métalliques contenues dans le matériel sont éliminées par lavages successifs avec de l'eau (250 mL), une solution de HCl 10% (250 mL) et de l'éthanol anhydre (2 x 250 mL). Chaque lavage a été maintenu sous agitation pour avoir une solution homogène. Après la dernière centrifugation, le matériau a été récupéré sous la forme d'un hydrogel de couleur orangée.

Finalement, 1 L de diéthyl éther (Et_2O) a été ajouté à l'hydrogel pour séparer les feuillets de l'OG sous agitation. Le matériel de couleur brunâtre est récupéré et séché à l'air, puis sous vide pendant 24 heures à 40 °C pour obtenir un mélange brut d'oxyde de graphène et d'oxyde de graphite. Finalement, le produit d'OG a été dilué dans de l'eau nanopure sous agitation pour avoir une concentration de 4 g/L et la solution a été stockée à température ambiante (figure 1.3).
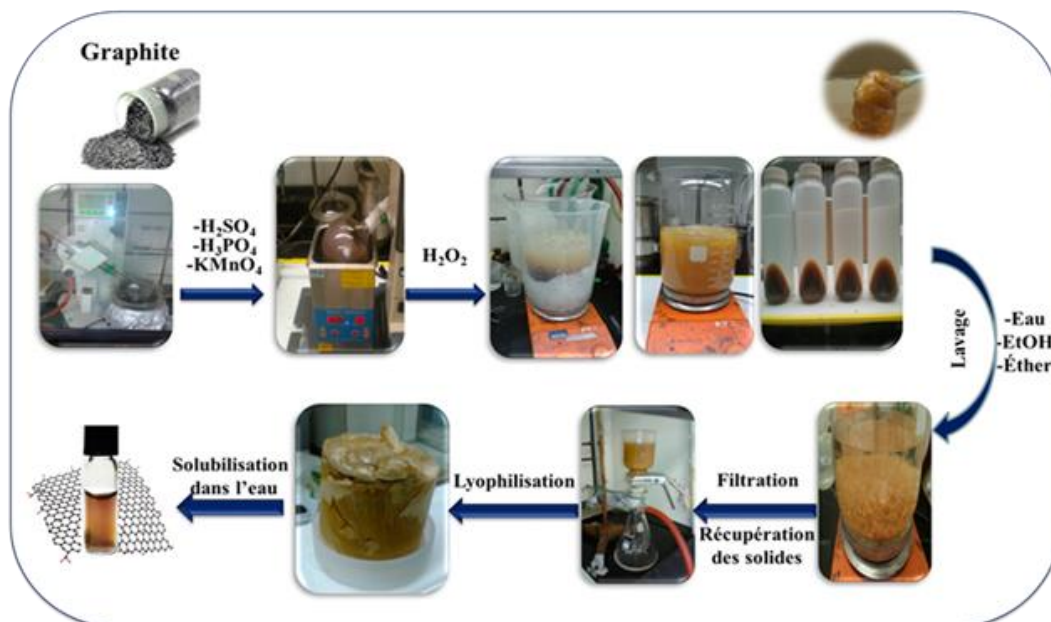
Figure 1.3   Différentes étapes de la synthèse de l'oxyde de graphène par la méthode de Hummers modifié (Chergui 2018)

1.3.2 Caractérisation de l'OG

1.3.2.1 Spectroscopie infrarouge à transformée de Fourier (FTIR) et RAMAN

Les groupes fonctionnels de l'OG sont étudiés par la spectroscopie FTIR. Le spectre FTIR de l'OG (figure 1.4a) possède plusieurs bandes d'élongations intenses associées aux étirements des fonctions hydroxyle à 3350 cm^{-1} (O-H), carbonyles à 1730 cm^{-1} (C=O), alcènes à 1608 cm^{-1} (C=C), et aux époxydes à 1027 cm^{-1} (C-O).

Le spectre Raman de l'OG (figure 1.4b) montre deux pics à 1345 cm^{-1} et 1584 cm^{-1}, correspondants aux bandes D et G, respectivement. La bande D est relative au mode de vibration radiale de cycle aromatique et lié directement aux défauts dans la structure, tandis que la bande G provient du mode de vibration associé aux étirements des liaisons

C=C sp2 dans le plan pour les cycles aromatiques et aliphatiques (Rhili, Chergui et al. 2021).
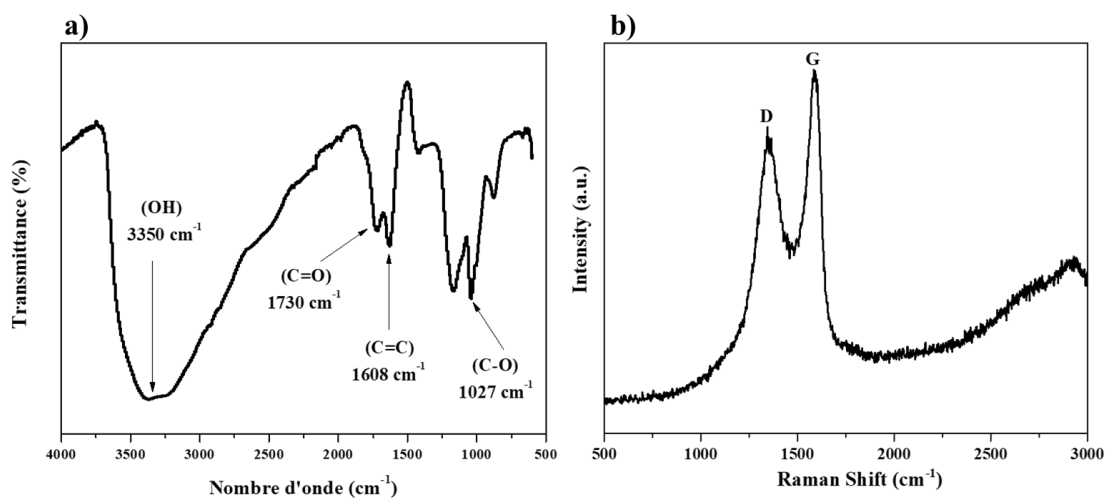
Figure 1.4   (a) Spectre FTIR de l'OG et (b) spectre Raman de l'OG

1.3.2.2 Microscopie électronique à balayage (MEB) et microscopie AFM de l'OG

La microscopie électronique à balayage nous permet d'observer la morphologie des feuillets de l'OG. Cette technique a été utilisée pour la caractérisation de l'oxyde de graphène lyophilisé pour visualiser les différents feuillets de manière indépendante. L'image MEB de l'OG (figure 1.5a) montre de longs feuillets minces séparés les uns sur les autres dans le matériel après lyophilisation. Ces feuillets sont aussi continus sans défauts apparents.

La microscopie AFM a été utilisée pour confirmer la morphologie de nos échantillons à l'échelle atomique et mesurer ainsi la taille et l'épaisseur des feuillets. La figure 1.5b,

représente l'image AFM de l'OG qui confirme une bonne séparation de feuillets d'OG selon la taille.
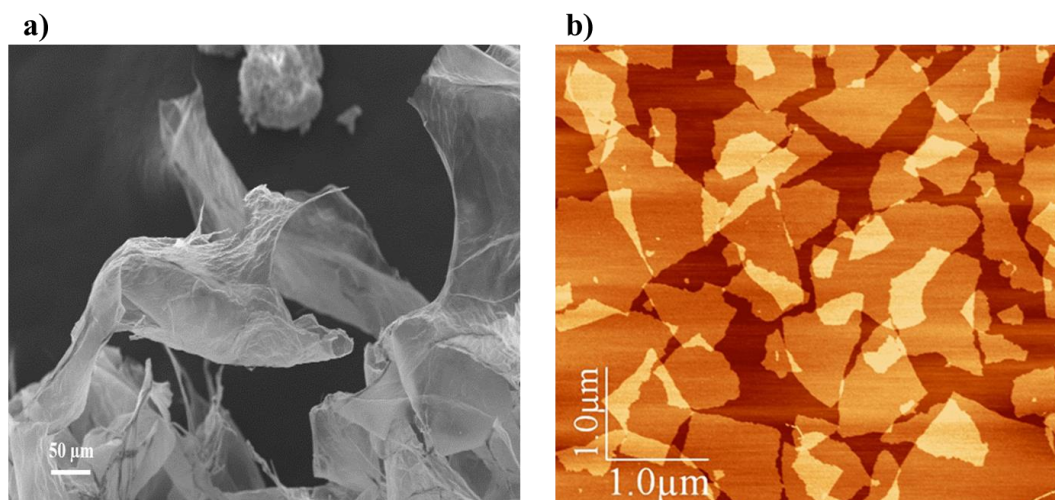
Figure 1.5   (a) Microscopie électronique à balayage (MEB) et (b) Microscopie à force atomique (AFM)

1.4   Oxyde de graphène réduit (rGO)

L'OG présente une faible conductivité électrique entraînant un comportement isolant en raison de la perturbation de sa structure électronique durant le processus d'oxydation, ce qui empêche un transfert de charge efficace. Il est nécessaire de le réduire afin de restaurer des propriétés électriques et donc se rapprocher des propriétés du graphène (MacDonald, Veneman et al. 2012).

L'oxyde de graphène réduit (rGO) a été préparé par la méthode de réduction hydrothermale. En bref, 100 mg d'OG ont été dissouts dans 100 ml d'eau désionisée et soumis à une sonication pendant 30 minutes pour obtenir une dispersion homogène. La

solution a été transférée dans un autoclave revêtu de téflon et chauffée à 200 °C pendant 24 h, puis laissée à refroidir à la température ambiante pour obtenir un produit noir. Le rGO obtenu a été lavé plusieurs fois avec de l'eau désionisée et recueilli par centrifugation. Finalement, le produit a été séché dans un four sous vide à 60 °C (Kamila, Mohanty et al. 2017).

1.4.1 Caractérisation de l'rOG

1.4.1.1 Microscopie électronique à balayage du rGO

L'image MEB de rGO (figure 1.6) présente une morphologie désordonnée avec des feuillets de carbone agglomérés les uns aux autres en raison de la réduction thermique.
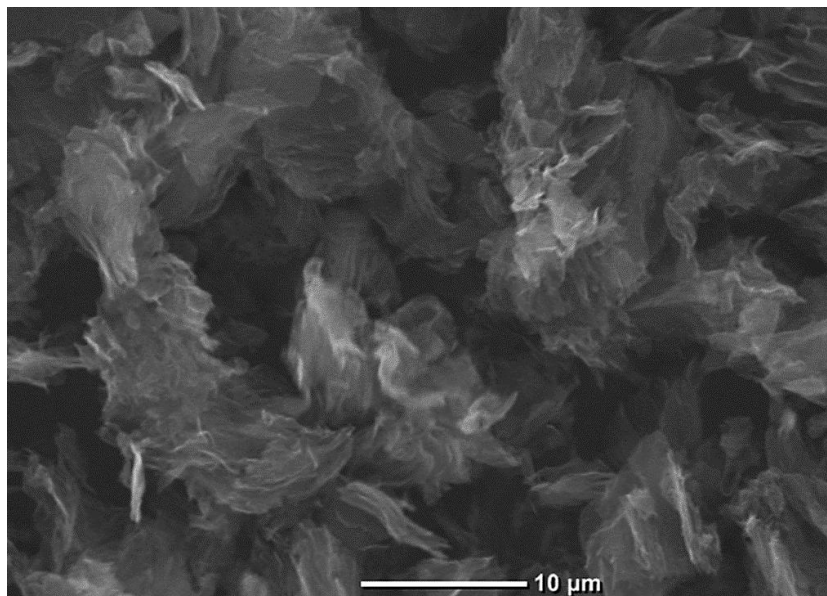
Figure 1.6   Image MEB de rGO

1.4.1.2 Diagramme XRD de l'GO et du rGO

Le diagramme XRD de GO (figure 1.7) montre un pic de diffraction cristalline intense à 2θ = 10° avec une distance interplanaire de 0,85 nm, correspondant au plan (002). Après réduction, ce fort pic de diffraction du plan (002) dans GO se déplace vers une position d'angle plus élevé à 2θ = 15,62° pour le rGO. La distance interplanaire a été considérablement diminuée de 0,4 nm, en raison de l'élimination des groupes fonctionnels, confirmant ainsi la réduction (Oliveira, Braga et al. 2018).
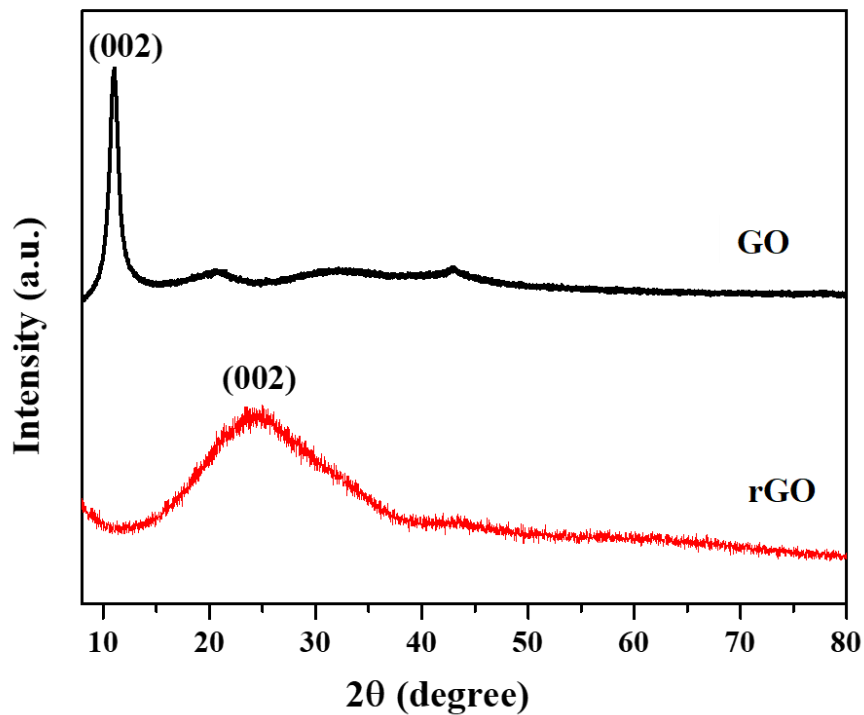
Figure 1.7   Diagramme XRD de l'OG et du rGO

1.5   Matériaux carbonés dopés aux hétéroatomes

Récemment, les matériaux carbonés dopés aux hétéroatomes comme l'azote (N), le bore (B), le soufre (S) et le phosphore (P) sont devenus des candidats prometteurs exempts de métaux. Ces matériaux ont des applications d'électrocatalyse, tels que les réactions de réduction de l'oxygène (RRO) dans les piles à combustible (Li, Wei et al. 2015, Qiao, Liao et al. 2015, Li, Wang et al. 2017) et les électrodes pour les supercondensateurs (Cheng, Yi et al. 2019, Zhou, Ye et al. 2020, Zou, Zhang et al. 2020). De plus, l'ajout de P et de N aux matériaux polymères permettent d'augmenter leur stabilité thermique et leur retardement de flamme (Yuan, Hu et al. 2017, Zhang, Xu et al. 2019, Rhili, Chergui et al. 2021).

Le graphène dopé par des hétéroatomes, appelé aussi substitution d'atomes de carbone par d'autres éléments chimiques, permet de modifier la structure électronique et les propriétés chimiques du graphène pour lui ajouter des propriétés de donneur ou accepteur d'électrons (Chen, Deng et al. 2015).

Le dopage à l'azote est très largement étudié du fait de sa taille atomique similaire à celle du carbone (77 pm contre 70 pm) et à ses cinq électrons de valence, disponibles pour former des liaisons covalentes fortes avec le carbone, améliorant sa stabilité (Wu, Santandreu et al. 2016, Yanilmaz, Tomak et al. 2017). De plus, l'électronégativité de l'azote selon l'échelle de Pauling, plus élevée que celle du carbone (3.04 contre 2.55) ce qui permet de modifier la structure électronique du matériau et de créer des sites actifs pour catalyser les réactions électrochimiques (Guo, Shibuya et al. 2016).

D'autres hétéroatomes sont utilisés pour le co-dopage du carbone tels que le N, le B, le S, ou encore le P. Ces hétéroatomes augmenteraient l'activité électrochimique en raison des effets électroniques synergiques de différents dopants (Chen, Sun et al. 2013, Gao, Fu et al. 2018).

L'introduction d'autres hétéroatomes fournit non seulement plus de sites actifs dans les réseaux de carbone, mais rend également les sites N plus catalytiquement actifs et plus efficaces. Les hétéroatomes les plus utilisés sont l'azote et le phosphore, ils appartiennent au même groupe dans le tableau périodique, mais le phosphore possède une capacité de donneur d'électrons plus élevée, ce qui est utile pour obtenir une propriété capacitive stable (Zhao, Wang et al. 2017). Par conséquent, nous pensons que la présence d'azote et de phosphore dans le carbone améliorerait considérablement les performances capacitives.

L'hexachlorocyclotriphosphazène (HCCP) a été choisi comme dérivé pour préparer nos matériaux à base d'azote et de phosphore. Le HCCP (figure 1.8) est une molécule cyclique constituée d'une alternance de trois atomes de phosphore et trois atomes d'azote. De plus, il possède six atomes réactifs de chlore qui peuvent être facilement substitués par d'autres groupes comme l'amine.
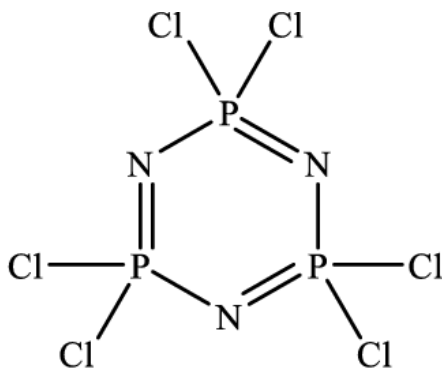
Figure 1.8   Structure chimique de l'hexachlorocyclotriphosphazène

1.6   Généralités sur les retardateurs de flammes

Depuis plus de 70 ans, les matériaux polymères remplacent peu à peu les matériaux traditionnellement employés (bois, métaux) et nous entourent constamment sous diverses formes : produits de commodité (emballage, textile), polymères techniques (composites, matériel électronique) ou de spécialités (fibre optique). Tandis que ces matériaux fournissent de nombreux avantages, ils présentent un problème : ils sont plus combustibles que les matériaux qu'ils remplacent, ce qui signifie qu'ils s'enflamment plus facilement entrainant de graves conséquences en cas d'incendie. Afin de minimiser leur inflammabilité et les risques associés, des additifs ignifugeants ou retardateurs de flamme (RF) sont en général incorporés à l'état fondu dans les polymères (Wilkie and Morgan 2009, Zhang, Rong et al. 2018).

1.6.1   La combustion des polymères

La combustion est une réaction d'oxydo-réduction qui fait intervenir deux éléments en présence d'une source d'énergie: les combustibles (éléments réducteurs) et les comburants (éléments oxydants). Le comburant est généralement l'oxygène contenu dans l'air. L'association de ces trois éléments constitue le « triangle du feu » (Pédrot and Tabareau 2020) présenté sur la figure 1.9.
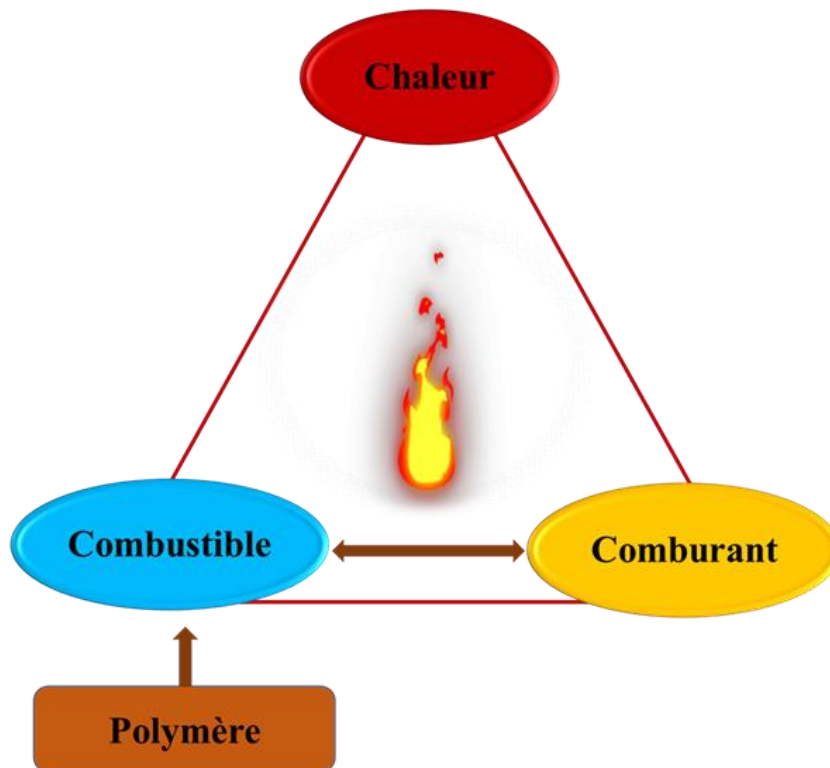
Figure 1.9   Schéma du triangle de feu

La combustion est une réaction chimique fortement exothermique, autonome, susceptible de s'accélérer brutalement et d'être accompagnée d'émission de rayonnements (Renner, Mensah et al. 2021). C'est un phénomène complexe faisant intervenir de nombreux paramètres et se déroulant en quatre principales étapes : (1) l'échauffement, (2) la dégradation thermique, (3) l'ignition et la (4) propagation (figure 1.10).
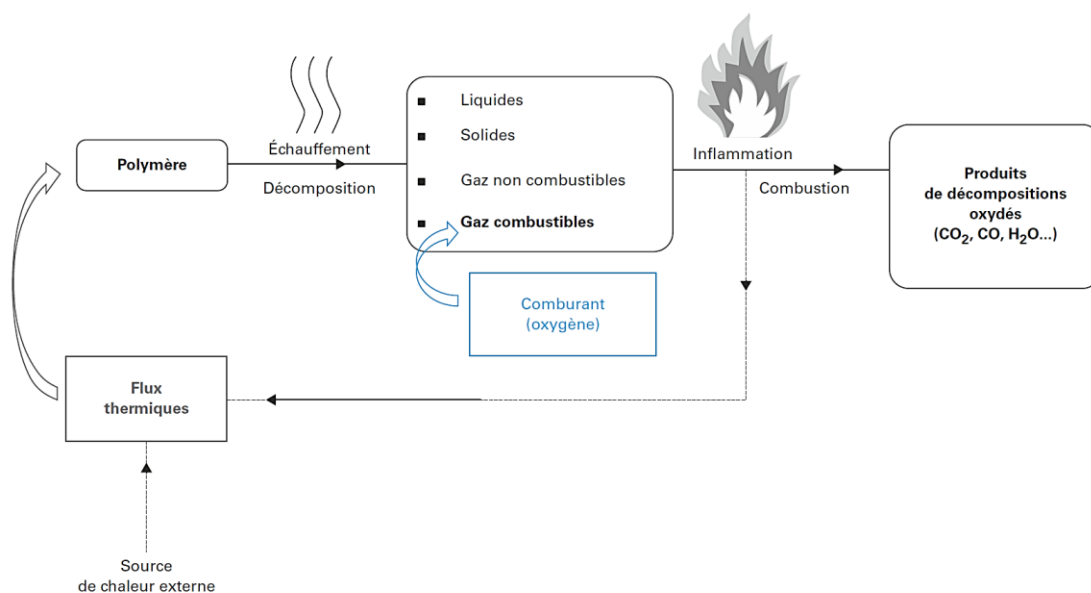
Figure 1.10   Schéma du procédé de combustion d'un polymère (Dasari, Yu et al. 2013)

Le polymère est susceptible de s'enflammer au voisinage d'une source de chaleur au contact de l'air. L'échauffement provoque la dégradation thermique du matériau; les liaisons les plus faibles du polymère se cassent et produisent des radicaux qui réagissent pour former des molécules inflammables. Cette dégradation thermique (pyrolyse) donne naissance à différents composés solides, liquides et gazeux, mais surtout à des gaz combustibles. Ces derniers se mélangent à l'oxygène de l'air et conduisent à une phase gazeuse inflammable. Tant qu'il y aura libération de produits de dégradation et présence d'oxygène en quantité suffisante, la flamme sera autoalimentée et pourra se propager (Sinha Ray and Kuruma 2020).

1.6.2   Développement d'un incendie

Un incendie commence par un départ de feu provoqué par une source de chaleur. Les phases principales du développement d'un feu sont présentées à la figure 1.11 en fonction de la température de l'environnement qui peut atteindre 1200 °C. La première phase correspond à l'échauffement du matériau par la source de chaleur.

Les premières flammes vont d'abord apparaître et se propager à la surface du matériau embrasé. Le feu se propage ensuite à l'environnement proche et la température des lieux augmente rapidement: c'est la phase dite « feu en développement ». La température ambiante peut alors atteindre une valeur critique supérieure à la température d'auto-inflammation de tous les matériaux combustibles présents qui vont s'enflammer: c'est l'embrasement généralisé éclair (en anglais flashover). Le feu complètement développé se poursuit jusqu'à l'épuisement soit du combustible soit de l'oxygène. La décroissance du feu s'amorce alors et l'incendie finit par s'épuiser et s'éteindre de lui-même (Mariappan 2016).
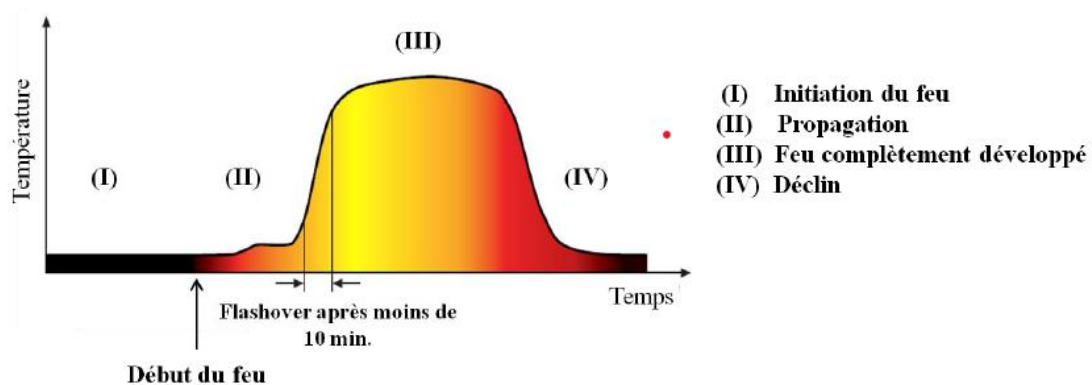
Figure 1.11   Les phases du déroulement d'un incendie (Friederich 2011)

1.6.3 Définition de retardateurs de flamme

Les retardateurs de flamme (RF) sont des composés chimiques utilisés dans les polymères comme dans le mobilier ou les composés électroniques pour prévenir et empêcher la propagation de l'incendie. Les RF visent à freiner la propagation de l'incendie, d'augmenter le temps d'ignition, d'améliorer la capacité d'auto-extinction du polymère, de diminuer la quantité de chaleur, de fumées et de gaz toxiques libérés (CO, HCN, etc.) lors de leur combustion (Geyer, Jambeck et al. 2017).

1.6.4 Différents retardateurs de flammes

La consommation mondiale en RF était d'environ 7 milliards d'euros pour l'année 2018. Environ 90% de la production mondiale de retardateurs de flammes aboutit dans l'électronique et les plastiques, les tissus et les meubles se partageant les 10% restants (Friederich 2011). Il existe quatre grandes catégories de composés retardateurs de flamme couramment utilisés : les inorganiques, les organophosphorés, les azotés et les halogénés (Sahyoun 2014).

La première catégorie de RF est celle des composés minéraux dont les deux principaux sont le trihydroxyde d'aluminium (Al $(OH)_3$, ATH), et hydroxyde de magnésium (Mg $(OH)_2$, MDH) qui sont utilisés sous forme d'additifs. Cependant, pour qu'ils soient efficaces, il est nécessaire d'incorporer des pourcentages conséquents (jusqu'à 60% en masse), ce qui va donc entrainer une diminution importante des caractéristiques mécaniques (Herbiet 2000).

La deuxième catégorie est celle des composés phosphorés organiques ou minéraux. Il s'agit principalement des esters phosphoriques. Ils présentent un large champ d'applications; sont utilisés dans les résines thermoplastiques et thermodurcissables, les mousses et polyuréthanes et dénotent une bonne efficacité en termes de sécurité des

incendies (Mizouchi, Ichiba et al. 2015). Les plus importants retardateurs de flammes contenant du phosphore sont : Les phosphates organiques, les polyphosaphates d'ammonium et les phosphates, les phosphonates, et les phosphinates (Ospina, Jayatilaka et al. 2018).

La troisième catégorie de RF correspond aux composés azotés et comprend essentiellement la mélamine pure (figure 1.12), des dérivés de mélamine comme des sels d'acides organiques et inorganiques (acide borique et acide cyanurique). À haute température, la mélamine se décompose avec l'élimination de l'ammoniac, ce qui dilue le mélange de gaz combustibles et conduits à la formation de produits de condensation stables à la chaleur, comme le melam, le melem et melon (Herbiet 2000).
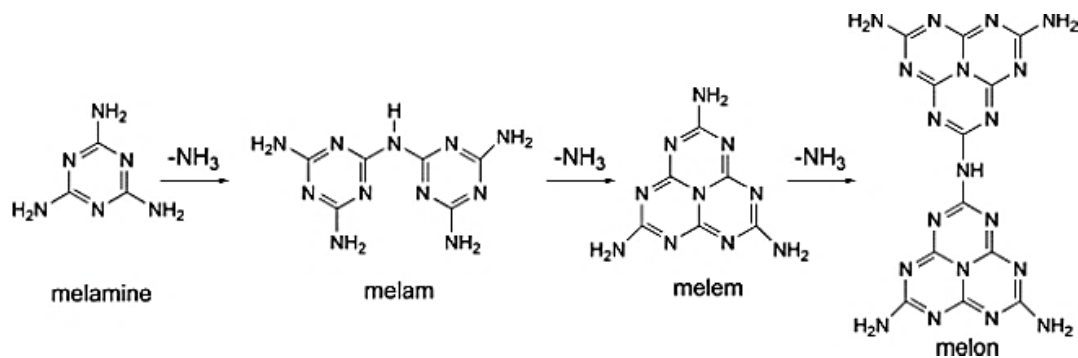
Figure 1.12   Décomposition thermique de la mélamine et ses produits homologues

La formation de melam, melem et melon génère des résidus dans la phase condensée, résultant par des processus endothermiques, également efficaces pour les propriétés de retard au feu (Costa and Camino 1988).

La dernière catégorie de RF est celle des composés halogénés. Les RF halogénés représentent une large part du marché Européen et 30% en volume de la production

mondiale (Covaci, Voorspoels et al. 2003). Ils sont utilisés dans les applications électriques et électrotechniques, dans les traitements textiles, dans les produits de construction et dans les mousses polyuréthane. Les halogènes sont très efficaces dans le piégeage des espèces radicalaires formées lors du processus de combustion des matériaux et présentes au sein des flammes, permettant ainsi le ralentissement de feu. Malgré leurs efficacités reconnues, les retardateurs de flamme halogénés sont suspectés d'avoir des effets nocifs pour la santé et l'environnement. Cela a conduit les Nations Unies et diverses réglementations RoHS et REACH à interdire et limiter leur emploi et à encourager la recherche d'agents de remplacement (Leikach 2007).

La figure 1.13 représente une espèce de dérivé chloré qui fut très utilisé en tant que retardateur de flamme. Le polychlorobiphényle (PCB) a été fabriqué pour servir comme isolant électrique ou comme lubrifiant dans l'industrie. L'exposition chronique à ce composé peut entraîner des dommages sur le foie, la reproduction et la croissance et ils sont suspectés d'être cancérigènes pour l'homme (Friederich 2011).
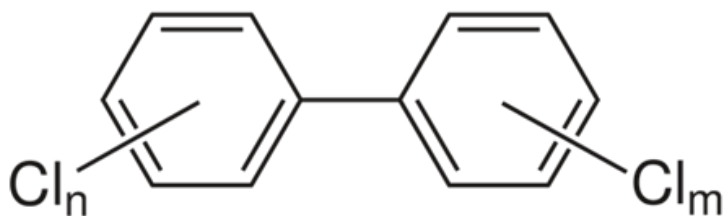
Figure 1.13   Structure de PCB

Les recherches actuelles s'orientent ainsi vers l'utilisation de RF non halogénée. Les retardateurs de flammes contenant du phosphore et/ou de l'azote constituent une bonne alternative d'après de récentes recherches (Rhili, Chergui et al. 2021).

1.6.5   Mode d'action des RF

Différents modes d'action d'un RF : Un RF intervient soit par voie physique, soit par voie chimique dans la phase où se déroule la combustion (figure 1.14) (Maqsood and Seide 2020).

a)

b)
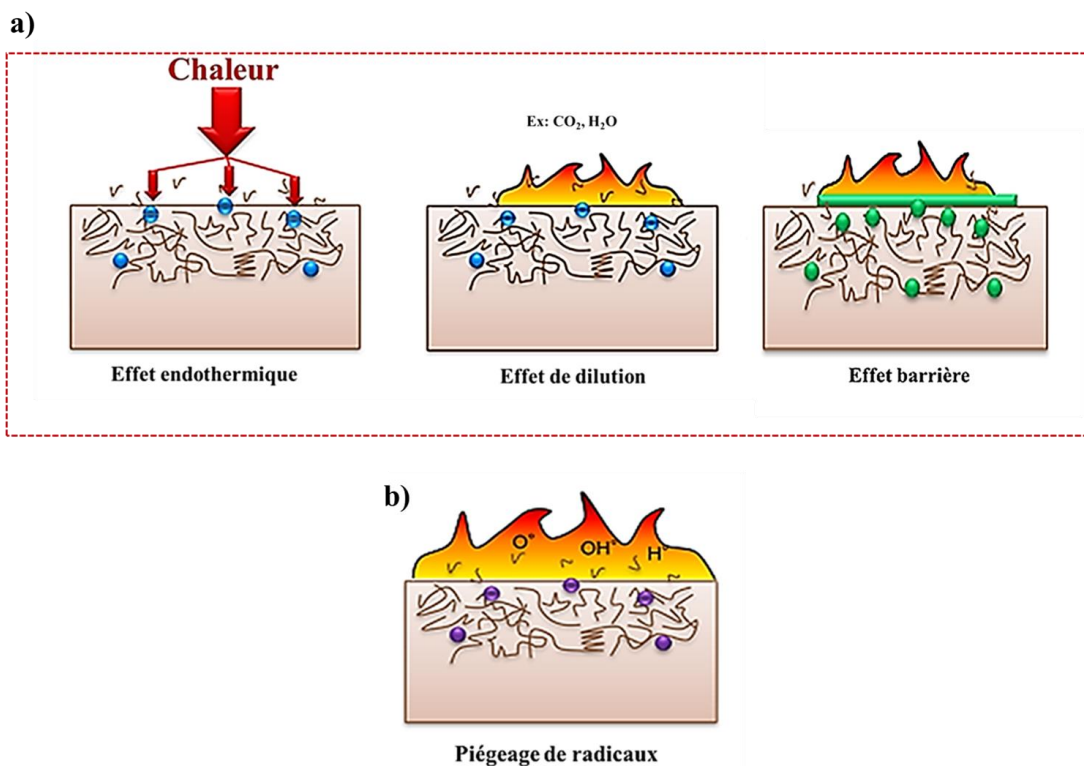
Figure 1.14   Différents modes d'action d'un retardataire de flamme : (a) action physique du RF et (b) action chimique du RF

L'action physique du RF (figure 1.14a) peut se faire par refroidissement, dilution ou formation d'une couche protectrice :

- Refroidissement : l'additif incorporé dans la matière polymère retarde la combustion par dégradation endothermique. Le trihydroxyde d'aluminium (ATH) fonctionne suivant ce principe et son efficacité est directement proportionnelle à la quantité d'additif introduite dans le matériau.

- Dilution : ce processus met en jeu la libération des gaz inertes (H_2O, CO_2 ou NH_3) dans la zone de combustion, ce qui diminue la température de flamme et provoque l'extinction.

- Formation d'une couche protectrice : Le matériau est protégé de la chaleur et des flammes par une couche protectrice solide, à la suite de la formation d'un char (des résidus charbonnés), qui empêche également l'accès de l'oxygène nécessaire au processus de combustion vers l'échantillon. On parle d'effet barrière.

L'action chimique (figure 1.14b) peut avoir lieu en phase gazeuse ou condensée :

- En phase gazeuse, le RF inhibe les réactions radicalaires en neutralisant par piégeage les radicaux $HO°$ et $H°$ responsables de la propagation de la flamme. C'est le cas des composés halogénés qui vont libérer les radicaux ($X°$). Cela a pour conséquence le ralentissement de la réaction de combustion par coupure de la chaîne réactionnelle (Sai, Ran et al. 2022).

- En phase condensée, le RF intervient en formant une couche charbonnée qui va isoler le matériau des flammes et de l'oxygène, et arrêter l'émission des gaz de dégradation du polymère vers l'extérieur (Lee, Yi et al. 2012).

Le Tableau 1.2 résume les principales classes de RF employées et les modes d'action qui leur sont associés (Döring and Diederichs 2007, Jiang, Gui et al. 2014).

Tableau 1.2　　　　Principales classes de RF et leurs modes d'action

Retardataire de flamme	Quelques exemples	Modes d'action
Halogénés	Aromatiques :TBBA, PPBDE, Aliphatiques (ester phosphate bromés) et Cycliques	• Inhibition des réactions radicalaires en phase gaz (capture des radicaux énergétiques H° et OH°, remplacés par X° de plus faible énergie)
Phosphorés	Polyphoshate d'ammonium, phosphonates, phosphinates, phosphites, phosphore rouge.	• Formation d'un résidu solide phospho-carboné • Formation de radicaux (PO°, PO$_2$°, HPO°) pour piéger les radicaux actifs (HO°., H°) • Libération de gaz non combustibles (H$_2$O, CO$_2$, NH$_3$...) qui diluent les gaz combustibles et les radicaux dans la phase gazeuse
Azotés	Mélamine et ses derivés (melam, melem, melon), et ses sels d'acides (borique, cyanurique, phosphorique)	• Dilution des gaz combustibles par libération de NH$_3$ • Décomposition endothermique • Réticulation qui favorise la formation d'un char
Minéraux hydratés	Dihydroxyde de magnésium (MDH), hydroxyde d'aluminium (ATH), ALOOH (boehmite)	• Décomposition endothermique : refroidissement du polymère • Dilution des gaz combustibles : libération d'eau • Formation d'une couche charbonnée constituée d'oxydes métalliques (Al$_2$O$_3$, MgO) et de composés polyaromatiques
Oxydes métalliques	SiO$_2$, TiO$_2$, Al$_2$O3, Fe$_2$O$_3$	• Formation d'une couche protectrice (effet barrière) • Favorise la formation d'un char • Limitation la mobilité des chaines de polymères • -Modification du mécanisme de dégradation du polymère

1.7   Supercondensateurs (SC)

Les systèmes de stockage d'énergie jouent un rôle important dans notre vie quotidienne. L'énergie spécifique, la puissance spécifique, la durée de vie, la fiabilité et la protection sont les paramètres les plus importants lors de la sélection d'un dispositif de stockage d'énergie (Zhang and Zhao 2009, Kandalkar, Dhawale et al. 2010, Cao and Emadi 2011).

Les supercondensateurs, les batteries et les condensateurs font partie des dispositifs énergétiques non conventionnels de stockage d'énergie. Leur fonctionnement est basé sur le principe de la conversion électrochimique de l'énergie. Ces dernières années, les SC ont pris une place importante dans le marché du stockage de l'énergie en raison de leur grande densité de puissance, leur longue durée de vie, leur faible sensibilité aux températures extrêmes et leur bas cout (Zhang and Zhao 2009, Kandalkar, Dhawale et al. 2010).

Le diagramme de Ragone (figure 1.15) montre la place des supercondensateurs en termes de capacité de stockage et de puissance par rapport aux autres systèmes. Ce diagramme montre que les condensateurs électrolytiques possèdent une très grande densité de puissance, mais une très faible énergie spécifique. Ils sont utilisés généralement pour des constantes de temps de l'ordre de la microseconde. À l'opposée, les batteries possèdent des densités de puissance très faible et une énergie spécifique élevée. Elles peuvent être utilisées avec une constante de temps supérieure à la minute. En ce qui concerne la pile à combustible, c'est un convertisseur d'énergie et non pas un élément de stockage (Kim, Sy et al. 2015).

Entre les batteries et les condensateurs électrolytiques, on trouve les supercondensateurs qui sont utilisés pour une utilisation de stockage de l'énergie avec une constante de temps inférieure à quelques dizaines de secondes.
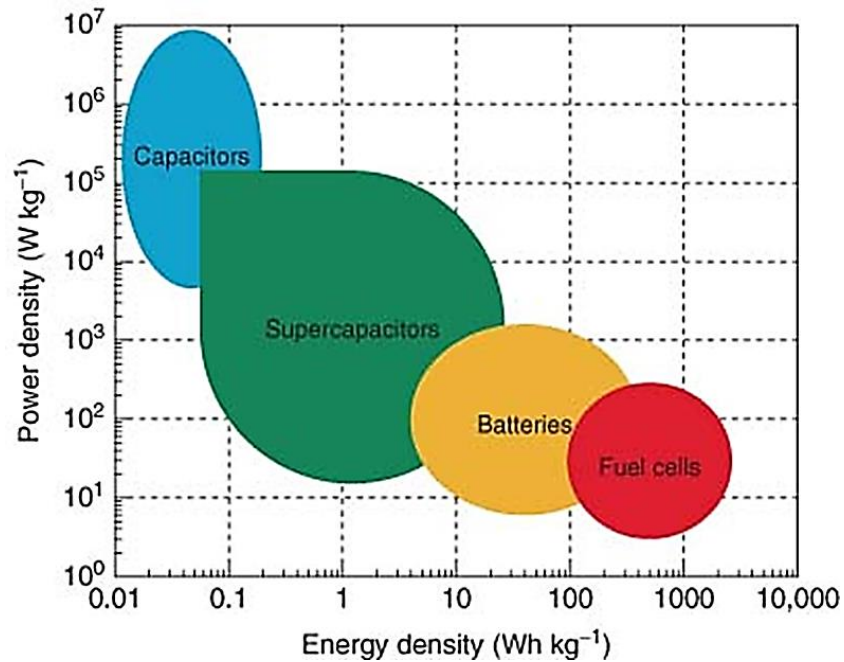
Figure 1.15   Diagramme de Ragone permettant de comparer les principaux systèmes de stockage de l'énergie (Zhang, Zhang et al. 2011)

Les supercondensateurs indifféremment appelés Condensateurs à double couche électrochimique (EDLC) possèdent une puissance instantanée plus importante que celle des batteries et une énergie plus grande que celle des condensateurs classiques. Leur durée de vie est plus élevée que celle des batteries (plusieurs centaines de milliers de cycles).

Le tableau 1.3 donne une comparaison des principales caractéristiques des supercondensateurs, des condensateurs et des batteries.

Tableau 1.3   Comparaison des principales caractéristiques des batteries, des condensateurs et des supercondensateurs (Pandolfo and Hollenkamp 2006, Burke 2007)

	Condensateur	Supercondensateur	Batterie
Principe de fonctionnement	Adsorption des charges électriques à la surface des électrodes	Adsorption des ions à la surface des électrodes	Réactions redox
Puissance maximum (W.kg^{-1})	>> 50 000	1 000-20 000	≤ 2 000
Energie maximum (Wh.kg^{-1})	< 0,1	1-10	30-180
Durée de vie (cycles)	Infinie	1 000 000	~ 1 000
Temps de charge/décharge	De quelques microsecondes à quelque millisecondes	Quelques secondes	Quelques minutes à quelques heures (10 − 15 min au minimum)
Rendement énergétique	~ 100 %	~85 − 98 %	70-85 %

D'après les donnes du tableau 1.3, les supercondensateurs possèdent une durée de vie théoriquement illimitée ; elle est cependant limitée par la dégradation de l'électrolyte, des fonctions de surface présentes sur le carbone ou encore par la corrosion des collecteurs de courant lors du cyclage en tension. Cependant, ils peuvent effectuer aisément 1 000 000 cycles (Burke 2007).

Pour les mêmes raisons, un supercondensateur se charge en quelques secondes alors qu'une batterie nécessite un minimum de quelques minutes. De plus, le phénomène étant réversible, le rendement énergétique des supercondensateurs est de l'ordre de 95% alors qu'il est inférieur à 80% pour les batteries. Tout ceci présente des avantages

par rapport aux batteries où ont lieu des réactions faradiques qui limitent la durée de vie, ainsi que le rendement de ces systèmes. De même un supercondensateur stocke plus d'énergie qu'un condensateur diélectrique.

1.7.1   Principes de fonctionnement des supercondensateurs

Les supercondensateurs sont constitués de deux électrodes de carbone déposées sur des collecteurs de courant métalliques imprégnées dans un électrolyte, entre lesquels un séparateur poreux assure l'isolation électronique. En effet, lorsqu'on applique une tension aux bornes d'un supercondensateur, on crée une zone de charge d'espace aux deux interfaces électrode-électrolyte. C'est ce que l'on appelle la double couche électrochimique (figure 1.16). Le stockage de l'énergie est donc électrostatique et non pas faradique comme dans le cas des batteries, puisqu'il n'y a pas de réaction électrochimique (Cao and Emadi 2011).
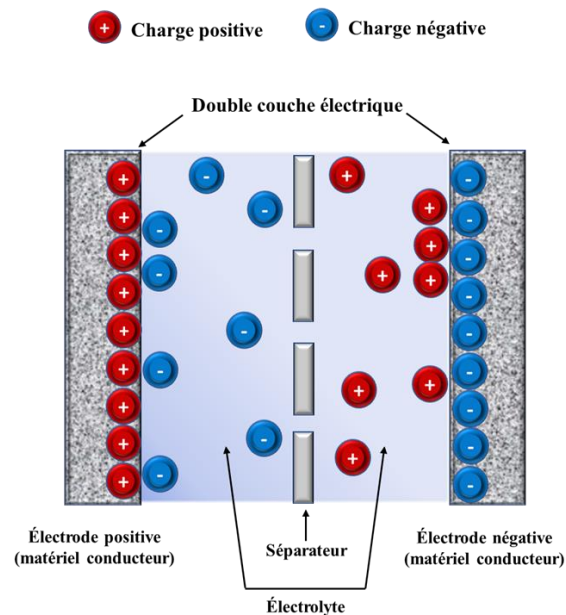
Figure 1.16   Schéma d'un supercondensateur

1.7.1.1 La double couche électrochimique

La double couche électrochimique a été décrite par différents modèles successifs. Le premier modèle (figure 1.17a) a été proposé par Helmholtz (du 19 -ème siècle), qui considère simplement la formation à l'interface électrode/électrolyte d'une couche d'ions, par exemple d'anions si l'électrode est chargée positivement (Helmholtz 1879).

Le deuxième modèle (figure 1.17b) a été proposé pour la première fois par Gouy (Gouy 1910) et Chapman (Chapman 1913) (début du 20e siècle). Ce modèle envisage la formation d'une couche diffuse liée à l'agitation thermique et au sein de laquelle le potentiel décroit de façon exponentielle. Finalement le modèle de Stern en 1924 (Stern 1924) combine ces deux approches : il décrit la formation d'une couche compacte au voisinage proche de l'électrode puis d'une couche diffuse (1.17c).

La capacité de la double couche (C_{dl}) peut être représentée par la mise en série de deux capacités, la capacité de la couche compacte d'Helmholtz (C_H) et la capacité de la couche diffuse de Gouy-Chapman et Stern (C_{diff}). La capacité de la double couche est donnée par l'équation suivante :

$$\frac{1}{C_{dl}} = \frac{1}{C_H} + \frac{1}{C_{diff}}$$

(1)
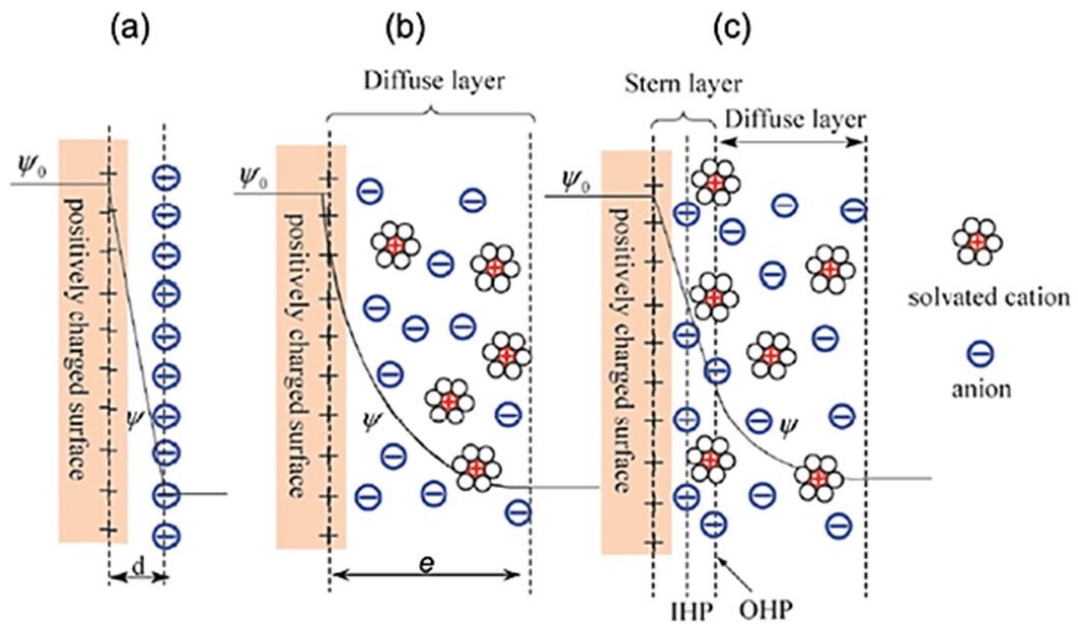
Figure 1.17   Modèles de la double couche pour une électrode chargée positivement : (a) Helmholtz, (b) Gouy-Chapman et (c) Stern avec les plans interne (IHP) et externe (OHP) de Helmholtz. IHP correspond à la plus proche distance d'approche des ions et OHP à celle des ions non spécifiquement adsorbés, au-delà de laquelle débute la couche diffuse, d'après la référence (Zhang and Zhao 2009)

1.7.2   Technologie des supercondensateurs

Un supercondensateur performant dépend de plusieurs facteurs, notamment le matériau d'électrode, l'électrolyte et le séparateur. Le matériau doit avoir des valeurs de capacité élevées et une grande surface (Sharma and Kumar 2020).

1.7.2.1 Matériaux d'électrodes

Le matériau de l'électrode joue un rôle important dans les performances du supercondensateur. Les électrodes doivent avoir une conductivité élevée, une stabilité en température, une bonne stabilité chimique (inertie), une surface spécifique élevée, une résistance à la corrosion, doivent être respectueuses de l'environnement et avoir un coût moindre (Lobato, Suárez et al. 2017, Poonam, Sharma et al. 2019).

Cependant, la taille des pores des matériaux conducteurs détermine électrochimiquement la surface active, qui peut être ajustée simplement par l'introduction de nanostructures. Lorsque la taille des pores augmente, la distance entre les pores augmente et la capacité diminue (Raza, Ali et al. 2018). Plusieurs matériaux d'électrodes sont utilisés comme les matériaux à base de carbone, les oxydes métalliques et les polymères.

1.7.2.2 Électrolyte

Les électrolytes/solutions jouent un rôle essentiel dans la mise en place de propriétés importantes telles que la densité de puissance, la plage de température et la conductivité (Wang, Zhang et al. 2012). Ils sont utilisés pour la conduction ou le mouvement des ions.

Les paramètres importants pour la sélection d'un électrolyte sont les matériaux d'électrode, le type d'ions, la taille, la concentration et l'interaction ion-solvant (Raza, Ali et al. 2018). De plus, les électrolytes pour les supercondensateurs doivent avoir une large fenêtre de potentiel, une concentration ionique élevée, une bonne stabilité électrochimique, une faible résistance équivalente, moins de volatilité, moins de viscosité, la non-toxicité, un petit rayon d'ion solvaté et un faible coût (Wang, Zhang et al. 2012).

Cependant, le choix de l'électrolyte joue un rôle important sur les performances d'un supercondensateur. Il peut affecter la capacité, la durée de vie et l'énergie ou la densité de puissance (Lai, Yang et al. 2012).

1.7.2.3 Séparateur

La construction des supercondensateurs fait également intervenir une membrane isolante poreuse, donc conductrice ionique, séparant les deux électrodes imprégnées d'électrolyte. Les séparateurs sont généralement formés à partir de films polymères tels que le polypropylène (PPE) ou à partir de papier cellulosique renforcé. Sa porosité doit être adaptée à l'électrolyte pour que la résistance de l'électrolyte dans le séparateur soit le plus faible possible (Willfahrt, Steiner et al. 2019).

1.7.3   Applications des supercondensateurs

Les supercondensateurs ont plusieurs applications (figure 1.18), ils sont utilisés pour stocker de l'énergie et sont utiles dans une certaine mesure par rapport aux batteries. La flexibilité des supercondensateurs, les matériaux utilisés pour l'électrode et l'électrolyte et le processus de stockage de charge régissent toutes les performances des supercondensateurs (Zhang and Zhao 2009).

Les premières applications ont longtemps été cantonnées à la sauvegarde de mémoire informatique, ils ont été rapidement utilisés pour l'alimentation des outils portables nécessitant des apports de puissance, comme les visseuses électriques, et plus généralement en électronique de puissance.

Les supercondensateurs sont idéaux pour toute application ayant un cycle de charge court et des exigences de fiabilité élevées, telles que les sources de récupération d'énergie, notamment les grues de charge, les chariots élévateurs et les véhicules électriques. D'autres applications exploitent la capacité d'un supercondensateur à absorber et à libérer de l'énergie presque instantanément, comme la sauvegarde de l'alimentation d'usine (Kötz and Carlen 2000).
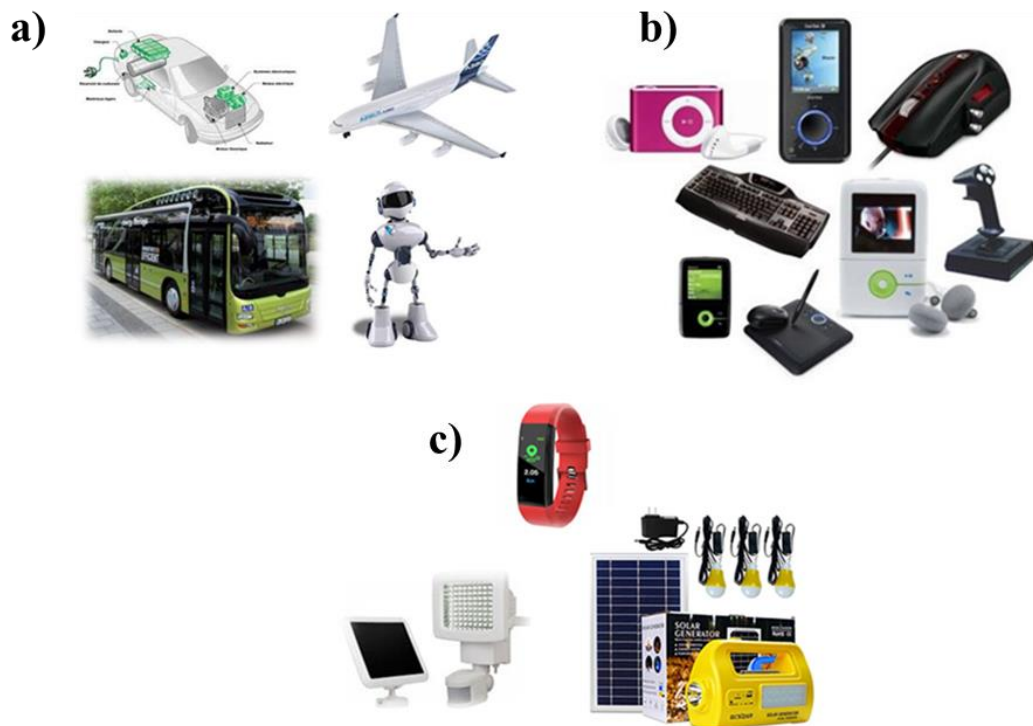
Figure 1.18   Quelques applications des supercondensateurs : (a) récupération d'énergie, (b) sauvegarde de la mémoire et (c) stockage d'énergie

CHAPITRE II

HEXACHLOROCYCLOTRIPHOSPHAZENE FUNCTIONALIZED GRAPHENE OXIDE AS A HIGHLY EFFICIENT FLAME RETARDANT

Khaled Rhili[a], Siham Chergui[a], Ahmad Samih El Douhaibi[b] and Mohamed Siaj [a,*]

[a]Department of Chemistry and Biochemistry, Université du Quebec à Montréal, Montréal QC, H3C 3P8, Canada

[b] Department of Chemistry, Lebanese University, College of Science III, Campus Mont Michel, 1352, Tripoli, Lebanon

*Corresponding author at: Email: siaj.mohamed@uqam.ca

Contribution des auteurs

KHALED RHILI

L'auteure principale a effectué toutes les manipulations expérimentales incluant la synthèse de produit ainsi que les caractérisations, la recherche bibliographique et les traitements des résultats. Aussi, elle a écrit la première version du manuscrit et a contribué à la version finale du manuscrit.

SIHAM CHERGUI

Le co-auteur a effectué des analyses et a participé à l'interprétation des résultats et la rédaction du manuscrit.

Ahmad Samih El Douhaibib

Le co-auteur a participé à l'interprétation des résultats et la rédaction du manuscrit.

MOHAMED SIAJ

L'auteur de correspondance a effectué la supervision des travaux et il a participé à l'interprétation des résultats, à l'écriture ainsi qu'à la révision finale du manuscrit.

ACS Omega, publiée (2020).

2.1 Résumé

Une synthèse d'un retardateur de flamme à base d'oxyde de graphène (OG) fonctionnalisé avec de l'hexachlorocyclotriphosphazène (HCCP) et de la *p*-Phénylèndiamine (*p*-PDA) a été réalisée avec succès. L'oxyde de graphène fonctionnalisé (FGO) a démontré une efficacité en tant que retardateur de flamme. L'analyse thermogravimétrique a démontré que l'ajout d'HCCP à l'oxyde de graphène lui permet une grande stabilité thermique et une meilleure résistance à la température ce qui lui confère une application comme retardateur de flamme. Une résine époxy (EP) thermodurcissable a été synthétisée par mélange d'éther diglycidylique de bisphénol-A (DGEBA) et de *m*-Phénylènediamine (*m*-PDA) comme durcisseur. Le FGO obtenu a été incorporé dans la résine époxy pour former des composites. Les propriétés ignifuges, le comportement de dégradation thermique et la combustion des composites ont été étudiés par TGA et par une flamme de brûleur Bunsen. La structure chimique de FGO a été caractérisée par des techniques spectroscopiques et d'imageries, telles que la résonance magnétique nucléaire à l'état solide (RMN), la spectroscopie infrarouge à transformée de Fourier (FTIR), la spectroscopie Raman, l'analyse thermogravimétrique (ATG) et la microscopie électronique à balayage (MEB). Les résultats obtenus par FTIR révèlent la présence de groupes (P=N) et (P-N) caractéristiques de l'HCCP ce qui indique le bon ancrage de HCCP sur l'oxyde de graphène. Le spectre Raman démontre la présence de deux bandes D et G représentatifs de la structure d'oxyde de graphène après l'ajout de l'HCCP.

2.2   Abstract

Flame-retardant composite was synthesized through a simple graphene oxide functionalization route with hexachlorocyclotriphosphazene and *p*-phenylenediamine. Flame experiments conducted on the synthesized composite proved its importance as tremendously resistant to fire. The thermogravimetric analysis (TGA) shows clearly that the functionalized graphene oxide (FGO) exhibits an enhanced thermal stability and better temperature resistance. A thermoset epoxy resin was prepared by incorporating different percentages (2, 5, and 10%) of FGO to diglycidyl ether of bisphenol A (DGEBA). The flame-retardant properties, thermal degradation behavior, and combustion of the DGEBA thermosets cured by *m*-phenylenediamine were investigated using a Bunsen burner flame approaching the flame temperature of a fire and TGA. The chemical structure of FGO was characterized with spectroscopic and imaging techniques including Fourier transform infrared spectroscopy, Raman spectroscopy, X-ray diffraction, TGA, scanning electron microscopy, energy-dispersive X-ray spectroscopy elemental mapping, and X-ray photoelectron spectroscopy. Due to its high flame-retardant capabilities, such a composite could promise potential applications in the manufacture of inflammable materials for different uses.

Keywords: Graphene oxide, hexachlorocyclotriphosphazene, flame retardant, epoxy resin, thermal stability.

2.3   Introduction

Synthesis and applications of graphene and graphene oxide (GO) have been the subjects of numerous studies in recent years. Graphene exhibits inert properties towards chemical reactions, which limit their use as potential reagents for further chemical syntheses and applications. Despite of graphene, GO is a very promising material for various applications in chemical synthesis (Brisebois and Siaj 2020).

The presence of many oxygen atoms in form of hydroxyl and epoxide functionalities on the basal plane of graphene sheets, as well as carbonyl and carboxyl moieties on the edge of the sheets, renders this material as a potential reagent for various chemical applications (Stankovich, Dikin et al. 2006). These applications included use of GO as catalysts in Friedel-Crafts reactions,(Kumar and Rao 2011) oxidation (Dreyer, Jia et al. 2011) esterification (Qi, Xu et al. 2013) and Knoevenagel condensation reactions (Islam, Roy et al. 2014) and Diles-Alder reaction (Brisebois, Kuss et al. 2016). Kaviyarasu *et. al* studied the effect of GO/ZnO material in photocatalytic applications, such as reduction of Cr(IV) compounds (Kaviyarasu, Magdalane et al. 2015).

Further applications of GO materials were reported by Maaza and co-workers; such applications include irradiation of Cu^{+2} ions on Co_3O_4-NiO-ZnO/GO nanowire and its effect on different electrochemical properties of the material (Obodo, Ahmad et al. 2020). Analytical studies were also conducted by Bajjou *et. al* regarding charge carrier dynamics and the effect of pH on optical properties of porphyrin-graphene oxide composites (Bajjou, Bakour et al. 2018).

Numerous studies were conducted on the functionalization of GO with different positional isomers of phenylenediamine (PDA), pertaining to the plethora of applications for the materials obtained, including but not limited to anticorrosive agents, (Hwang, Kim et al. 2019) removal of heavy metals and other contaminants from

water (Jin, Huang et al. 2019, Kandjou, Perez-Mas et al. 2019) and preparation of superhydrophobic surfaces (Wang, Yu et al. 2017).

Studies of the electrochemical properties of PDA functionalized GO (GO-PDA) have received the highest interest (Zou, Zhong et al. 2016, Pisarevskaya, Ehrenburg et al. 2017, Rajagopalan, Kim et al. 2017, Yang, Shin et al. 2018, Chang, Xia et al. 2019). For instance, Dasari*et.al* reported a facile functionalization of GO with *p*-Phenylenediamine (*p*-PDA) to produce a material (GO-*p*-PDA) that showed a sharp increase in electrical conductivity compared to pure GO. Incorporation of the obtained GO-*p*-PDA material into electrically insulating polypropylene produced a new electrically conducting composite (Dimiev, Alemany et al. 2012).

Wong and co-workers reported a detailed study on the functionalization of GO with *o*-PDA, *m*-PDA, and *p*-PDA, showing that *m*-PDA and *p*-PDA enlarged the graphene interlayer spacing by 1.3 and 1.41 nm, respectively, and showed considerable improvement of electrical capacitance (Song, Choi et al. 2016). Yuan and co-workers showed that grafting of the HCCP- *p*-PDA to GO improved the flame retardancy of polypropylene (Yuan, Hu et al. 2017). Though Yuan's FGO showed good flame retardancy, the use of $Ni(OH)_2$ was necessary to further improve flame retardancy, and the maximum residual char yield they obtained was only 8.5% when 2% of their $FGO/Ni(OH)_2$ was incorporated on polypropylene (Yuan, Hu et al. 2017).

The phosphazenes materials are polymers with transition nitrogen and phosphorus atoms known for their high thermal and chemical stabilities. The cyclic polyphosphazene ($[PC_{l2}N]_3$) obtained during phosphazene ring synthesis (Davy, Xie et al. 1991) shows exceptional properties, which impose it as one of the most interesting subjects of thermal and chemical stabilities studies (Singler, Hagnauer et al. 1974, Wisian-Neilson, Allcock et al. 1994).

In fact, its connection with other material allows increased properties as their thermal and flame-retardants (Kumar, Fohlen et al. 1983, Kumar, Khullar et al. 1993). Herein, we investigate the properties of polyphosphazenes/*p*-PDA/GO (HCCP- *p*-PDA functionalized GO) composite as flame retardant. To obtain FGO product as efficient flame-retardant, the graphene oxide (GO) was successfully functionalized with hexachlorocyclotriphosphazene (HCCP) and *p*-phenylendiamine (*p*-PDA). Then, different percentage of FGO was incorporated into the epoxy resin DGEBA *in situ* curing polymerization to enhance the thermal stability of composites. The typical preparation procedure to FGO is illustrated in figure 2.1.
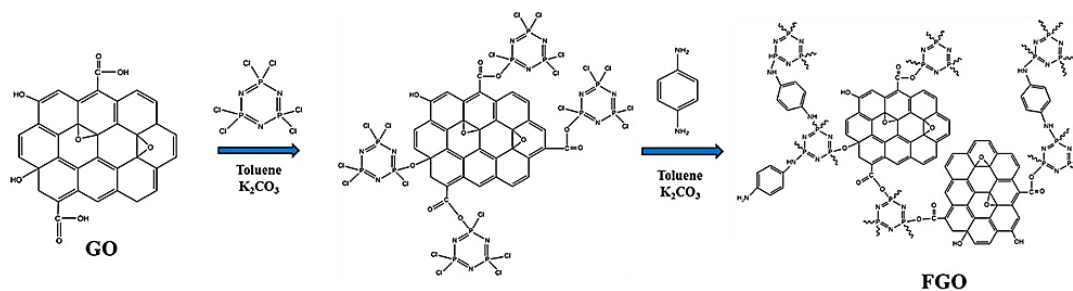
Figure 2.1   Schematic representation of the preparation route of FGO

2.4   Results and discussion

2.4.1   Characterization of FGO

The functional groups of the obtained products GO, HCCP and FGO were characterized by FTIR spectroscopy. Figure 2. 2a, shows the FTIR spectrum of GO with different peaks of the characteristic functional groups due to oxidation. The GO has a broad band characteristic of the hydroxyl functions at 3315 cm^{-1} C-OH and C=O stretching vibrations at 1735 cm^{-1} frequencies of the–COOH. The peak at 1635 cm^{-1} belongs to the aromatic C=C vibrations. The peaks at around 1225 cm^{-1} and

1061 cm^{-1} corresponding to phenolic C-O and epoxy C-O-C groups, respectively, similar to the previous literature (Mo, Gou et al. 2012, Yuan, Hu et al. 2017).

Some new absorption peaks in the spectrum of FGO appear at around 1170 cm^{-1} and 834 cm^{-1} corresponding to the groups P=N and P-N in the starting material (hexachlorocyclotriphosphazene) (Verma and Dutta 2015) which indicated that the phosphazene ring structure is not destroyed during the reaction. Meanwhile, another important peak appearing at 938 cm^{-1} was assigned to the stretching P-NH-Ph, (Zhang, Xu et al. 2019) which indicated the occurrence of copolymerization between HCCP and *p*-PDA. The peaks at 3330 cm^{-1}, 1511cm^{-1}, and 1386 cm^{-1} are assigned to N-H stretching, C-N stretching and N-H bending (Yuan, Hu et al. 2017) respectively.

The P-Cl peak at 660 cm^{-1} of HCCP (Yuan, Hu et al. 2017) disappeared in the FGO indicating that a nucleophilic substitution of HCCP by *p*-PDA had taken place. Hence, FTIR analysis confirms the functionalization of graphene oxide by HCCP. In parallel, Raman spectroscopy was used to investigate the quality of the carbon nanomaterials of GO and functionalized FGO. As shown in figure 2. 2c, the Raman spectrum of GO shows two prominent peaks at 1345 cm^{-1} and 1584 cm^{-1}, corresponding to the D and G bands, respectively. The D band relates to the mode of radial vibration of the aromatic cycle and is related directly to the defects in the structure, while the G band comes from the mode of vibration associated with stretching of the C = C sp^2 links in the plane for the aromatic and aliphatic cycles (Zhang, Zhang et al. 2011).

Compared to the Raman spectrum of GO, the Raman spectrum of FGO also contains both D and G bands at 1383 cm^{-1} and 1556 cm^{-1}, respectively. It is clear that the G band was broadened and shifted with higher intensity, while the D-band around 1383 cm^{-1} can be deconvoluted into two Lorentzian components which can be used to assess the degree of the defect, which could be attributed to the Raman mode activated by the distortions (Bao, Song et al. 2012). We agree that the D band is related to sp3 c atoms. However, we believe that the preparation route of FGO does not increase the amount

of the sp3 carbon species. The addition between the cyclophosphazene and
p-Phenylenediamine (*p*-PDA) involves the carboxylic moieties instead of the ethylenic
double bond. In parallel, the ratio between D (D$_1$+D$_2$) peak and G peak
intensities *($I_{(D)}$/$I_{(G)}$)* leads to the amount quantification of the defect in the material.
Measurements of ration *($I_{(D)}$/$I_{(G)}$)* for GO and FGO material were collected. The
($I_{(D)}$/$I_{(G)}$) of FGO was 0,43 and *($I_{(D)}$/$I_{(G)}$)* of GO was 0,83. These changes could be
assigned to the grafting of HCCP and *p*-PDA molecules into the hexagonal structure
of carbon atoms, which corresponds to an increase of structural disorder (sp^3 defects)
(Stankovich, Dikin et al. 2007). This supposition will be confirmed by XRD analysis.
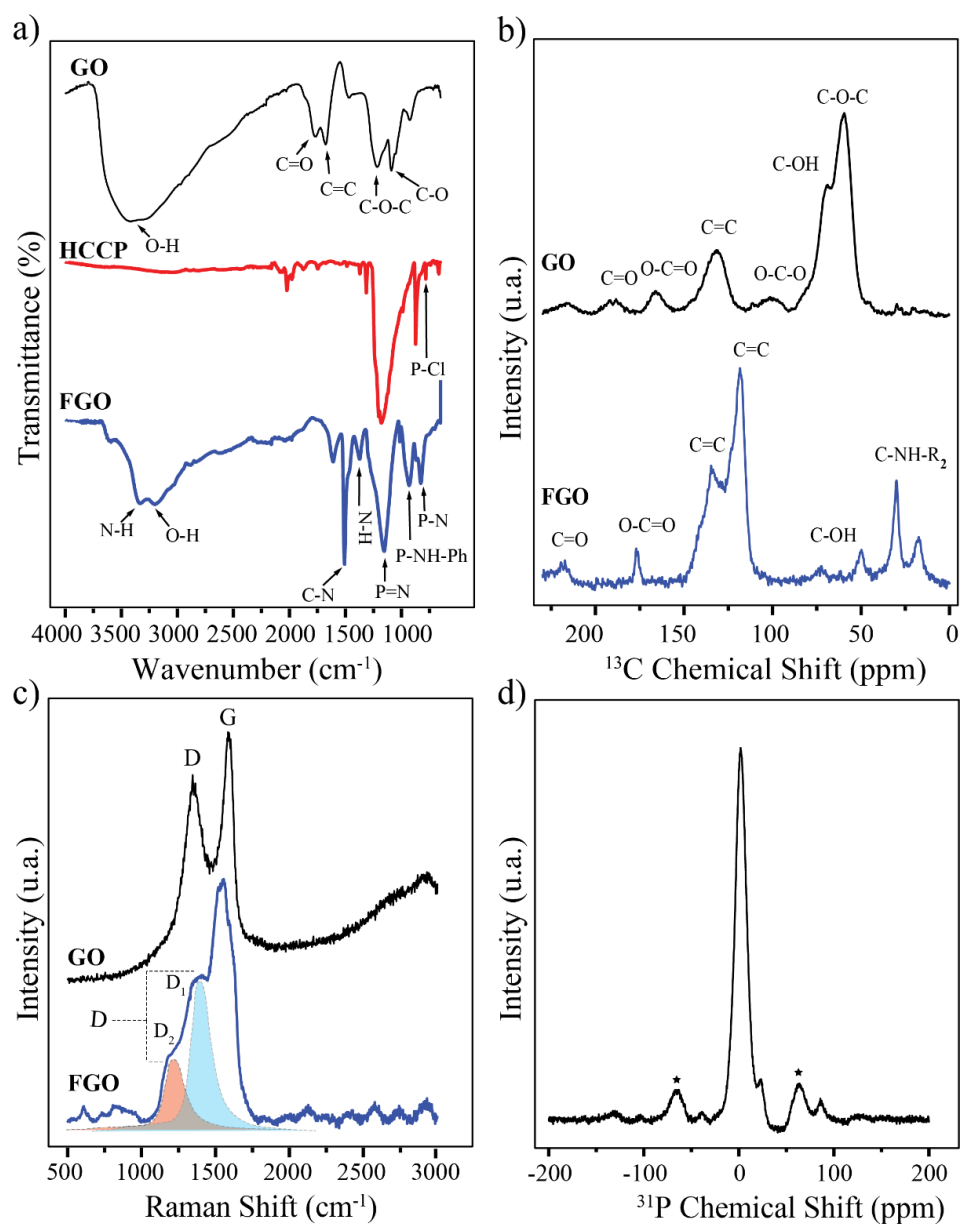
Figure 2.2   (a) FTIR spectra of GO, HCCP and FGO, (b) NMR spectra ^{13}C of GO and FGO, (c) Raman spectra of GO and FGO, (d) ^{31}P spectra of FGO

Solid-state NMR was used to clarify the molecular structure of FGO. The Solid state ^{13}C magic angle spinning (MAS) NMR spectrum of GO and FGO are depicted in (figure 2.2b), the NMR spectrum of GO reveals several peaks at 61 ppm (C-O-C), 70 ppm (C-OH), 101 ppm (O-C-O), 100-140 ppm (C=C sp^2), 164 ppm (C=O carboxylic acid) and 190 ppm (C=O), all are in good agreement with previously reported work (Aliyev, Filiz et al. 2019).

However, the typical GO resonances were also observed in the solid-state ^{13}C NMR spectrum of the FGO, with the appearance of new peaks at 0-50 ppm, which correspond to the amine bonds (C-NH-R$_2$). Moreover, two strong signals between 100 and 140 ppm associated to sp^2 carbon atoms are observed, suggesting that they are more graphite-like (Khandelwal and Kumar 2015). These results confirm that the *p*-PDA is indeed incorporated on the surface of GO. Solid state ^{31}P NMR was used to identify the chemical environments of phosphorus.

As shown in the figure 2.2d, a single peak at 2.5 ppm, confirming the total substitution of chlorines by amines. A very small peak appears at 18 ppm corresponds to unreacted P-Cl, as phosphorous would have different chemical environment. The peaks indicated with asterisks are sidebands (Crouzet and Leclercq 2000, Fan, Zhu et al. 2014).

XPS was employed to detect the surface composition and chemical component of GO and FGO, the results are tabulated in table A.1 and shown in figure A.3† (see Appendice A). The survey XPS spectrum of FGO shows three new peaks attributing to N 1s, P 2p and P 2s. Meanwhile, no Cl peaks is observed (figure A.3a), implying the Cl atoms in HCCP have been completely substituted with phenyl amine group of p-PDA (Zhang, Xu et al. 2019). High-resolution XPS spectra are shown in figure A.3 b.d.

The C 1s spectrum of GO (figure A.3b) presents four types of carbon: C-C (285.7 eV), C-OH (287.9 eV), C-O-C (288.6 eV) and C=O (289.7 eV), which is in good agreement

with earlier work results (Yuan, Bao et al. 2014, Yuan, Hu et al. 2017) C 1s spectrum of FGO (figure A.3c) also indicates the appearance of C-O-P/C-N groups (285.9 eV) (Yuan, Hu et al. 2017) which confirms the successful modification based on GO.

Furthermore, the intensity of oxygen functional groups in FGO decreases, which can be ascribed to the functionalization with polyphosphazenes containing phosphorus and nitrogen. The high-resolution spectra of N 1s for FGO (Figure a.3d) shows that there exist three chemical species of nitrogen: P=N (397.8 eV), P-NH-Ph (399.5 eV) and Ph-NH2 (400.1eV) (Zhang, Xu et al. 2014) suggesting that the HCCP and *p*-PDA were grafted onto the surface of the GO nanosheets.

The X-ray diffraction pattern was used to study the crystal structure and interlayer distance of nanosheets in GO and FGO. As shown in figure A.2†, the XRD pattern of pristine GO has a sharp diffraction peak located at $2\theta=10.09°$, indicating the crystalline structure of GO with the interlayer distance of 8.5Å, which corresponds to (002) plane due to the formation of oxygen-functional groups (Hydroxyl, carboxyl, and epoxy). A smaller peak appeared at $2\theta = 42.48°$ (d = 2.9 Å), corresponding to (100) plane, which is in good agreement with previously reported results (Marcano, Kosynkin et al. 2010).

However, in the XRD pattern of FGO, the (002) plane diffraction peak shifts to a higher-angle position at $2\theta = 15.62°$ leading to decrease in the interlayer distance d = 5.7Å by calculation with the Bragg equation (Pu, Ma et al. 2013) which indicates the conversion of GO into FGO. The peak corresponds to the (100) plane shifted to $2\theta = 47.25°$. A new weak peak was observed at $2\theta = 22°$ indicating that the π -π stacking of the GO was functionalized.(B 2018). Moreover, the presence of a board diffraction peak on the spectra at around $2\theta = 22$-$34°$, suggests that the structure of FGO is amorphous, which could be confirmed by selected area electron diffraction (SAED) patterns (figure A.4†).
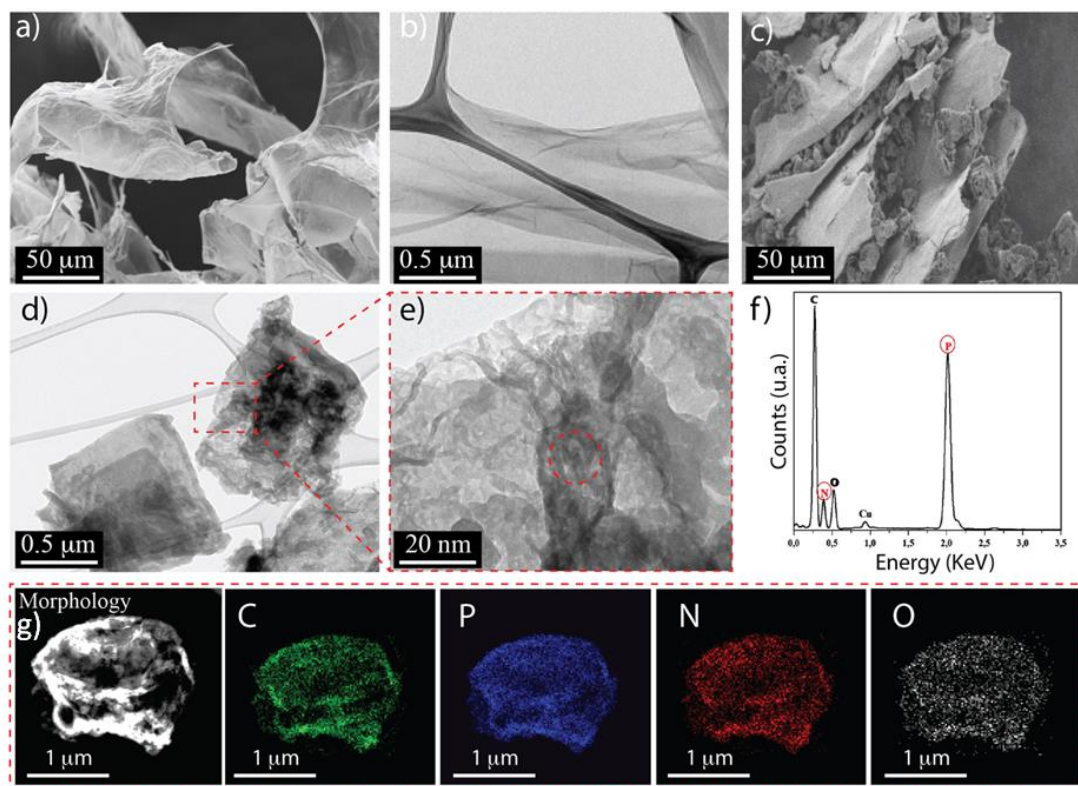
Figure 2.3   (a) SEM image GO, (b) TEM image of GO, (c) SEM image of FGO, (d) TEM image of FGO, (e) HRTEM of FGO, (f) TEM EDX spectrum of FGO and (g) Elemental mapping images of C, P, N and O components of FGO

The SEM image in figure 2.3a presents the morphology of the obtained GO in the form of wrinkled sheets separated from each other and closely linked together, which confirms the accuracy of our synthesis. Compared to GO, the SEM of FGO (figure2. 3c) shows a compact morphology which indicates that the functionalization has been achieved. With a higher magnification (figure 2.3b), the TEM image shows that the GO nanosheets are almost transparent and have no structural defect.

However, the TEM image of the FGO (figure 2.3d) demonstrates that a different structure with dark spots incorporated and distributed on the GO nanosheets. The high-resolution transmission electron microscopy image (HRTEM) of GO clearly shows the nature of nanosheets as well as the thickness of the GO (figure 2.3e). The spacing between two adjacent monolayers is 0.290 nm, which is consistent with the value of GO interlayer spacing of the (100) plane also obtained from SAED measurements (figure A.4A†).

Representative HRTEM and SAED images of the FGO are also shown in (figure A4B†), implying a low degree of crystallization. Energy dispersive X-ray spectroscopy (EDS) was used to follow the surface elements in FGO. The presence of N and P atoms on the FGO nanosheet is confirmed by signals in the EDX spectrum (figure 2.3f). Elementary mapping was performed to reveal the uniform distribution of atoms on the surface of the FGO: Phosphorus (blue), oxygen and chlorine (black), nitrogen (red) and carbon (green) (figure 2.3g).

TGA was used to follow the FGO thermal stability and the variation in mass loss for GO and functionalized GO with HCCP as a function of temperature under a nitrogen atmosphere (figure 2.4). As control experiment, compared to GO the TGA thermogram of HCCP clearly shows a sharp mass loss from 60 °C to 180 °C, which is attributed to the sublimation of HCCP. For freshly synthesized GO, the TGA thermogram shows three stages of mass loss. The first mass loss below 100 °C was attributed to the removal of residual moisture (Du, Wang et al. 2012). The second stage between

190-220 °C, corresponds to the decomposition of the various labile oxygen functional groups, such as the hydroxyl group (~36 wt%).

However, the last stage between 680-900 °C, corresponds to the total mass loss with about (~24wt%) char residues. Therefore, the GO is thermally unstable, indicating that it could not be used individually as an efficient flame retardant for polymers (Chen, Liu et al. 2018). After functionalization, FGO has a mass lossaround (~9 wt%) at a 190-220 °C range compared to that of the GO (~36 wt%), indicating that the thermal stability is greatly improved. The mass loss above 300 °C in the TGA curve of FGO principally belongs to the decomposition of HCCP. Importantly, the char residues of FGO between 680-900 °C is increased to (~39 wt%) compared to that of the GO (~24 wt%). Consequently, the good thermal stability for the FGO is explained by the elimination of the various oxygen-containing groups present on the GO, which were used as links with the HCCP.
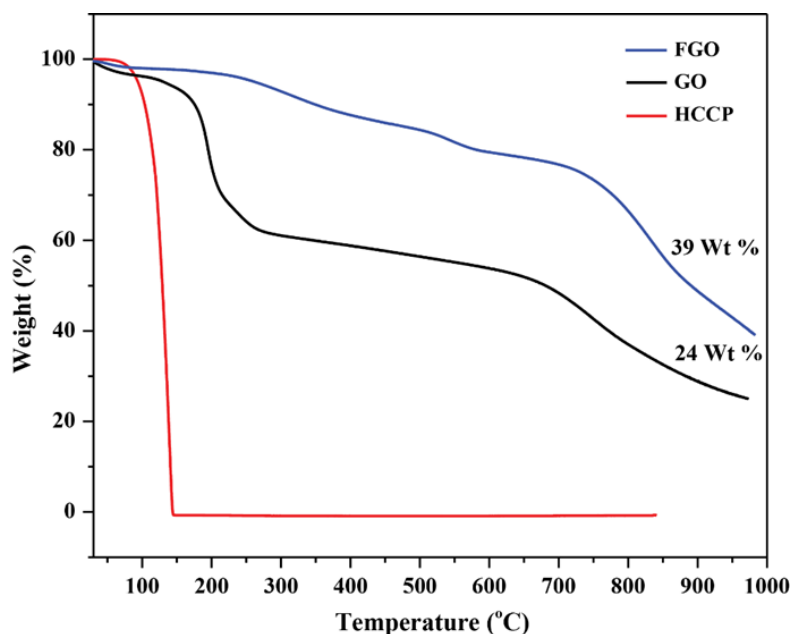
Figure 2.4   TGA curve of GO, HCCP and FGO

2.4.2   Thermal stability and thermal decomposition

The thermal stability of EP and its composites EP@GO and EP@FGO is investigated by TGA under a nitrogen atmosphere. TGA and differential thermogravimetric (DTG) curves are displayed in figure 2.5, and the detailed data are tabulated in table A.2. $T_{10\%}$ is defined as the temperature at which the mass loss is 10%. T_{max} is the temperature when the mass loss of the sample reaches its maximum. The degradation of pure EP and its composites have two mass loss stages.

The first stage is at 250-400 °C, it can be seen that the EP composites display a first maximum degradation temperature lower than that of the pure EP, which shows that the P-N-containing FRs decompose preferably at a lower temperature in order to catalyze carbonization of the EP matrix (Zhang, Xu et al. 2019). The second stage occurs between 400-500 °C, indicating that EP@FGO composites exhibit higher thermal stability than the pure EP. Therefore, EP@FGO composites decompose slower at high temperatures, due to the strong interfacial interactions between the FGO layers and the EP matrix, which can increase the thermal degradation activation energy of the composites (Bao, Guo et al. 2012).

As shown in table A.2, after pyrolysis at 800 °C the char yield ratio increases remarkably with increasing phosphorus and nitrogen content. The char yield of EP@FGO 2% is progressively increased to 18.3%, higher than those of pure EP or EP@GO 2%. Furthermore, the char yield of the EP@FGO composites is increased to 23% in EP@FGO 10%, which demonstrates that FGO can retard the decomposition of the composite. The main reason behind this phenomenon for this retarded decomposition is that FGO sheets are well distributed in EP matrix and form linkages with EP segments to effectively increase the intermolecular cross linkage density (Lei, Xia et al. 2016).

On the other hand, FGO catalyzes the char formation of polymer matrix EP due to HCCP, and therefore lower the rate of maximum mass loss to produce an additional protective residue rich in phosphorus and nitrogen. As shown in DTG curves (figure. 2b), it is clear that maximum mass loss rates of the composites are attenuated by FGO is about 45% (EP@FGO10%), because of the enhancement in the char formation and to the excellent physical barrier effect provided by the FGO sheets, which can decelerate the heat transfer (Chen, Liu et al. 2018).
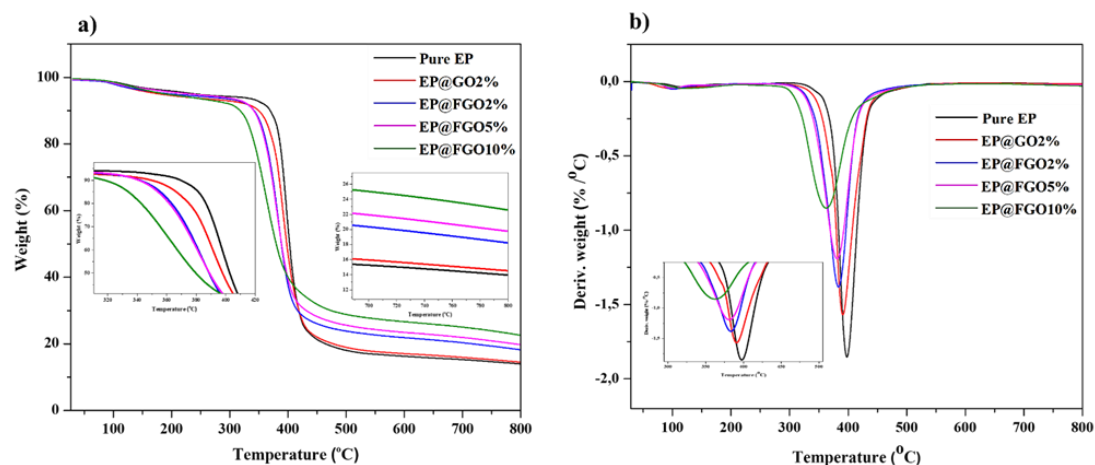
Figure 2.5   (a) TGA and (b) DTG thermograms of the pure epoxy EP and its composites under nitrogen

2.4.3   Flammability tests

In order to understand the different inflammability characteristics between EP, EP@GO and EP@FGO, a flame test was performed to confirm the flame-retardant effect. For this purpose, the different polymers have been modulated in the form of pellets for practical application (as shown in figure 2.6).
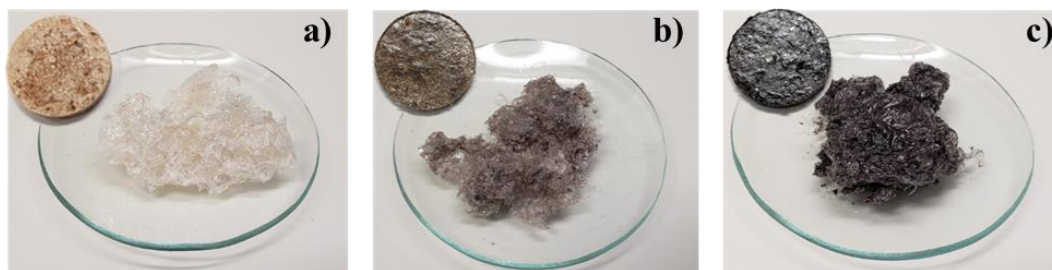
Figure 2.6   Photographic image of the different foams and pellets: (a) pure EP, (b) EP@GO and (c) EP@FGO

The sample pellets were exposed vertically to a Bunsen burner flame approaching the flame temperature of a fire, then were recorded by a digital camera at different stages of the combustion experiments and are shown in figure 2.7.
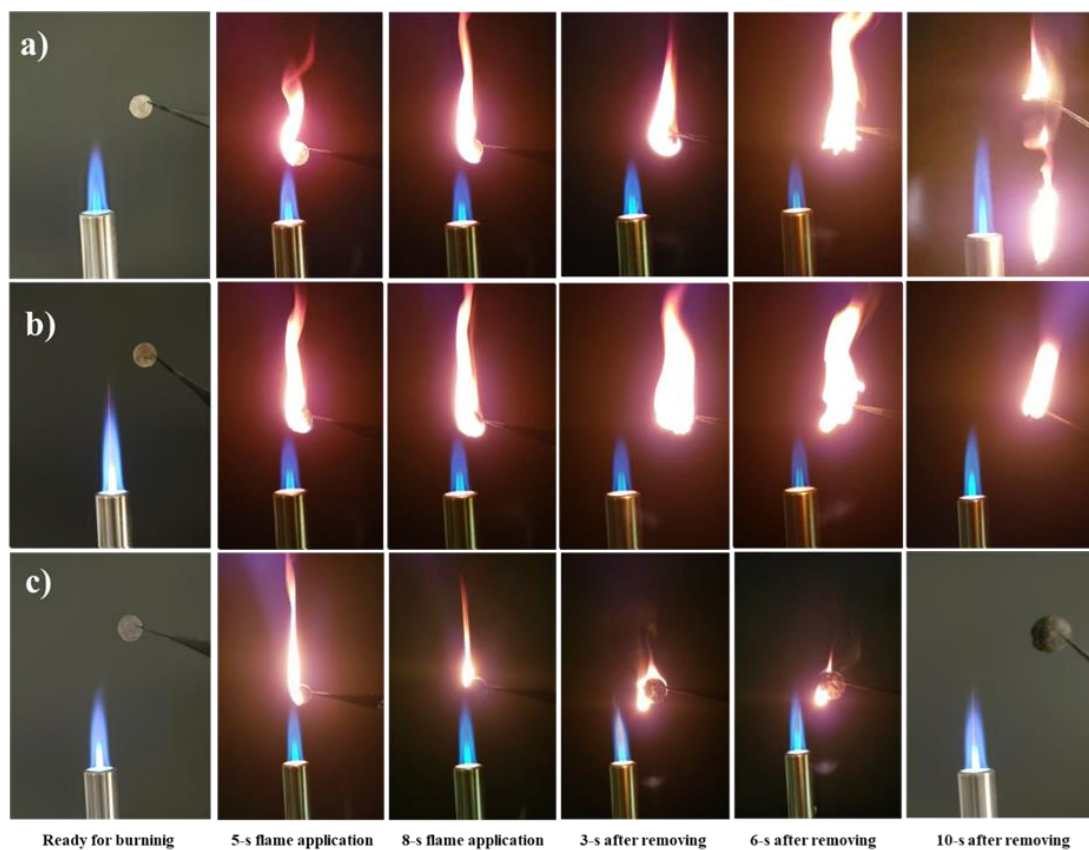
Figure 2.7   Photographs of the burning behavior of (a) Pure epoxy EP, (b) EP@GO and (c) EP@FGO during a vertical burning experiment

It is clearly observed from these photographs that the pellets of pure epoxy EP and its composite EP@GO immediately caught fire, releasing a large flame whose propagation was total, while the epoxy functionalized with flame retardant (EP/FGO) only exhibited slight combustion and almost non-existent propagation. After applying a flame for 8 s, the pure EP still burned with severe flaming drips, indicating a highly combustible behavior. However, in the case of the EP@FGO, one of the fascinating characteristics of the combustion is that it just burned lightly with a little flame and extinguished by itself within 10 s while keeping its initial form.

At the end of the combustion experiment, it is interesting to observe that part of the surface of the epoxy composite was covered with a network of expanded carbon, indicating that this epoxy composite formed an effective carbon that was able to impede heat transfer and the spread of flame during combustion. These results demonstrate the flammability of epoxy thermosets linked to phosphazene due to the presence of a unique combination of phosphorus and nitrogen. Finally, we have found the retarding effect has been produced with the incorporation of only 2% by weight of FGO in the epoxy resin EP.

2.5 Conclusion

A new method for the preparation of functionalized graphene oxide (FGO) is revealed in this study. The obtained FGO prepared via reaction of hexachlorocyclotriphosphazene and *p*-phenylendiamine with GO showed excellent thermal stability as shown by TGA analysis, as well as excellent flame-retardant capabilities as proved by flame tests. Effect of epoxy resins incorporation on GO and FGO was also studied, and experiments showed that EP@FGO showed much more enhanced fire resistance. Functionalization of graphene oxide by HCCP and PDD was closely monitored by different spectroscopic techniques including FTIR, Raman Spectroscopy, and Solid-State NMR.

Imaging techniques including SEM, EDX elemental mapping, XPS, and high-resolution TEM showed clear structural differences between GO and FGO, as well as proved the presence nitrogen and phosphorous on FGO. The incorporation of the phosphazene rings in the epoxy resin provides good non-flammability due to the unique combination of phosphorus and nitrogen. Further studies involving incorporation of different cyclophosphazene derivatives on GO and studying their potential electrochemical properties are currently underway.

2.6   Experimental Section

2.6.1   Experimental methods

2.6.1.1 Materials

Graphite powder (mesh size ≤100μm), *p*-Phenylenediamine (*p*-PDA), hexachlorocyclotriphosphazene (HCCP), potassium carbonate (K_2CO_3), concentrated sulfuric acid (H_2SO_4, 98%), potassium permanganate ($KMnO_4$), hydrogen peroxide aqueous solution (H_2O_2, 30%), phosphoric acid (H_3PO_4, 88%), hydrochloric acid (HCl), toluene, acetone, methanol, Bisphenol A. diglycidyl ether, (DGEBA) and *m*-phenylenediamine (*m*-PDA) were supplied from Sigma-Aldrich (Oakville, ON, Canada). De-ionised (DI) water was produced by a water purification machine (Milli-Q® Reference). Toluene was dried by 4 Å molecular sieves before being used.

2.6.2   Characterization Methods

Fourier transform infrared (FTIR) spectroscopy was acquired on a Nicolet smart iTR 6700 spectrometer in the wavenumber range of 4000–500 cm^{-1} (Thermo-Nicolet, Madison, WI). Data were analyzed using OMNIC® software (Thermo-Nicolet,

Madison, WI). The X-ray diffraction (XRD) was performed using a diffractometer (Bruker D8 Advance) with Cu-Kα radiation ($\lambda = 1.54182$ Å) in an angular interval from 20° to 100° at room temperature. X-ray photoelectron spectroscopy (XPS) data for elemental composition and valence information was collected with XPS PHI 5600-ci (Physical Electronics, Eden Prairie, MN, USA). The morphology of materials was obtained with a scanning electron microscope (SEM) by utilizing a JEOL (JSM7600F) operated at 10 kV accelerating voltage and a working distance of 14 mm using secondary electron imaging mode. Transmission electron microscopy (TEM) and Energy-dispersive X-ray spectroscopy (EDS) was performed on a Joel JEM-2100F.

Thermal gravimetric analysis (TGA Q500/Discovery MS) meter was used to measure the thermal stability under nitrogen (N_2) with a heat ramp of 5 °C /min between 30 and 1000 °C. Raman measurements were acquired on a Renishaw in Via microspectrometer using a 50X objective and a 514 nm laser wavelength. ^{13}C and ^{31}P MAS NMR spectra were recorded using a 400 MHz solid-state Bruker Advance III HD spectrometer (Milton, ON, Canada), operating at frequencies of 150.874 MHz for C^{13} and 162 MHz for P^{31}. Cross-polarization with the magic angle spinning (CP/MAS) technique was adopted.

2.6.3   Synthesis of the GO by the modified hummers method

Graphene oxide was obtained according to the modified Hummers method (Katsnelson, Novoselov et al. 2006). Briefly, (3 g) of graphite flakes was mixed with (360 ml) of concentrated acids H_2SO_4 and (40 ml) of 85% H_3PO_4. Then, 18 g of $KMnO_4$ was added gradually for 10 minutes. The reaction mixture was heated at 50 °C for 4 hours with continuous stirring. To promote exfoliation of graphite oxide, short periods of ultrasonication (4×) were applied every hour (15 min) during the reaction (4 h). When the reaction was over, the suspension was neutralized with a mixture of ice water containing 30% H_2O_2 (10 ml) with strong release of gas. The suspension was

centrifuged and washed several times with deionized water (250 mL) 10% HCl solution (250 mL) and anhydrous ethanol (2 x 250 mL).

The obtained light brown material was finally precipitated in anhydrous ether (1000 mL) and dried in a vacuum oven for 24 h at 40 °C yielding 4.9 g of a crude mixture of graphite/graphene oxide. Finally, the crude product (4.9 g) containing a mixture of graphite and graphene oxide was diluted in NanoPure water (1L) with stirring and sonication until complete homogenization to have a concentration of 4.9 g/L, and the solution was stored at room temperature.

2.6.4 Preparation of functionalized Graphene Oxide by hexachlorocyclotriphosphazene

Graphene oxide (100 mg) was dissolved in anhydrous toluene (10 mL), sonicated for 30 min at ambient temperature and then stirred with a mechanical stirrer to form a brownish black slurry. 1.40 g of K_2CO_3 was added to the GO suspension, and then HCCP (348 mg, 1 mmol) dissolved in toluene was added dropwise to the mixture with continuous stirring under N2 protection. Then (325 mg, 3 mmol) of *p*-PDA dissolved in toluene was slowly added to the mixture. Afterwards, the reaction was refluxed and maintained at 60 °C for 72 h. Finally, the obtained FGO was filtered by suction filtration and washed copiously with deionized water and methanol, and then dried under vacuum at 70 °C for 24h to yield a light violet-brownish solid.

2.6.5 Preparation of polymer composites EP@GO and EP@FGO

A flammable epoxy resin (EP) was carried to be mixed with GO and FGO (see the supporting information). The EP was prepared by mixing an epoxy precursor the bisphenol A diglycidyl ether (DGEBA) and the *m*-Phenylenediamine (*m*-PDA) as hardener (figure A.1†) (Liu, Tang et al. 2012). The main monomer of this type of resin

has two very electrophilic epoxy functions, which will react with different nucleophilic functions of graphene oxide (COOH and OH). In parallel, the hardener could react with epoxy functions as well as with halogenated reactive sites present on phosphazene. For flame retardant testing, various composite was carried out, such as the EP (100%), the EP loaded with graphene oxide (EP@GO) comprising 2% by mass ratio of (GO) and the EP loaded with the functionalized graphene oxide (EP@FGO), 2%, 5% and 10% as mass ratio of FGO in total mass. Prior to the composite preparation GO and FGO was dissolved in acetone, which we added to the prepared EP. The reaction mixture was stirred at 40 °C in a water bath to evaporate the acetone.

Finally, the mixture was kept in a vacuum oven at 80 °C for 45 minutes until the polymers (foams) become dray, see figure 2.6 in flammability tests section.

CHAPITRE III

ONE-POT SYNTHESIS OF CYCLOMATRIX TYPE POLYPHOSPHAZENEMICROSPHERES AND THEIR HIGH THERMAL STABILITY

Khaled Rhili[a], Siham Chergui[a], Ahmad Samih ElDouhaibi[b], Ahmed Mazzah[c] and Mohamed Siaj[a]*

[a] Department of Chemistry, University of Quebec at Montreal, Montreal QC, H3C3P8, Canada

[b] Department of Chemistry, Lebanese University, College of Science III, Campus Mont Michel, 1352, Tripoli, Lebanon

[c] Université de Lille, CNRS, USR 3290, MSAP, Miniaturisation pour la Synthèse, l'Analyse et la Protéomique, F-59000 Lille, France

Contribution des auteurs

KHALED RHILI

L'auteure principale a effectué toutes les manipulations expérimentales incluant la synthèse de produit ainsi que les caractérisations, la recherche bibliographique et les traitements des résultats. Aussi, elle a écrit la première version du manuscrit et a contribué à la version finale du manuscrit.

SIHAM CHERGUI

Le co-auteur a effectué des analyses et a participé à l'interprétation des résultats et la rédaction du manuscrit.

Ahmad Samih El Douhaibib

Le co-auteur a participé à l'interprétation des résultats et la rédaction du manuscrit.

Ahmed Mazzah

Le co-auteur a participé à l'interprétation des résultats et la rédaction du manuscrit.

MOHAMED SIAJ

L'auteur de correspondance a effectué la supervision des travaux et il a participé à l'interprétation des résultats, à l'écriture ainsi qu'à la révision finale du manuscrit.

ACS Omega, publié (2023).

3.1   Résumé

Une synthèse des cyclomatrix polyphosphazène type-microsphères par polymérisation en un seul pot entre l'hexachlorocyclotriphosphazène (HCCP) et la *p*-phénylènediamine (*p*-PDA) en présence de triéthylamine (TEA) en tant que produits ignifuges a été réalisé avec succès. Une résine époxy thermodurcissable a été préparée en incorporant différents pourcentages (2, 5 et 10 %) de C-PPZ à l'éther diglycidylique de bisphénol A (DGEBA). Les résultats révèlent que la taille et la morphologie des microsphères changent progressivement en changeant la température de 100, 120 et 200 ºC. La taille moyenne des C-CPPZ a progressivement augmenté de 3,12 µm, 4,9 µm à 7,7 µm, à mesure que la température est augmentée de 100, 120 à 200 ºC, respectivement. L'analyse thermogravimétrique (TGA) a montré que les microsphères de C-CPPZ ont une bonne stabilité thermique jusqu'à 900 ºC avec environ ~10 wt % de perte de masse pour les C-CPPZ formés à 200 ºC par rapport à ~30 wt % de perte de masse pour celles obtenues à 100 et 120 ºC. Les microsphères C-CPPZ résultantes ont été caractérisées par des techniques spectroscopiques et d'imagerie, notamment la spectroscopie infrarouge à transformée de Fourier, la spectroscopie Raman, la diffraction des rayons X, la microscopie électronique à balayage, la cartographie élémentaire par spectroscopie à rayons X à dispersion d'énergie et la spectroscopie photoélectronique à rayons X.

3.3   Introduction

Cyclomatrixpolyphosphazenes have attracted considerable interest in recent years (El-Kaderi, Hunt et al. 2007). Since their discovery, they have emerged as new inorganic material of various applications. They have exceptional attributes in various fields of interdisciplinary science such as metallo-organic and biomedical polymers, solid polyelectrolytes, and flame-retardant materials (Zhang, Cai et al. 2005). Their main starting material, hexachlorocycltriphosphazene (HCCP), is an essential material for synthesizing a variety of functionalized organocyclotriposphazenes (Carriedo 2007, Yeşilot and Uslu 2017), as well as a versatile network of functionalized amorphous porous organic polymers (POPs) (Zhu, Zhu et al. 2007) and covalent organic frameworks (COFs) (Zhang, Zhao et al. 2016, Zhang, Li et al. 2018). HCCP has also been used in preparation of functionalized dendrimers, which found various applications as catalysts and biosensors (Caminade, Hameau et al. 2016).

It is known that the most efficient flame-retardant additives are the halogen containing compounds, their use is limited and restricted because the combustion reaction products of halogenated additives exhibit higher toxicity. Another disadvantage is their harmful characteristics to the ozone layer of the atmosphere which has the negative impact on climate change. The phosphazene unit could be a good alternative to use as a starting point for the synthesis of halogen-free phosphazenes derivatives aiming to introduce flame retardant characteristics to organic polymers. Cyclomatrixpolycphosphazenes one of the important class of materials of the phosphazene chemistry, whether being crystalline or amorphous, have shown increased thermal stability and flame-retardant characteristics (Kumar, Fohlen et al. 1983, Kumar, Khullar et al. 1993).

Thermal stability of these polymers mainly depends on the linkages between phosphazene and other organic moieties, as well as the structure and particle size of the

cyclomatrix itself (Wan and Huang 2017). Studies have shown that the coexistence of nitrogen and phosphorous compounds in an organic polymer can undoubtedly lead to the nonflammability and high thermal stability of the polymer (Shieh and Wang 2002, Gao, Wang et al. 2008). More recent studies have shown that the inclusion of P and S atoms as linkages to HCCP further increased their thermal stability (Jian, Wang et al. 2016, Guo, Wang et al. 2018). For example, Xu et al. reported the synthesis of phosphorous-nitrogen-sulfur containing microspheres using HCCP and sulfonyldiphenol as starting materials. The product obtained showed very good thermal stability, showing about 55% weight loss at the end of 800 ^{o}C (Guo, Wang et al. 2018).

Li and Ma et al. designed a micro-porous phosphazene based covalent organic framework by reacting HCCP with p-phenylenediamine. The product was highly thermally stable, with about 45% weight loss at 800 ^{o}C (Zhang, Zhao et al. 2016). Huang et al. showed that inclusion of oxygen linkers, such as Phloroglucinol, in the cyclophosphazene polymer drastically increased thermal stability up to less than 30 % weight loss at 800 ^{o}C (Pan, Huang et al. 2012). Though the 800 ^{o}C threshold temperature attained by numerous cyclophosphazene frameworks is considered good, preparation of such class of polymers reaching such a temperature with minimum weight loss remains a quest. A water triggered polycondensation reaction of HCCP with amino acid esters reported by Lu et al. produced a mixture of cyclomatrixphosphazene nanoparticles bearing unsubstituted P-Cl moieties as proved by ^{31}P solid state NMR studies (Huang, Chen et al. 2015).

Though SEM data showed aggregations of perfectly spherical particles with different diameters, complete polycondensation where Cl atom were all being substituted could not be obtained, and the thermal stability of the cyclomatrix showed about 55 % weight loss at only 600 ^{o}C (Guo, Wang et al. 2018). In an attempt to further study the temperature effect on the structure and geometry of amorphous cyclomatrixphosphazene, and further improve their thermal stability, we report a

simple one pot hydrothermal polymerization method for preparing cross-linked polyphosphazene micro-spheres with controllable particle size by tuning the synthesis temperature, using hexachlorocyclotriphosphazene (HCCP) and *p*-phenylenediamine as co-monomers. We found that the temperature plays a determinant role to reach complete $-NH_2$-Cl substitution. The resulting product exhibits a very high thermal stability which could be used as fire retardant and could find other electrochemical applications.

3.4   Results and Discussion

3.4.1   Synthesis and characterization of C-PPZs

The synthesis of C-PPZs shown in figure 3.1, was prepared successfully via a one-pot and basic polymerization technique. HCCP is a crosslinker molecule having six reactive chlorine atoms. These features provide high cross-linking ability to HCCP. TEA was used as a base just to consume the hydrogen chloride (HCl) that is released from the polymerization reaction of HCCP and *p*-PDA and forms TEA.HCl salt. The reaction was performed three times at three different temperatures with same molar ratios of starting materials. The reaction was run at 100 °C and 120 °C, in which the analytical data showed incomplete reaction, as reflected by NMR and IR studies.

However, increasing the temperature reaction to 200 °C resulted in complete reaction, as illustrated in figure 3.1.
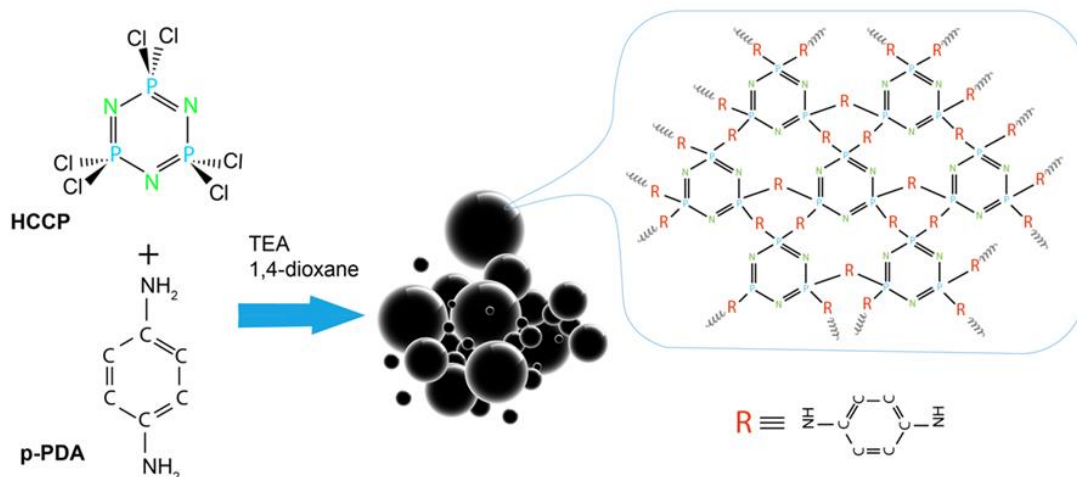
Figure 3.1   Synthetic route of C-PPZs microspheres

FTIR spectroscopy was used to identify the chemical structure of the obtained C-PPZs, as shown in figure 3.2a. The peaks in the region of 3100-3400 cm^{-1} correspond to the stretching vibrations of N-H (Rhili, Chergui et al. 2021). The aromatic skeleton vibrations are observed between 1505 and 1604 cm^{-1} (Hong, Li et al. 2018). The stretching band at 1170 cm^{-1} and 834 cm^{-1} are attributed to P=N and P-N characteristic absorption of the starting material (hexachlorocyclotriphosphazene) (Verma and Dutta 2015, Qu, Yang et al. 2017), respectively, which indicated that C-PPZs kept the skeleton structure of phosphazene during the reaction. Meanwhile, another important peak appearing at 938 cm^{-1} is associated to the stretching P-NH-Ph (Li, Qin et al. 2019), which obviously demonstrates the occurrence of copolymerization between HCCP and *p*-PDA. The P-Cl peak at 660 cm^{-1} of HCCP (Yuan, Hu et al. 2017) disappeared in the C-PPZs at 200 ºC, suggesting the complete substitution reaction of P-Cl in HCCP by *p*-PDA.
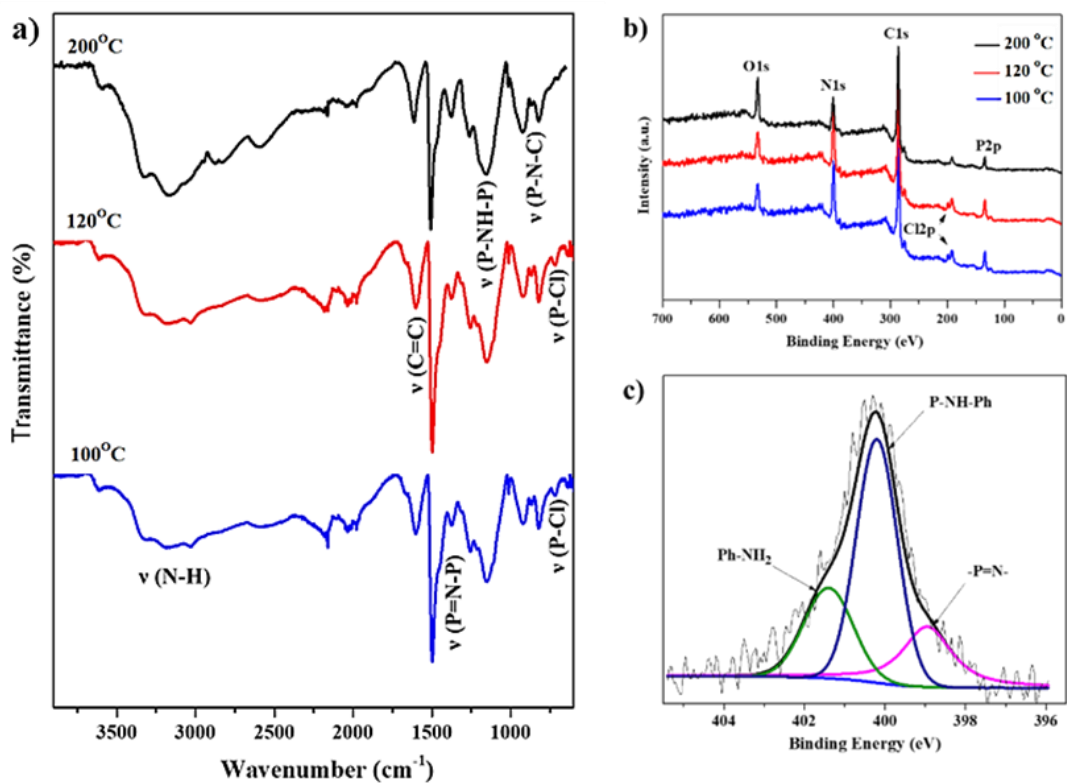
Figure 3.2   (a) FTIR spectra of C-PPZs microspheres obtained at different temperatures, (b) XPS survey spectra for C-CPZs microspheres and (c) high-resolution spectrum of N1s

High-resolution XPS was employed to detect the surface composition and the chemical component of C-CPPZs microspheres. The survey XPS spectra of C-CPPZs (figure 3. 2b) shows three peaks attributing to C1s, N1s, and O1s. A small amount of chlorine 1.7% and 1.9% was observed in C-CPPZs at 100 ^{o}C and 120 ^{o}C, respectively. Meanwhile, no Cl peaks in C-CPPZs at 200 ^{o}C, confirming that the Cl atoms in HCCP have been completely substituted by p-PDA (Rhili, Chergui et al. 2021). The high-resolution spectra of N1s for C-CPPZs microspheres at different temperatures (figure 3.2c) yield three peaks at about 397.5 eV, 399.4 eV and 400.2 eV, corresponding to P=N, P-NH-Ph and Ph-NH$_2$ bonds (Zhang, Xu et al. 2014, Zhang, Zhao et al. 2016), respectively. These results indicate the occurrence of polycondensation between HCCP and p-PDA.

Thermal stability of the C-PPZs microspheres was investigated by TGA analysis as shown in figure 3.3a. It shows that C-PPZs at 200 ^{o}C is more stable, having initial degradation at around 300 ^{o}C, while C-PPZs at 120 and 100 ^{o}C show similar behaviour, having initial degradation at around 180 ^{o}C which can be due to the incomplete reaction. C-PPZs at 200 ^{o}C showed excellent thermal stability, showing only 25% weight loss at 800 ^{o}C (you mentioned in the abstract that the weight loss was 10% at 900 ^{o}C, here you say it is 25% at 800 ^{o}C, please check the accurate values). Also, the improved thermal stability of the CPPZs microspheres compared with HCCP and p-PDA (Figure B.1) is due to the formation of a highly crosslinking structure and the thermally stable of cyclotriphosphazene rings (Wang, Fu et al. 2015).

The phase structure of the C-PPZs microspheres was checked by using power X-ray diffraction (XRD), as shown in Figure 3.3b. Two broad diffraction peaks at 2θ values of around 12° and 26° were observed, which confirms the amorphous structure of the PZS microspheres without any crystallization (Fu, Huang et al. 2008).
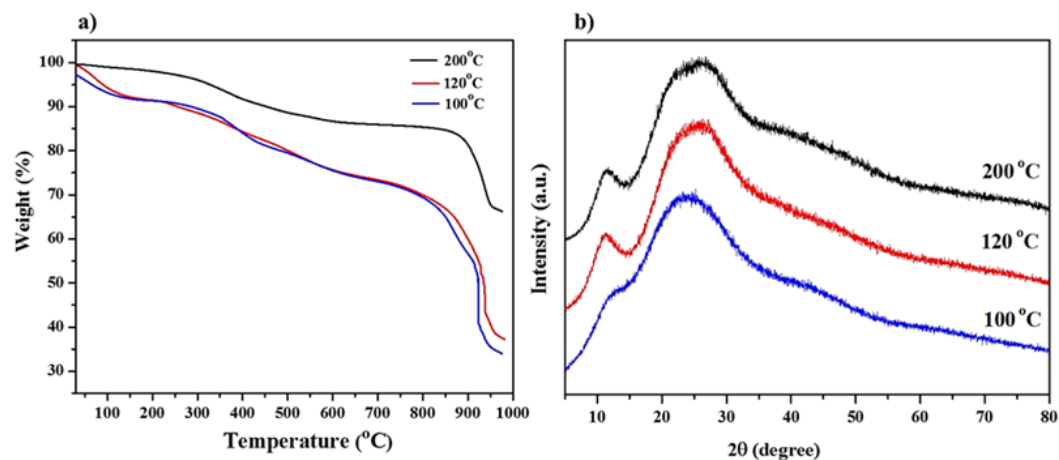
Figure 3.3   (a) TGA curves of C-PPZs microspheres under nitrogen and (b) X-ray diffractogram patterns of C-PPZs microspheres

The chemical structures of the C-PPZs are characterized by ^{13}C and ^{31}P CP/MAS NMR spectroscopy, as shown in figure 3. ^{13}C CP/MAS NMR spectra of C-PPZs obtained at 100 and 120 °C showed carbon chemical shifts as broad peaks at 118 ppm (C=C) and at 134 ppm (=C-N-P) in the aromatic region. Two smaller shoulders at 123 and 140 ppm were observed in the spectra, suggesting that more than one *p*-PDA moiety chemical environment exist in C-PPZs at 100 and 120 °C, that could be attributed to the presence of unreacting NH_2 moieties in *p*-PDA (figure 3.4a).

The ^{13}C CP/MAS NMR spectrum of C-PPZs obtained at 200 °C showed clearly only two single peaks in the aromatic region at 118 ppm and 134 ppm, thus indicating that *p*-PDA had substituted all Cl atoms of HCCP (Zhu, Zhu et al. 2007). As reflected by ^{31}P NMR (figure 4a), the spectrum of C-PPZs microspheres showed a major sharp phosphorous peaks appearing at 3.1 and 2.6 ppm in C-PPZs at 100 and 120 °C, respectively with an observed shoulder on the left of the peak in each spectrum, indicating the presence of structural units -N=P(-(NHPh))- and –N=P(-Cl)-, i.e, the

existence of different chemical environments for phosphorus atoms in the cyclophosphazene moiety of the cyclomatrix, which can be attributed to the incomplete substitution of all the Cl atoms by *p*-PDA (Dar, Ali et al. 2016).

In addition to the NMR data, the existence of unreacted chlorine is confirmed by EDS (figure 3.4). However, for the C-PPZs obtained at 200 ºC exhibit a single sharp phosphorous ^{31}P NMR peak appears at 2.8 ppm, indicating one phosphorous chemical environment and a complete substitution reaction.
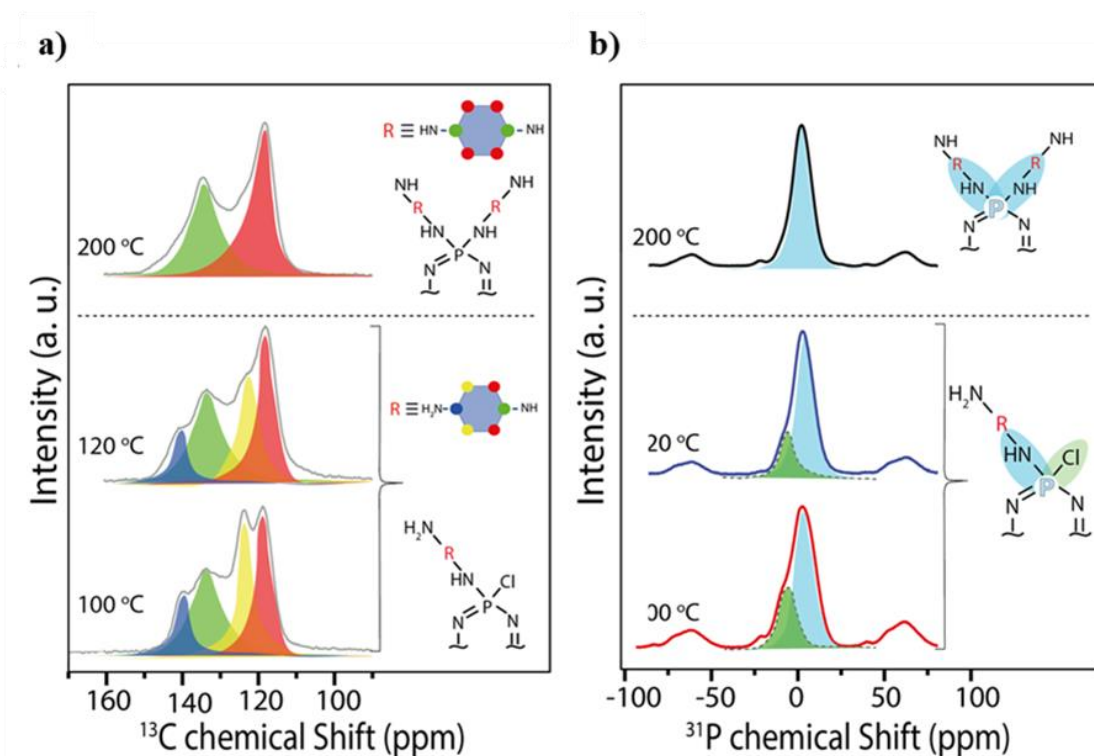
Figure 3.4   (a) Solid-state ^{13}C CP/MAS NMR spectrum of C-PPZs microspheres and (b) Solid-state ^{31}P CP/MAS NMR spectrum of C-PPZs microspheres

Figure 3.5 shows the SEM and TEM images of C-PPZs microspheres at different temperatures. The morphology of microspheres gradually changed by changing the temperature to 100, 120 and 200 $^{\circ}$C (figure 3.5a). The morphology of C-PPZs at 100 $^{\circ}$C adopts a deformed spherical-like structure, which could be explained by the presence of unsubstituted Cl atoms on the cyclophosphazene moiety of the cyclomatrix. The same behavior is noted for 120 $^{\circ}$C and 100 $^{\circ}$C with less deformed spherical C-PPZs structure. The obtained C-PPZs at 200 $^{\circ}$C adopts a complete spherical structure with all spheres perfectly tangents to each other, and this is due to the completely symmetrical structure of cyclomatrix which contains almost no Cl atoms in the cyclophosphazene ring system according to Energy-dispersive X-ray spectroscopy (EDX) and NMR data. EDX data show relatively high percentage of Cl in C-PPZs at 100 $^{\circ}$C (5.1%) compared to the obtained C-PPZs at 120 $^{\circ}$C (2.9%) and 200 $^{\circ}$C (0.2%). The gradually decreasing amount of Cl by 25 times from 100 $^{\circ}$C to 200 $^{\circ}$C confirm the proposed postulate that the resulting deformed spherical shape is related to the incomplete displacement of Cl atoms by *p*-PDA. In addition, the EDX-mapping indicated a uniform distribution of N, O, C, P and unsubstituted Cl over the cyclomatrix microspheres.
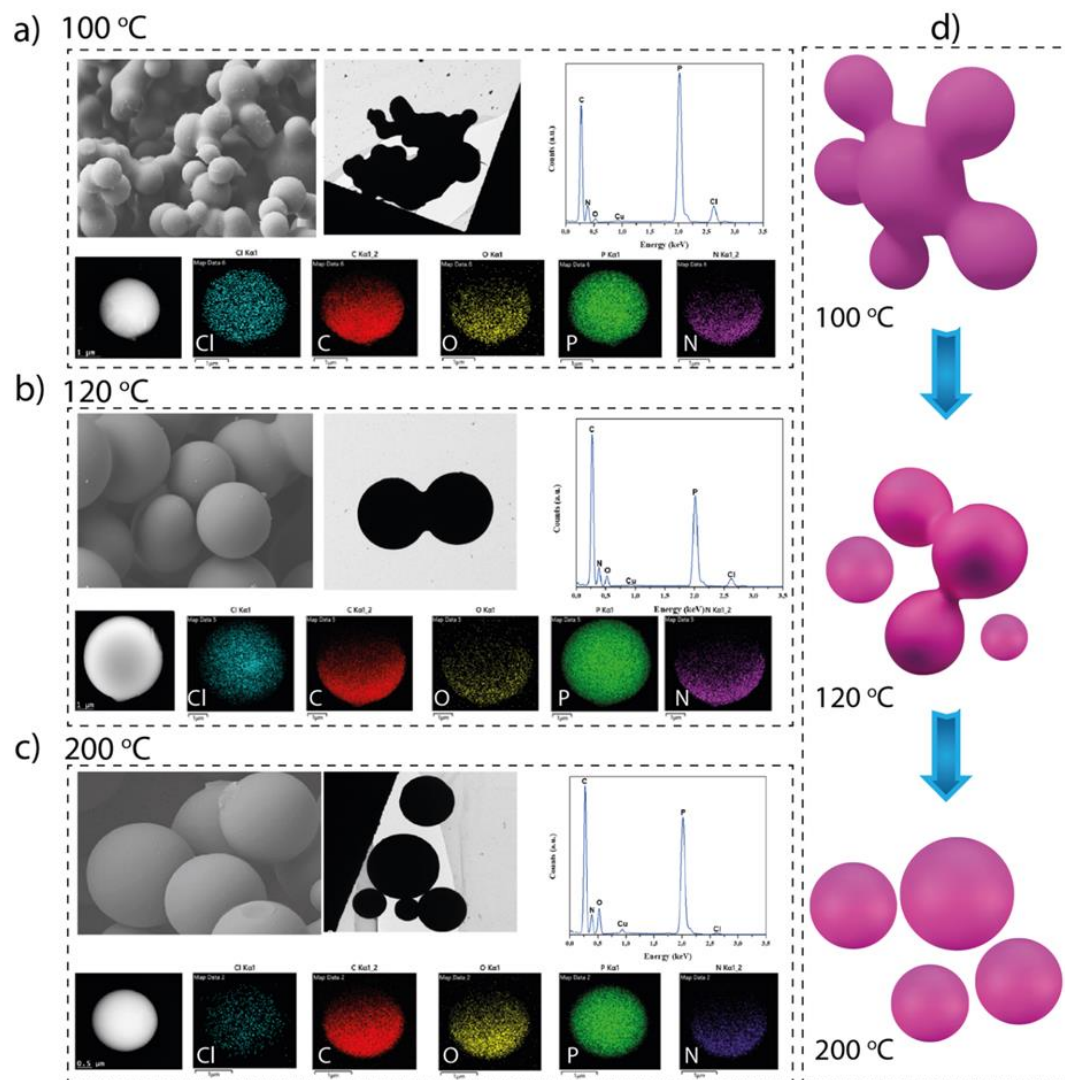
Figure 3.5   SEM, TEM images, TEM EDS spectra, Elemental mapping images of N, O, C, P and Cl of C-CPZs of microspheres at different temperatures: (a) 100 ^{o}C, (b) 120 ^{o}C and (c) 200 ^{o}C. Explanatory sketch showing the morphology as a function of temperature and the formation of distinct spheres at 200 ^{o}C (d) Growth kinetic of C-CPZs microspheres at different temperatures

Figure B.2 shows the particle-size distribution of the C-CPPZs microspheres at different temperatures. The average size of C-CPPZs gradually increased from 3.2 ± 0.7 µm, 4.9 ± 0.7 µm, to 7.7 ± 1.6 µm, as the temperatures are increased from 100 ℃, 120 ℃ to 200 ℃, respectively. So, the diameter increase is directly proportional to increase the temperature.

3.4.2   Thermal properties of EP@C-PPZs composites

The degradation of pure EP and its composites have two mass loss ranges. The first range is observed at 250-400 °C in the TGA analysis shown in figure 3.6. It can be seen that the EP composites display a first maximum degradation temperature lower than that of the pure EP, which shows that the phosphorus and nitrogen (P-N) containing flame retardants (FRs) decompose preferentially at a relatively low temperature, promoting char formation; Therefore and forming a protective layer that retards further degradation of the char at higher temperatures (Wang, Tai et al. 2011, Chiang and Yang 2015).

The second stage, which is the main mass-loss range, occurs between 400 and 500 °C. The EP@C-PPZs composites exhibit higher thermal stability than the pure EP in the second range because of the strong interfacial interactions between the polyphosphazene layers and the EP matrix (Zhang, Xu et al. 2019). As shown in Table S1, after pyrolysis at 900 °C, the char yield ratio of the EP@C-PPZs composites increases remarkably with increasing phosphorus and nitrogen content. The char yield of EP@FC-PPZs 2% is progressively increased to 17.7%, higher than the of pure EP, which demonstrates that C-PPZs can retard the decomposition of the composite. The main reason behind this phenomenon for this retarded decomposition is that C-PPZs sheets are well-distributed in the EP matrix and form linkages with EP segments to effectively increase the intermolecular cross-linkage density (Lei, Xia et al. 2016).

From DTG Curves (figure 3.6b), it is apparent that maximum mass loss rates of the composites are decreased by C-PPZs (Chen, Liu et al. 2018).
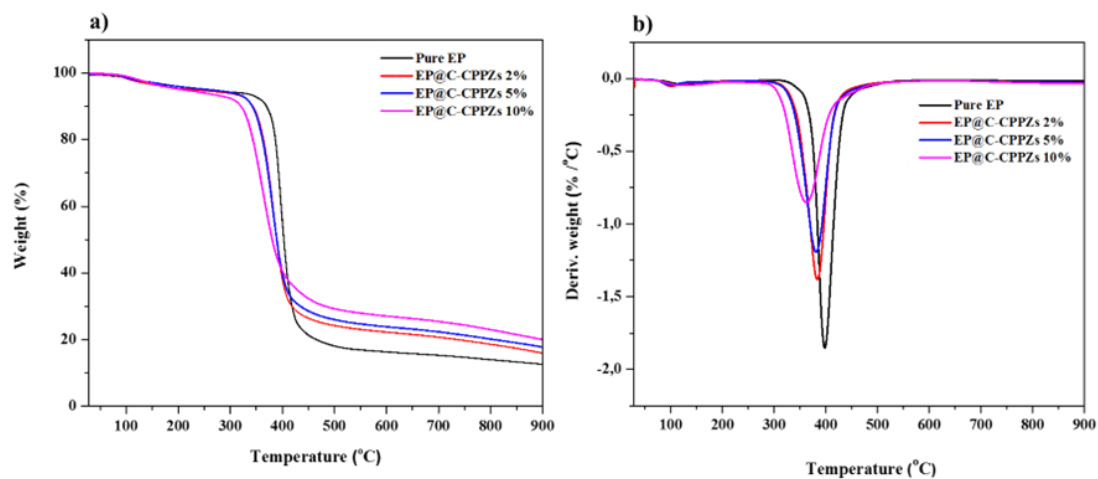
Figure 3.6   (a) TGA and (b) DTG thermograms of the pure epoxy EP and its composites under nitrogen

3.4.3   Flammability tests

We investigated the flame-retardant properties of pure EP and its composites EP@C-CPPZs 10% by direct exposure to an acetylene flame. For this purpose, the different polymers have been modulated in the form of pellets for practical application (as shown in scheme 1). Figure 3.7 demonstrates the typical burning procedures for the sample pellets. It is clearly observed from these photographs that the pellets of pure epoxy EP immediately caught fire, exhibiting a highly combustible behaviour, and left almost no residue after 10 s of combustion.

However, in the case of the C-PPZs, composites only exhibited slight combustion and almost nonexistent propagation. One of the fascinating characteristics of the

combustion is that it just burned lightly with a little flame even after repeated exposure to high temperature flame for 40 s while keeping its initial form. The excellent flame-retardant properties are mainly due to the formation of a high-quality barrier layer, which is based on the graphitic char from the HCCP-catalyzed char from the EP matrix (Chen, Liu et al. 2018).
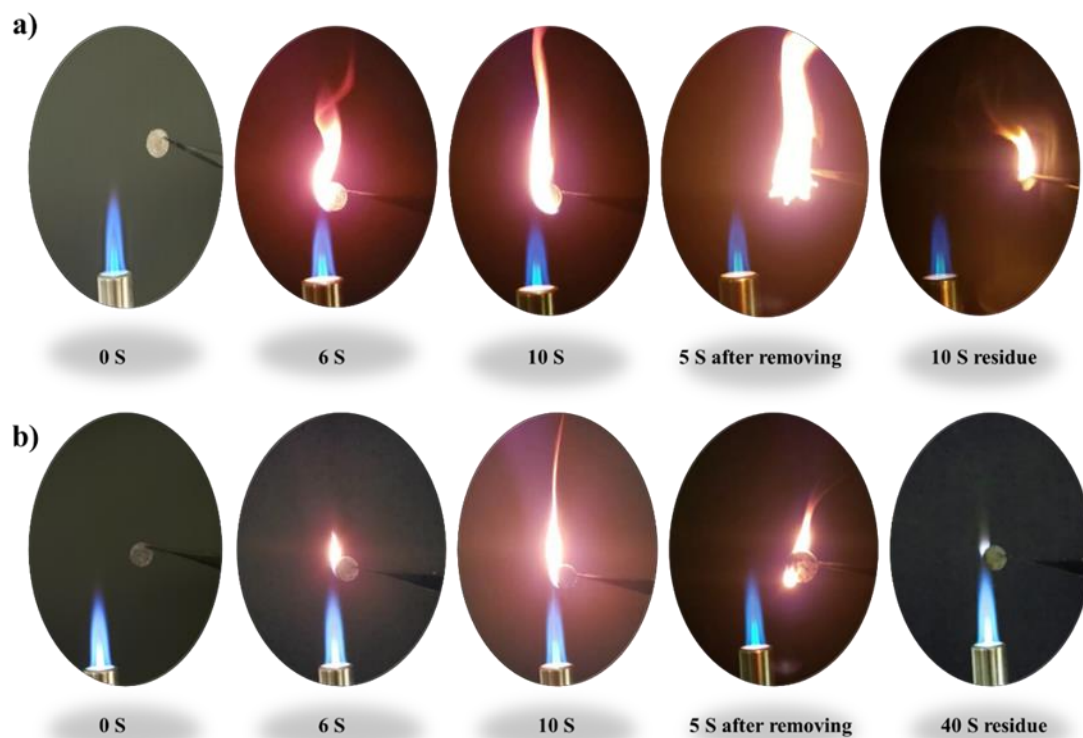
Figure 3.7   Photographs of the burning behavior of (a) Pure epoxy EP and (b) EP@C-CPPZs 10% during a vertical burning experiment

3.5   Experimental Section

3.5.1   Materials

Hexachlorocyclotriphosphazene (HCCP), *p*-Phenylenediamine (*p*-PDA), 1.4-Dioxane, ethanol, acetone, triethylamine (TEA) were purchased from Sigma-Aldrich (Oakville, ON, Canada). De-ionised (DI) water was produced by a water purification machine (Milli-Q® Reference). 1.4-Dioxane was dried by 4 Å molecular sieves before being used.

3.5.2   Characterization Methods

Fourier transform infrared (FTIR) spectroscopy was acquired on a Nicolet smart iTR 6700 spectrometers in the wavenumber range of 4000–500 cm^{-1} (Thermo-Nicolet, Madison, WI). Data were analyzed using OMNIC® software (Thermo-Nicolet, Madison, WI). The X-ray diffraction (XRD) was performed using a diffractometer (Bruker D8 Advance) with Cu-Kα radiation (λ = 1.54182 Å) in an angular interval from 5° to 80° at room temperature. X-ray photoelectron spectroscopy (XPS) data for elemental composition and valence information was collected with XPS PHI 5600-ci (Physical Electronics, Eden Prairie, MN, USA).

The morphology of materials was obtained with a scanning electron microscope (SEM) by utilizing a JEOL (JSM7600F) operated at 10 kV accelerating voltage and a working distance of 14 mm using secondary electron imaging mode. Transmission electron microscopy (TEM) and Energy-dispersive X-ray spectroscopy (EDX) was performed on a Joel JEM-2100F. The size and distribution of all as prepared nanoparticles were determined from SEM micrographs using ImageJ (V1.41, NIH, USA) for image analysis. Thermal gravimetric analysis (TGA Q500/Discovery MS) meter was used to

measure the thermal stability under nitrogen (N_2) with a heat ramp of 5 $^{\circ}$C /min between 30 and 1000 $^{\circ}$C. ^{13}C and ^{31}P MAS NMR spectra were recorded using a 400 MHz solid-state Bruker Avance III HD spectrometer (Milton, ON, Canada), operating at frequencies of 150.874 MHz for ^{13}C and 162 MHz for ^{31}P. Cross-polarization with the magic angle spinning (CP/MAS) technique was adopted.

3.5.3 Preparation of cyclomatrix type polyphosphazene microspheres (C-PPZs)

HCCP (348 mg, 1 mmol) and (p-PDA) (486 mg, 4.5 mmol) were dissolved in 15 mL of 1.4-Dioxane to form light purple suspension. Then, 1.74 mL of TEA was added. The suspension was transferred to an 80 mL Teflon-lined stainless-steel autoclave which was then sealed and heated in an oven and the reaction was run separately at three different temperatures: (100, 120 and 200 $^{\circ}$C) each for 24 h to prepare C-PPZs microspheres, which were named as C-PPZs-100, C-PPZs-120 and C-PPZs-200 $^{\circ}$C respectively. The products were left to gradually cool down to room temperature. The resulting powders were collected by centrifugation and washed with deionized water, ethanol and acetone three times, respectively. Then dried under vacuum at 80 $^{\circ}$C for overnight.

3.5.4 Preparation of polymer composites EP@C-PPZs

A flammable epoxy resin (EP) was mixed with C-PPZs (see the supporting information), which was described in our prior publication (figure A1) (Rhili, Chergui et al. 2021). Various amounts of C-PPZs were added to acetone and stirred until C-PPZs had completely dispersed to form a solution. Then, the C-PPZs solutions were separately added to the epoxy resin and stirred until homogeneous mixtures were obtained. The contents of C-PPZs were 0, 2, 5, and 10 wt %, and the resultant samples were marked as pure EP, EP@C-PPZs2%, EP@C-PPZs5%, and EP@C-PPZs10%,

respectively. In order to remove the solvent, the reaction mixture was stirred at 40 °C in a water bath. Finally, the mixture was put in a vacuum oven at 70 °C for 40 minutes until the polymers (foams) were completely dry, see figure 3.8.
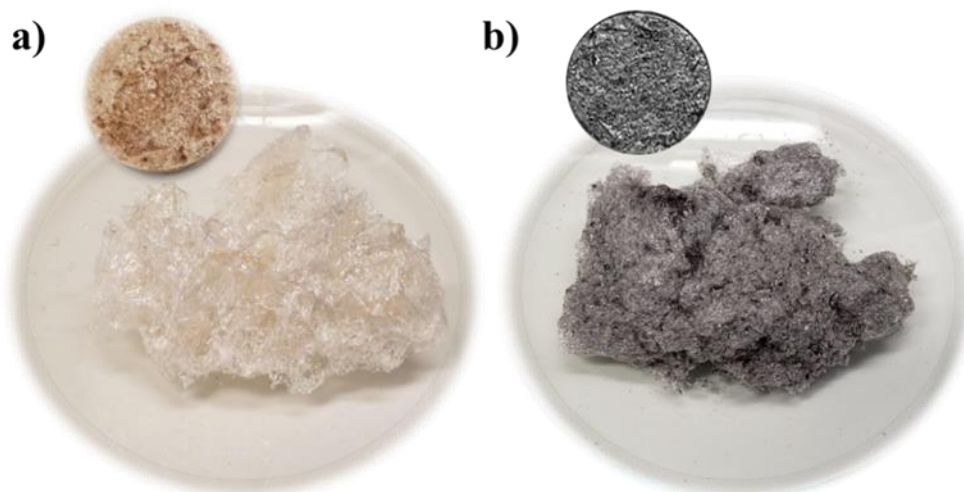
Figure 3.8   Photographic image of the different foams and pellets: (a) pure EP and (b) EP@C-PPZs

3.6   Conclusion

A simple and efficient method for synthesis of highly cross-linked cyclomatrixpolyphosphazenes from HCCP and *p*-PDA is disclosed. The study showed that morphology and reactivity of HCCP with *p*-PDA was highly temperature dependent. Solid state ^{13}C and ^{31}P NMR data showed that complete displacement of the Cl atoms in HCCP by *p*-PDA molecules took place at 200 °C, proving complete reaction, whereas incomplete reaction was observed at 100 °C and 120 °C. SEM and TEM analysis revealed that the average particle size of the cyclomatrices increased with temperature, and TGA analysis reflected excellent thermal stability for all

cyclomatrices obtained, the highest being to the cyclomatrices obtained at 200 ºC in which only 25% weight loss took place at 800 ºC. In addition, EP composites of the obtained CCPZs showed excellent flame-retardant properties. Studies on applications of these polyphospahzenecyclomatrices as well as other polyphosphazene materials in electrochemistry and other related fields are currently underway in our laboratories.

CHAPITRE IV

PHOSPHORUS AND NITROGEN CO-DOPED REDUCED GRAPHENE OXIDE AS SUPERIOR ELECTRODE MATERIALS FOR SUPERCAPACITORS

Khaled Rhili[a], Siham Chergui[a], Ahmad Samih El Douhaibi[b] and Mohamed Siaj [a,*]

[a]Department of Chemistry and Biochemistry, Université du Quebec à Montréal, Montréal QC, H3C 3P8, Canada

[b] Department of Chemistry, Lebanese University, College of Science III, Campus Mont Michel, 1352, Tripoli, Lebanon

*Corresponding author at: Email: siaj.mohamed@uqam.ca

Contribution des auteurs

KHALED RHILI

L'auteure principale a effectué toutes les manipulations expérimentales incluant la synthèse de produit ainsi que les caractérisations, la recherche bibliographique et les traitements des résultats. Aussi, elle a écrit la première version du manuscrit et a contribué à la version finale du manuscrit.

SIHAM CHERGUI

Le co-auteur a effectué des analyses et a participé à l'interprétation des résultats et la rédaction du manuscrit.

Ahmad Samih El Douhaibib

Le co-auteur a participé à l'interprétation des résultats et la rédaction du manuscrit.

MOHAMED SIAJ

L'auteur de correspondance a effectué la supervision des travaux et il a participé à l'interprétation des résultats, à l'écriture ainsi qu'à la révision finale du manuscrit.

Materials Advances, publié (2023).

4.1   Résumé

En tant que l'un des dispositifs de stockage d'énergie rapide les plus prometteurs, les supercondensateurs ont attiré une attention particulière pour de nombreuses applications émergentes pour le stockage d'énergie électrique. Dans ce travail, un matériau d'oxyde de graphène réduit co-dopé phosphore / azote (PN-rGO) a été préparé par pyrolyse en une étape de l'oxyde de graphène fonctionnalisé (FGO), qui est généré par une fonctionnalisation de l'oxyde de graphène (GO) avec de l'hexachlorocyclotriphosphazène et p-phénylènediamine. Les résultats de la caractérisation indiquent que le PN-rGO a une structure poreuse avec une morphologie de couche mince, transparente et ridée.

Les mesures électrochimiques révèlent que le rGO non dopé et le PN-rGO présente des propriétés capacitives améliorées avec une capacité spécifique élevée de 292 F g^{-1} à 0,5 A g^{-1} et une capacité de débit remarquable. Après 10 000 cycles, une capacité de 97% est maintenue, démontrant une excellente stabilité de cycle. De plus, le supercondensateur symétrique assemblé à base de PN-rGO présente une densité d'énergie relativement élevée de 8,2 Whkg^{-1} et une densité de puissance de 570 Wkg^{-1} dans l'électrolyte KOH. Les performances exceptionnelles de ce matériau en tant qu'électrode de supercondensateur peuvent être attribuées à l'effet pseudocapacitif du co-dopage P, N des nanofeuilles de graphène ainsi qu'à une structure poreuse exceptionnelle.

4.2   Abstract

phosphorus/nitrogen co-doped reduced graphene oxide (PN-rGO) material has been prepared by one-step pyrolysis of the functionalized GO (FGO) with hexachlorocyclotriphosphazene and *p*-phenylenediamine. The resulting PN-rGO shows a porous structure with a transparent and wrinkled thin film morphology. Compared with the undoped rGO, the electrochemical measurements of PN-rGO exhibit enhanced capacitive properties, including high specific capacitance of 292 F g^{-1} at 0.5 A g^{-1}, remarkable rate capability, and excellent cycling stability (after 10 000 cycles, 97% capacitance is maintained). Moreover, the assembled symmetric supercapacitor using PN-rGO shows a relatively high energy density of 8.2 W h kg^{-1}at a power density of 570 W kg^{-1} in KOH electrolyte. The outstanding performance of this material as a supercapacitor electrode may be attributed to the pesudocapacitive effect of P/N co-doping in reduced graphene nanosheets, as well as its exceptional porous structure.

Keywords: Graphene oxide, PN co-doping reduced graphene oxide, supercapacitor, porous carbon.

4.3   Introduction

In recent years, carbon-doped heteroatoms have gained considerable research interest. Doping with heteroatoms makes it possible to increase the specific capacity and improve the electrochemical performance of carbonaceous materials (Raza, Ali et al. 2018, Wang, Wang et al. 2019). In addition, such materials have demonstrated electrochemical stability, good energy conversion and bio-imaging applications (Xiang, Cao et al. 2014, He, Han et al. 2016). Among the elements most used to dope carbonaceous materials are sulfur, boron, nitrogen, and phosphorus. For this purpose, nitrogen is the most widely used heteroatom to dope carbonaceous materials. This doping improves the electrical conductivity and the power of the surface of the doped material (Ren, Li et al. 2018, Wang, Li et al. 2019).

Several methods are used for the preparation of heteroatom-doped carbon materials, such as external doping (Wang, Li et al. 2019), direct pyrolysis (Ren, Li et al. 2018), polymers (Hu, Zhu et al. 2018), as well as commonly used nitrogen-rich precursors (Song, Yang et al. 2016). Polyphosphazenes are polymers with an alternation of phosphorous and nitrogen atoms (Allcock 2006, Chen, Huang et al. 2016) with different chemical structures and functionalities and can be used as precursors to prepare carbon materials (Allcock 2016, Zhang, Ali et al. 2016). Doping of porous carbon with nitrogen and phosphorus proved to have excellent capacitive performance (Allcock and Morozowich 2012, Zhang, Zhao et al. 2018). Nitrogen-doped carbon materials exhibit unique electronegativity that induces an efficient distribution of the electronic charge and thus allows the transport of electrons through the carbon.

Furthermore, the positive effect of the single doping can be amplified by co-doping causing a synergistic effect (Allcock, McDonnell et al. 1990, Liu, Zhang et al. 2018). Reports demonstrated phosphorus dopant (Tian, Hess et al. 2015), exhibits higher electron donation capacity than nitrogen (Momodu, Sylla et al. 2019).

Recently, N/P doping on porous carbons has been reported to have an excellent performance as an electrode for supercapacitors (Wang, Sun et al. 2013, Chen, Wei et al. 2018, Ma, Wu et al. 2019). Supercapacitors have attracted a remarkable attention as a component for the energy storage and a good alternative to batteries and fuel cells (Stoller and Ruoff 2010, Berrueta, Ursúa et al. 2019). They have distinctive proprieties with an excellent power density, long lifetime, fast charging and discharging speed and higher cycle stability (Shao , Li, An et al. 2019, Zhou, Vassallo et al. 2020).

Supercapacitors are grouped in two categories depending on their charge storage mechanisms: electrochemical double layer capacitors (EDLC) and pseudo-capacitors (Zhang, Feng et al. 2009, Chen, Rakhi et al. 2012). EDLCs use ion adsorption between electrode-electrolyte interface for energy storage whereas pseudo-capacitors store energy by fast and reversible faradic reactions. Several carbon based materials are largely used as electrode materials for as electrode materials for EDLCs such as activated carbon, mesoporous carbon (Sevilla and Mokaya 2014), graphene or reduced graphene oxide (rGO) and carbon aerogels (Pandolfo and Hollenkamp 2006, Inagaki 2010). These materials have become indispensable electrode materials because of their high surface area, porous structure and good electrical conductivity (Guo, Li et al. 2016, Sadak, Sundramoorthy et al. 2018).

For pseudo-capacitors, the most commonly used materials are conductive polymers and transition metal oxides (Jacob, Yang et al. 2009, Zhang, Feng et al. 2009). For this purpose, the performance of the energy storage device can be improved by increasing the surface area, the specific capacity reaches a plateau when the specific surface is higher than about 1500 m^2/g (Xia, Chen et al. 2009, Zhang, Gong et al. 2012).

In this work we report a method to prepare the nitrogen and phosphorus co-doped microporous derived rGO for supercapacitor application. The rGO material with thermal stability, high electrical conductivity, large surface area and broad

electrochemical window (Geim and Novoselov 2007, Liu, Yu et al. 2010) was used as electrodes in supercapacitors.

We believe this proposed study will provide an approach that is scalable for the preparation of new materials based on three-dimensional nitrogen and phosphorus co-doped reduced graphene oxide as superior electrode materials for supercapacitors.

4.4   Experimental methods

4.4.1   Materials

Graphite powder (mesh size ≤100μm), *p*-Phenylenediamine (*p*-PPD), hexachlorocyclotriphosphazene (HCCP), potassium carbonate (K_2CO_3), concentrated sulfuric acid (H_2SO_4, 98%), potassium permanganate ($KMnO_4$), hydrogen peroxide aqueous solution (H_2O_2, 30%), phosphoric acid (H_3PO_4, 88%), hydrochloric acid (HCl), toluene, acetone, methanol. De-ionised (DI) water was produced by a water purification machine (Milli-Q® Reference). Toluene was dried by 4 Å molecular sieves before being used.

4.4.2   Synthesis of functionalized graphene oxide (FGO) and P, N-doped reduced graphene oxide (PN-rGO)

The detailed synthesis of rGO is shown in Supporting Information. FGO was prepared by functionalizing the GO with hexachlorocyclotriphosphazene (HCCP) and *p*-phenylenediamine (*p*-PDA). In a typical experiment, 70 mg of graphene oxide was dispersed in anhydrous toluene (10 mL), sonicated for 30 min at ambient temperature to yield a dark brown suspension. 1.40 g of K_2CO_3 was added to the GO suspension, and then, HCCP (348 mg, 1 mmol) dissolved in toluene was added dropwise to the mixture with continuous stirring.

Then, 325 mg (3 mmol) of *p*-PDA dissolved in toluene was slowly added to the mixture. Afterward, the reaction was refluxed and maintained at 60 °C for 48h. The as prepared sample was washed and dried under vacuum at 70 °C for 24h to obtain FGO. Finally, the sample was annealed in a tubular furnace at 850 °C for 2 h with the ramping rate of 5 °C min^{-1} under an argon atmosphere and the corresponding sample is named PN-rGO. The typical synthesis procedure to PN-rGO is illustrated in figure 4.1.
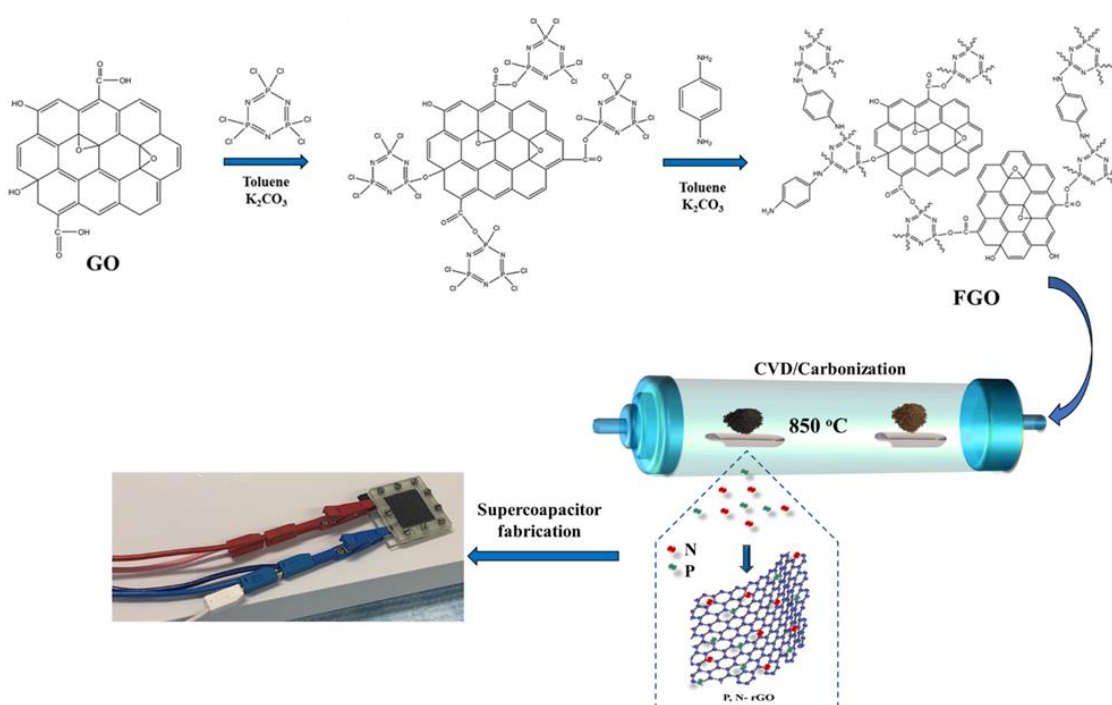
Figure 4.1   Schematic illustration of the fabrication process of the N, P co-doped reduced graphene oxide

4.4.3   Characterization Methods

The X-ray diffraction (XRD) was performed using a diffractometer (Bruker D8 Advance) with Cu-Kα radiation ($\lambda = 1.54182$ Å) in an angular interval from 20° to 100° at room temperature. X-ray photoelectron spectroscopy (XPS) data for elemental composition and valence information was collected with XPS PHI 5600-ci (Physical Electronics, Eden Prairie, MN, USA). The morphology of materials was obtained with a scanning electron microscope (SEM) by utilizing a JEOL (JSM7600F) operated at 10 kV accelerating voltage and a working distance of 14 mm using secondary electron imaging mode. Transmission electron microscopy (TEM) and Energy-dispersive X-ray spectroscopy (EDS) was performed on a Joel JEM-2100F. Raman measurements were acquired on a Renishaw in Via microspectrometer using a 50X objective and a 514 nm laser wavelength.

4.4.4   Electrochemical Tests

The electrochemical performance of the synthesized material was evaluated through cyclic voltammetry (CV), galvanostatic charge/discharge (GCD) and electrochemical impedance spectroscopy (EIS) in a typical three-electrode cell with 6 M KOH aqueous solution as the electrolyte. The working electrode was prepared by mixing the as prepared materials with 10 μL of Nafion™ solution (5 wt%) and1 mL water-ethanol solution with a volume ratio of 4:1, and the mix was then sonicated for 30 min. 18 μL of the resulting ink was drop-casted onto glassy carbon electrode (GC, A = 0.1256 cm^2) and dried in air at room temperature.

An Ag/AgCl electrode and a platinum wire were employed as reference electrode and counter electrode, respectively. CV curves were obtained at scan rates ranging from 5 to 100 mV s^{-1} with the voltage ranging from -1 V to 0 V. GCD curves were obtained at

current density ranging from 0.5 to 20 A g^{-1}. The EIS measurements were acquired in the frequency range from 100 kHz to 0.01 Hz.

To investigate the potential for practical applications, the performance of the synthesized material was then evaluated in a symmetric supercapacitor though CV, GDC and EIS. The supercapacitor device, shown in figure 4.8a, consisted of PN-rGO as both the positive and negative electrode materials. Toray (TGP-H-060) carbon paper sections (2 × 2 cm) was served as current collectors. Whatman 41 paper was used as separator, which was immersed in 6 M KOH electrolyte prior to assembly. A Silastic® ERTV Silicone Rubber element was added as gasket, and the set was sandwiched between two PMMA plates fabricated by computer numerical control (CNC) micromachining. The total mass loading of PN-rGO of positive and negative electrodes was 2 mg. All electrochemical experiments were performed on a Biologic SP-300 potentiate/galvanostatic controlled by EC-Lab software.

The specific capacitance (F g^{-1}) was determined from GCD curves according to Eq. (1)

$$C = \frac{I * \Delta t}{m * \Delta V} \tag{1}$$

where 'I' is the charge-discharge current (A); Δt is the discharge time (s); $\triangle$V is the potential window(V); and m is the active material loading in the working electrode (g). The energy (E, W h kg^{-1}) and power (P, Wkg^{-1}) densities were calculated from charge–discharge measurement using Eq. (2) and Eq. (3) respectively.

$$E = \frac{1}{2} C (\Delta V)^2 \tag{2}$$

Where 'C' is the specific capacitance; 'ΔV' is the voltage window of the assembled device.

$$P = \frac{E}{\Delta t}$$

where 'Δt' is the discharge time.

4.5   Results and Discussion

The mechanism of synthesis PN-rGO is summarized in scheme 1. In first step, The FGO was synthesized by functionalizing the GO with hexachlorocyclotriphosphazene (HCCP) and *p*-phenylenediamine (*p*-PDA). Afterwards, the sample was annealed in a tubular furnace at 850 °C for 2 h with a ramp rate of 5 °C min^{-1} under Argon atmosphere. For comparison, the rGO was also prepared by following the same preparation process without the addition of HCCP and (*p*-PDA). The morphologies of the obtained materials were characterized by scanning electron microscopy (SEM) and transmission electron microscopy (TEM), as shown in figure 4.2a, b and (figure C.1a Appendix C).

From figure C.1a, it can be observed that the GO sheets are almost transparent with some wrinkled structures. Compared to GO, the surface of FGO (figure C.1b) appears to be rough, which indicates that the functionalization has been realized. Figure 4.2a indicates the SEM image of rGO, which exhibits wrinkled sheets and randomly aggregated to a certain degree that led to the formation of well-developed mesopores (Liu, Zhou et al. 2013, Lin, Ma et al. 2018). As can be seen in figure 4.2b ultrathin, crumpled PN-rGO nanosheets are partially aggregated and crumpled structure, originating from the defective sites created after the incorporation of nitrogen and phosphorus atoms into the graphene layer.

With a higher magnification, as displayed in figure 4.2c, the TEM image shows the rGO nanosheets are almost transparent with some wrinkles on the surface and have no structural defect. However, the TEM image of PN-rGO (figure 4.2d) shows a microporous structure, rough and clearly covered by nanoparticles distributed on the rGO, confirming the successful doping of nitrogen and phosphorus heteroatoms. In addition, the presence of N and P atoms on the PN-rGO is confirmed by signals in the EDX spectrum (figure 4.2e). Elementary mapping (figure 4.2f) was performed to reveal the homogeneous distribution of atoms on the surface of teen-age: carbon (red), phosphorus (purple), nitrogen (yellow), and (green) oxygen.
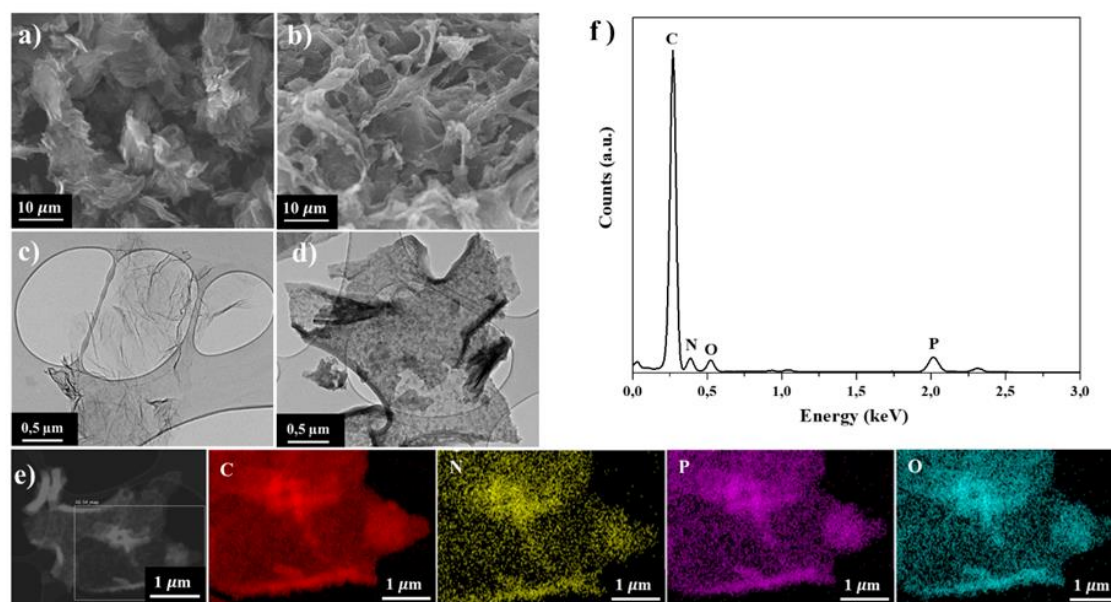
Figure 4.2   SEM images of (a) rGO and (b) PN-rGO, TEM images of (c) rGO and (d) PN-rGO, (d) TEM-EDX spectrum of PN-rGO, (e) Elemental mapping images of C, P, N, and O components of PN-rGO

XPS was used to investigate the elemental composition and chemical components of PN-rGO material. As shown in figure 4.3a, the survey XPS spectrum of PN-rGO presents four peaks according to C1s (285 eV), N1s (400 eV), O1s (533 eV) and P2p (133 eV), proving the successful P, N co-doping in graphene lattices (Yang, Bhattacharjya et al. 2012, Yang, Zhi et al. 2012). According to the XPS results, the atomic ratios of N and P are 2.3% and 4.5%, respectively (table C.1). The presence of oxygen in PN-rGO is attributed to the remaining oxygen functional groups (Wei, Liu et al. 2009).

Figure 4.3b shows the C 1s spectra of PN-rGO, which can be deconvoluted into four peaks located at about 284.7, 285.4, 286.6, and 289.1 eV, corresponding to C-C, C-O/C-N, C-P and O-C=O, respectively (Zhang, Jiang et al. 2011, Ma, Wu et al. 2019, Li, Lv et al. 2021). The N 1s spectrum (figure 4.3c) is fitted into three main peaks situated at 398.4 eV, 401.3 eV and 399.7 eV, corresponding to pyridinic-N, graphitic-N, and pyrrolic-N species, respectively (Lai, Potts et al. 2012, Ananthanarayanan, Wang et al. 2015). The pyridine-N and pyrrolic-N can significantly modify the electronic structure of the material and create active sites to improve the energy density of the supercapacitor (Ananthanarayanan, Wang et al. 2015, Li, Wang et al. 2020).

Furthermore, graphitic-N is beneficial in improving the electrical conductivity of carbon to reduce the resistance to charge transfer (Rct) during the charge/discharge process (Hulicova-Jurcakova, Seredych et al. 2009). Meanwhile, the P 2p spectrum (figure 4.3d) is deconvoluted into two components peaks at 131.8 and 133.9 eV which correspond to P-C and P-O bindings, respectively (Li, Dai et al. 2016).
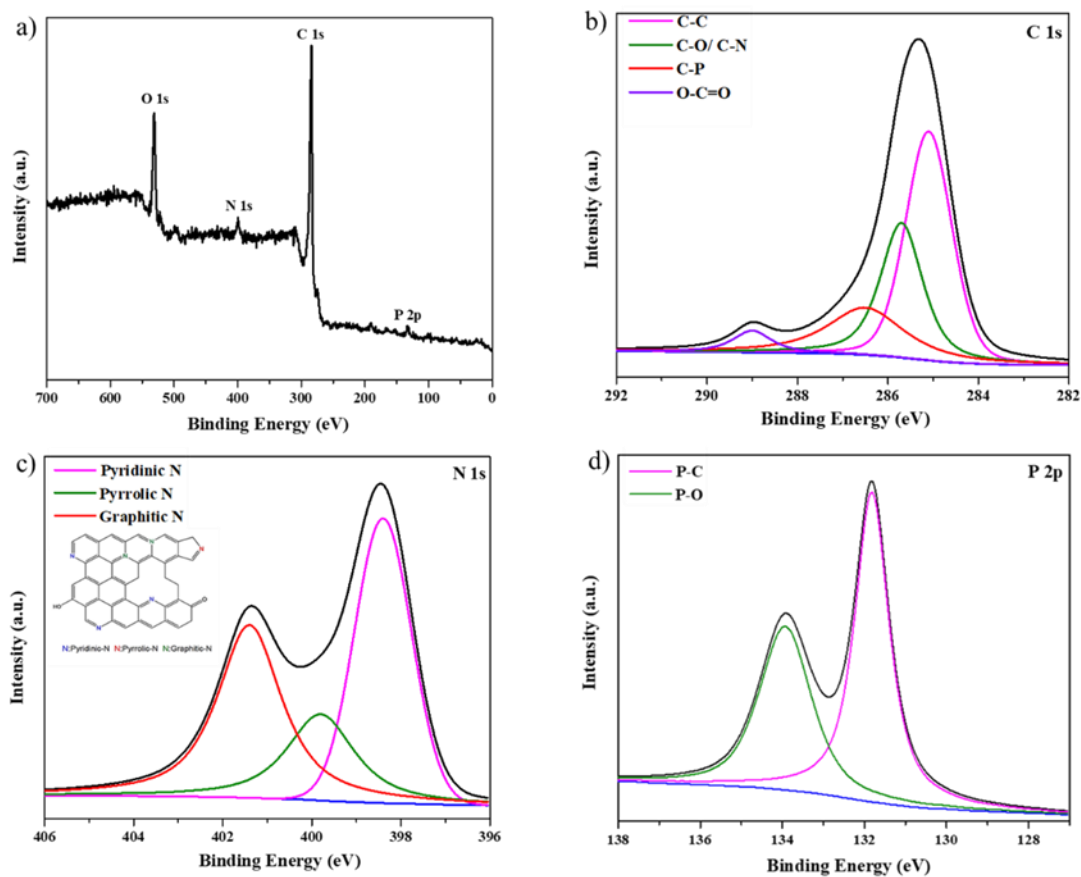
Figure 4.3 (a) XPS survey spectra of PN-rGO, High-resolution XPS spectra of the deconvoluted peaks of PN-rGO: (b) C 1s, (c) N 1s, and (d) P 2p, and spectra of the PN-rGO

Raman spectroscopy was used to investigate the quality of the carbon nanomaterials of GO, PN-rGO and rGO. As shown in figure 4.4a, two distinct peaks appeared at about1350 cm^{-1} and 1600 cm^{-1}, corresponding to the D band and G band, respectively (Rhili, Chergui et al. 2021). The D band is related to the disordered carbon atoms or to the defects in the structure (Verma and Dutta 2015), while the G band is associated with the ordered graphitic structure, and it is originating from the stretching vibrations of sp2 carbon atoms (Pimenta, Dresselhaus et al. 2007). Moreover, the intensity ratio value (I_D/I_G) leads to the defect degree of the materials. The *ID/IG* peak intensity ratios of GO, PN-rGO and rGO are 0.83, 0.89, and 0.84, respectively, which means PN-rGO has more defects compared with GO and rGO due to the incorporated phosphorus and nitrogen atoms in the graphitic plane (Gao, Fu et al. 2018).

The X-ray diffraction (XRD) pattern was used to study the structure information and crystal phase of the samples. Figure 4.4b shows the XRD patterns of GO, PN-rGO and rGO. The XRD spectrum of GO exhibits a sharp diffraction peak at $2\theta = 10.1°$ with an interlayer distance of 0.8 nm, corresponding to plan (002) due to the formation of oxygen functional groups (hydroxyl, carboxyl, and epoxy) (Kaniyoor, Baby et al. 2010, Hu, Zhan et al. 2014, Rhili, Chergui et al. 2021). However, for rGO and PN-rGO, the diffraction peak at 10.1° completely disappeared after annealing, replaced by a broad peak at $2\theta = 24°$ with a d-spacing of 0.4 nm, revealing that the successful reduction of GO to reduced graphene oxide (rGO).
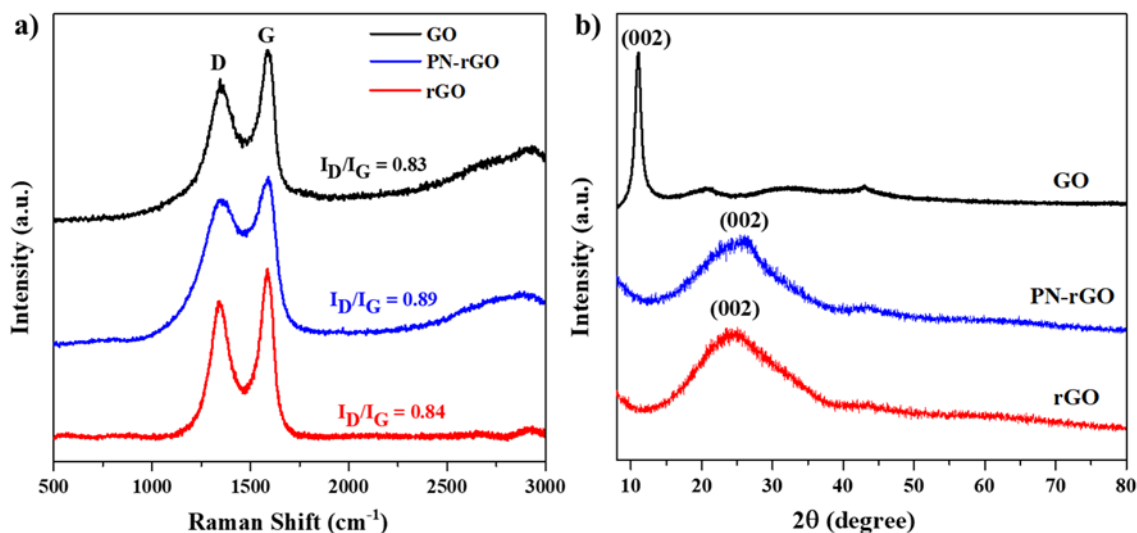
Figure 4.4   (a) X-ray diffraction (XRD) patterns, (b) Raman spectra of rGO, PN-rGO and GO

The Brunauer-Emmet-Teller (BET) surface area and pore structure play important roles in the electroactive materials used in supercapacitors. Figure 4 shows the nitrogen adsorption-desorption isotherms and the corresponding pore size distribution curves of rGOand PN-rGO samples. The nitrogen adsorption-desorption curves of PN-rGO sample (figure 4.5a) is type IV (Brunauer-Deming-Deming-Teller: BDDT) classification) with apparent hysteresis loops, indicating the presence of mesopores, which is consistent with the above TEM analysis (Zhang, Sun et al. 2019, Wan, Xiao et al. 2020).

In contrast, no hysteresis loops are observed on the isotherm curve of rGO, revealing the absence of pores on the GO surface. The BET surface area, pore size and pore volume of rGO and PN-rGOare summarized in table 4.1. Based on the BET method, the surface area of PN-rGO is 343.5 $m^2 \cdot g^{-1}$, which is larger than rGO (23.7 $m^2 \cdot g^{-1}$).

This is because the gases released from the decomposition of HCCP and *p*-PDA expand graphene sheets, while rGO suffers from restacking, in accordance with the SEM and TEM images (Gadipelli and Guo 2015). Figure 4.5b also shows the pore size distributions of the samples based on the Barret-Joyner-Halenda (BJH) method. The PN-rGO sample exhibits sharp peaks ranging from 2 to10 nm, suggesting the existence of dominant mesopores. The high surface area and large pore volume of PN-rGO can facilitate the transport of electrolyte ions and enhance energy-storage capacity (Sun, Xue et al. 2020).
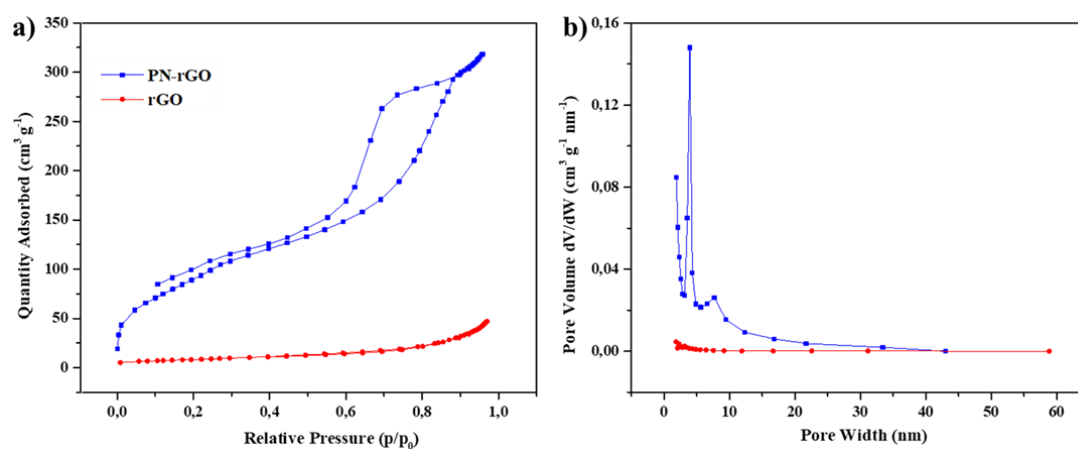
Figure 4.5   (a) Nitrogen adsorption-desorption isotherms and (b) corresponding pore size distribution curve of rGO and PN-rGO

Tableau 4.1   BET surface area and pore structure characterization of rGO and PN-rGO

Samples	S_{BET} (m^2.g^{-1})	Pore Volume (cm^3.g^{-1})	Average Pore Size (nm)
rGO	23.7	0.06	2.6
PN-rGO	343.5	0.7	4.5

To investigate the electrochemical supercapacitor performance of the as-synthesized materials PN-rGO and rGO, cyclic voltammetry (CV) and galvanostatic charge/discharge (GCD) measurement were evaluated by a three-electrode system in 6.0 M KOH electrolyte. Figure 4.6a shows the CV curves of PN-rGO and rGO at a scan rate 50 mV s^{-1} within the potential window of -1 V to 0 V. It can be observed that the CV curves of the two samples are quasi-rectangular, which are typical for electrochemical double-layer capacitors (EDLC) (Bai, Rakhi et al. 2013). It is clear that the CV curves area of PN-rGO is biggest, corresponding to higher specific capacitance (Cheng, Yi et al. 2019). This is because of the pseudocapacitive contribution mainly offered by P and N elements (Liu, Zhang et al. 2018). Figure 4.6b displays the GCD curves of PN-rGO and rGO measured at a current density 0.5 A g^{-1}.

The curves exhibit a quasi-triangular shape, indicating good electrochemical reversibility (Liu, Chang et al. 2019). Moreover, the longest charging / discharging time is clearly obtained for PN-rGO compared to rGO, implying higher capacitance, which in agreement with the CV results.
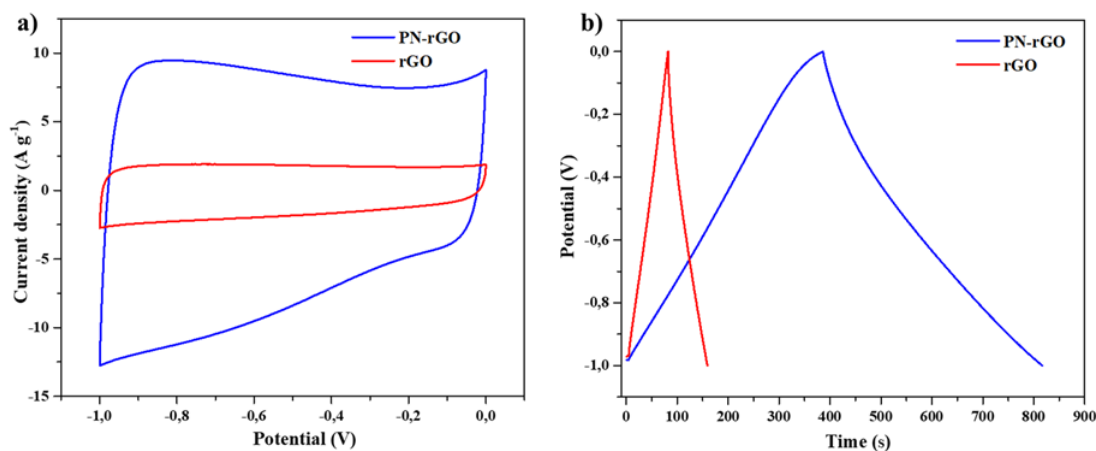
Figure 4.6 (a) CV curves of rGO and PN-rGO samples at 50 mV s^{-1} and (b) GCD curves of rGO and PN-rGO at 0.5 A g^{-1}

The CV measurements of PN-rGO at different scan rates from 5 to 100 mV s^{-1} are revealed in figure 4.7a. As the scan rate increases from 5 to 100 mV s^{-1}, the CV curves still remain a quasi-rectangular shape, indicating ideal capacitive properties (Qi, Xia et al. 2017, Lei, Li et al. 2018, Wan, Xiao et al. 2020). Additionally, the GCD curves for PN-rGO show highly symmetrical triangular shape at current densities from 0.5 to 20 A g^{-1} (figure 4.7b), which implied that the material has good charge/discharge reversibility and cycle performance (Zheng, Tang et al. 2020). The specific capacitance was calculated at different current densities From the GCD curves according to Eq. (1).

The specific capacitance of PN-rGO (figure 4.7c) was significantly larger than that of the rGO (figure S2) at all measured current densities (0.5 to 20 A g^{-1}). In addition, the capacitance retention for PN-rGO was 70% in the range 0.5 to 20 A g^{-1}, which indicate a good rate capability (Yang, Liu et al. 2019). The specific capacitance values obtained for PN-rGO (292 F g^{-1} at 0.5 A g^{-1}) is better than those reported by Ziyin (178 F g^{-1} at 0.5 A g^{-1}) (Lin, Liu et al. 2011), by Kaisheng et al. (202 F g^{-1} at 0.25 A g^{-1}) (Xia, Huang

et al. 2017), by Zhi et al. (227 F g^{-1} at 1 A g^{-1}) (Yang, Liu et al. 2019), and by Yaocai et al. (225 F g^{-1} at 1 A g^{-1}) (Bai, Rakhi et al. 2013). Moreover, the cycling stability of PN-rGO was investigated through 10000 charge/discharge cycles at current density of 10 A g^{-1} (figure 4.7d). The retention ratio of the capacitance value is 97% after 10000 cycles, suggesting higher stability and excellent cycle performance. These results confirm the excellent synergistic effect of heteroatom doping in the graphene nanosheets.
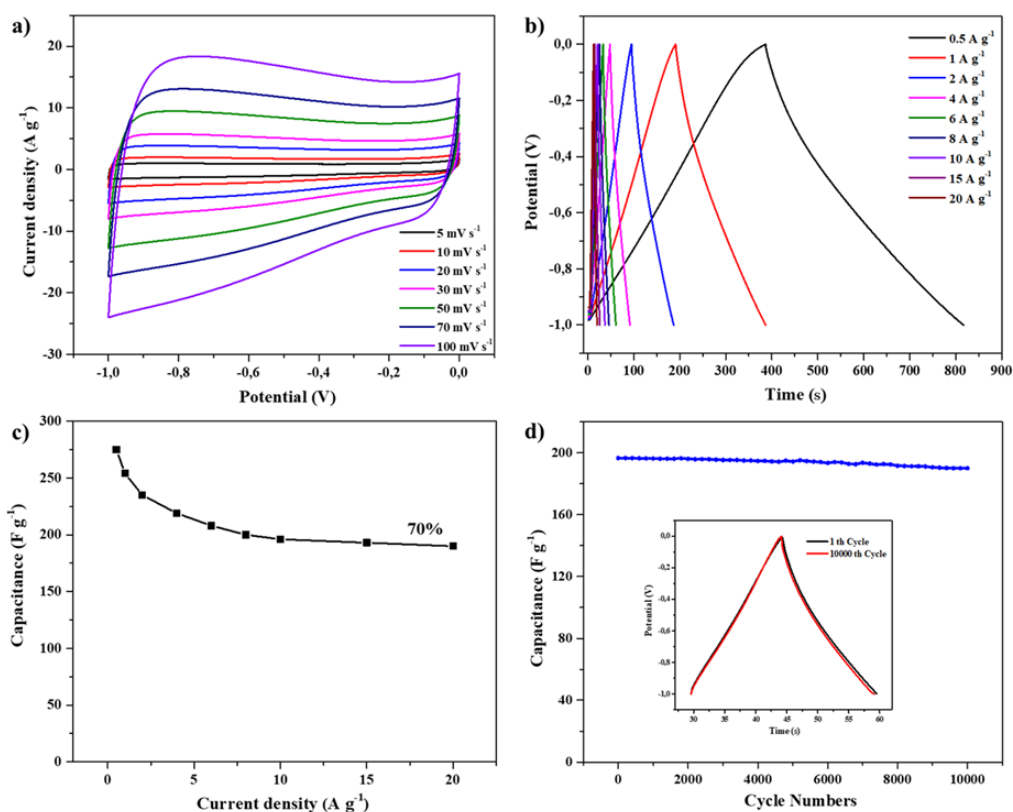
Figure 4.7   (a) CV curves of the PN-rGO electrode in 6 M KOH aqueous solution at different scan rates, (b) GCD curves of the PN-rGO electrode at different current densities, (c) A plot of the specific capacitances calculated from the discharge curves versus current density, (d) Cycling stability of the PN-rGO at a current density of 10 A g^{-1}, and the inset showing first and last cycles of GCD curves

Electrochemical impedance spectroscopy (EIS) provides information on the accessibility of electrolyte ions through materials. According to the Nyquist plots (figure 4.8), two regions can be clearly observed, including a semicircle in the high frequency region and a vertical-like slope in the low-frequency region. The nearly vertical line of PN-rGO in the low-frequency indicates the ideal capacitor behavior (Eftekhari 2018). In the high-frequency region, the semicircle corresponds to the charge-transfer resistance at the electrode/electrolyte interface (Xu, Cai et al. 2011). Obviously, PN-rGO has a small semicircle, indicating a small resistance to charge transfer, which is consequently related to its high electrical conductivity.
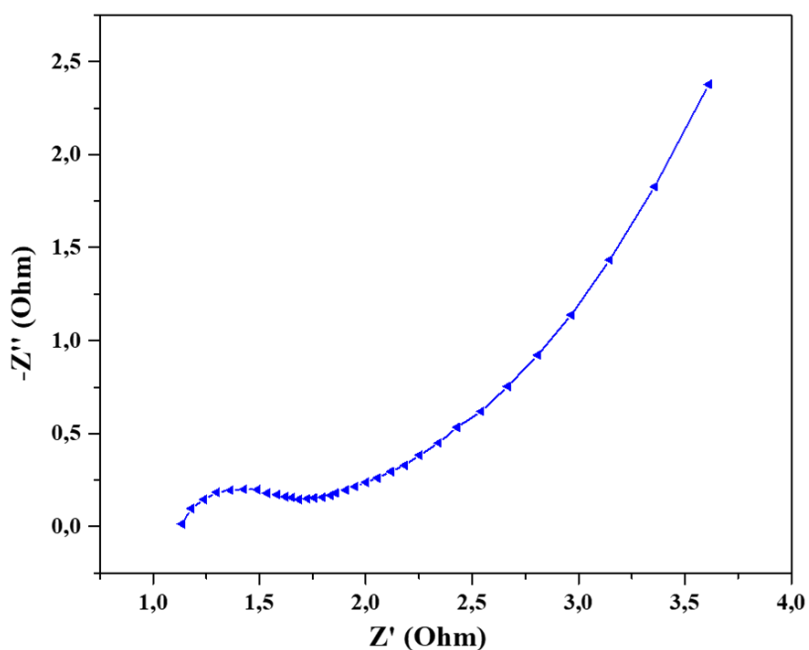
Figure 4.8   Nyquist plots of PN-rGO over the frequency range from 0.01 Hz to 100 kHz

To investigate the potential for practical applications of the PN-rGO based electrodes, a symmetric supercapacitor device was assembled and tested in 6 M KOH aqueous solution under a potential range of 0 to 0.6 V. The electrochemical performance of the device based on two PN-rGO pieces, as positive and negative electrodes was measured using CV and GCD. The performance of the device was evaluated from the obtained specific capacitance, energy density and power density, as shown in figure 4.9. The schematic illustration of the assembled symmetric supercapacitor is shown in figure 4 8a. The CV curves of the symmetric supercapacitor under various scan rates from 10 to 100 mV s^{-1} are presented in figure 4.9b. The area under the CV curve shows an approximately rectangular shape were sustained even at a high scan rate of 100 mV s^{-1}, suggesting a significant EDLC behaviour and ideal capacitive performance.

Figure 4.9c displays the GCD curves of the symmetric supercapacitor measured at various current densities from 0.5 to 10 A g$^{-1,}$ exhibiting an almost symmetrical triangle form, which further reveals high reversibility of capacitive behaviour, as consistent with the CV results. Besides, the Ragone plot in figure 4.9d illustrates the performance of the symmetric supercapacitor in terms of power density and energy density and was calculated from the discharge curves using the equations (3) and (4). The NP-rGO device delivered the energy density of 8.2 W h kg^{-1} at a power density of 570 W kg^{-1} under 0.5 A g^{-1}, and retained the energy density of 3.5 W h kg^{-1} at 6000 W kg^{-1}, which is comparable to those previously reported carbon materials (Chen, Wu et al. 2016, Xia, Huang et al. 2017, Xue, Zhu et al. 2019, Shen, Mo et al. 2020).

In addition, it has been observed that the symmetrical supercapacitor shows excellent electrochemical stability with 85% retention of the initial capacitance after 10000 repeated cycles at 6 A g^{-1} (figure 4.9e).
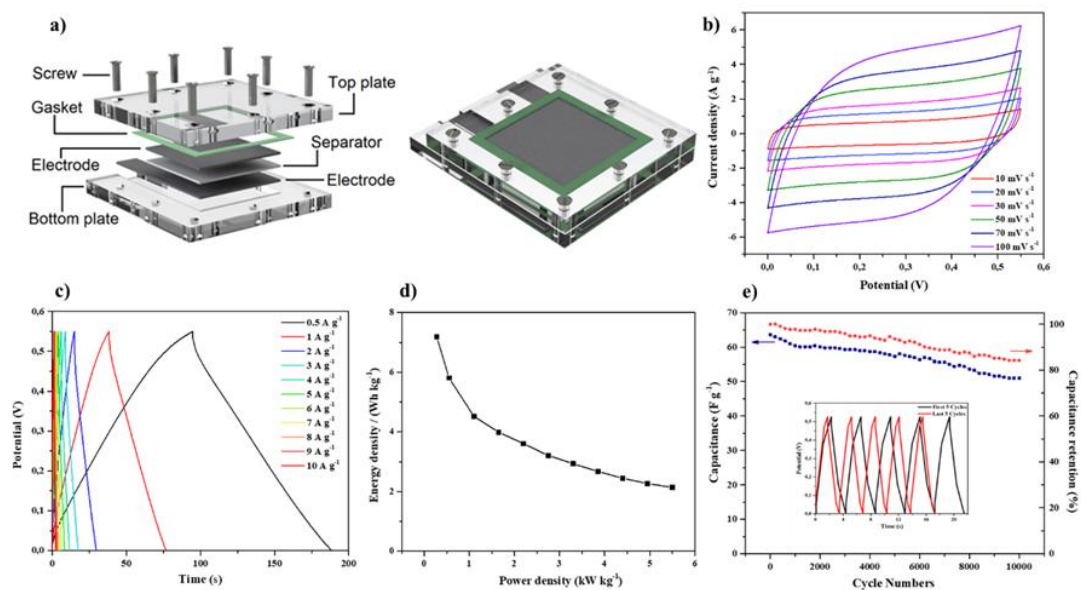
Figure 4.9　　　(a) The schematic illustration of the assembled symmetric supercapacitor, (b) CV curves of the symmetric supercapacitor measured at different scan rates under a potential range of 0-0.6 V in 6 M KOH electrolyte, (c) GCD curves of the symmetric supercapacitor at different current densities, (d) Ragone plot of the PN-rGO device and (e) Specific capacitance of PN-rGO under variable current densities

4.6   Conclusion

In summary, we have successfully prepared PN-rGO as electrodes for supercapacitors by direct pyrolysis of the functionalized graphene oxide (FGO). The PN-rGO exhibits high specific capacitance of 292 F g^{-1} at 0.5 A g^{-1}, a good rate performance (retention of 70% from 1 to 20 A g^{-1}) and excellent cycling stability (97% retention of the initial specific capacitance after 10,000 consecutive charge-discharge cycles at 20 A g^{-1}). The assembled symmetric supercapacitor exhibits an energy density of 8.2 W h kg^{-1} at a power density of 570 W kg^{-1}. The incorporation of heteroatoms N, P into carbon materials could effectively modify and improve their electrochemical performances.

CHAPITRE V

NITROGEN/PHOSPHORUS CO-DOPED POROUS CARBON AS AN EFFICIENT ELECTRODE MATERIAL FOR SUPERCAPACITORS

Khaled Rhili[a], Siham Chergui[a], Ahmad Samih ElDouhaibi[b] and Mohamed Siaj[a]*

[a] Department of Chemistry, University of Quebec at Montreal, Montreal QC, H3C3P8, Canada

[b] Department of Chemistry, Lebanese University, College of Science III, Campus Mont Michel, 1352, Tripoli, Lebanon

*Corresponding author at: Email: siaj.mohamed@uqam.ca

Contribution des auteurs

KHALED RHILI

L'auteure principale a effectué toutes les manipulations expérimentales incluant la synthèse de produit ainsi que les caractérisations, la recherche bibliographique et les traitements des résultats. Aussi, elle a écrit la première version du manuscrit et a contribué à la version finale du manuscrit.

SIHAM CHERGUI

Le co-auteur a effectué des analyses et a participé à l'interprétation des résultats et la rédaction du manuscrit.

Ahmad Samih El Douhaibib

Le co-auteur a participé à l'interprétation des résultats et la rédaction du manuscrit.

MOHAMED SIAJ

L'auteur de correspondance a effectué la supervision des travaux et il a participé à l'interprétation des résultats, à l'écriture ainsi qu'à la révision finale du manuscrit.

Journal of Colloid and Interface Science, soumis (2023).

5.1   Résumé

Des matériaux carbonés poreux dopés aux hétéroatomes d'azote (N) et de phosphore (P) ont été préparés par carbonisation des cyclomatrix polyphosphazènes, synthétisés par polymérisation entre l'hexachlorocyclotriphosphazène (HCCP) et la p- phénylènediamine (p-PDA) (ou Tris (4 aminophényl) amine), suivie d'une activation avec K_2CO_3. Les échantillons obtenus NPC1 et NPC2 présentent une structure poreuse qui fournissent des canaux pour le transport et le stockage des électrons et des ions. Les matériaux synthétisés ont été évalués en tant que matériaux de supercondensateur. L'électrode NPC2 affiche une capacité spécifique élevée de 483 F g^{-1} à 0,5 A g^{-1}, révélant une excellente performance électrochimique. La rétention de cyclage montre une excellente stabilité de 98% après 10 000 cycles de charge-décharge consécutifs à 20 A g^{-1}. De plus, un supercondensateur symétrique a été assemblé en utilisant le NPC2 présente une densité d'énergie relativement élevée de 13,2 Whkg^{-1} à une densité de puissance de 700 Wkg^{-1}. Le supercondensateur obtenu par une méthode de synthèse facile présente une haute performance.

5.2   Abstract

Nitrogen and phosphorus heteroatoms-doped carbon materials were prepared by carbonization of cyclomatrix polyphosphazenes, which is synthesized by a simple polymerization technique between hexachlorocyclotriphosphazene and *p*-phenylenediamine (or Tris(4-aminophenyl) amine), followed by activation with K_2CO_3 as an activator. The obtained samples Nitrogen-Phosphorus co-doped porous carbon materials denoted NPC1 and NPC2 have a hierarchical porous structure, which provides channels for the transport and storage of electrons and ions. As an electrode material for supercapacitors, the specific capacitance of the NPC2 displays a high specific capacitance of 483 F g^{-1} at 0.5 A g^{-1}, revealing superior rate performance. The capacity retention after 10,000 consecutive charge-discharge cycles at 20 A g^{-1} is 98%, demonstrating excellent cycling stability. Moreover, the assembled symmetric supercapacitor using NPC2 exhibits a relatively high energy density of 13.2 W h kg^{-1} at a power density of 700 W kg^{-1}. Thus, a promising electrode material for high-performance supercapacitors is obtained through a facile synthesis route.

Keywords: Cyclomatrix, porous carbon, supercapacitor, Nitrogen/ Phosphorus co-doped.

5.3   Introduction

Supercapacitors have attracted considerable interest and increased attention in recent years due to their higher power density than batteries and higher energy density than conventional dielectric capacitors (Wang and Kaskel 2012, Shen, Ran et al. 2015, Raza, Ali et al. 2018). The charge storage mechanisms of supercapacitors generally can be divided into two classes, electrical double-layer capacitor (EDLC) and pseudocapacitor (Wang and Xia 2013). EDLCs require electrode materials with a high specific surface area and appropriate pore size (Zhang and Zhao 2009). Design and synthesis of supercapacitors have particularly involved activated carbon to improve charge induction on the electrode surface (Wang, Fang et al. 2016, Gao, Fu et al. 2018, Shen, Mo et al. 2020, Zeng, Miao et al. 2021).

Activated carbons, though are easy and relatively cheap to prepare, exhibit low energy densities despite their large surface areas. Studies towards improving electrochemical characteristics of activated carbons have continued and are well documented in the literature (Sevilla and Mokaya 2014). Generally, various activating agents, such as K_2CO_3, CO_2, NaOH, $CaCl_2$, $ZnCl_2$, KOH and H_3PO_4 (Tian, Gao et al. 2016, Wang, Li et al. 2017, Lin, Ma et al. 2018). Weng et al. prepared an activated carbon material from a carton box activated by eutectic KOH, NaOH melt, the material showed very good performance in supercapacitor applications, exhibiting high surface area of 2731 m g^{-1} and rate capability up to 75 A g^{-1} in symmetric supercapacitor devices (Wang, Fang et al. 2016).

Recently, the most researched modification method is to dope heteroatoms in the carbon material, so that the surface of the carbon material will exhibit more active sites, which leads to improving its electrochemical performance (Wei, Zhou et al. 2013, Tang, Salunkhe et al. 2016, Wang, Wang et al. 2019). The most common elements used to dope carbon materials are nitrogen (N), sulfur (S), boron (B), oxygen (O) and phosphorus (Kim, Yang et al. 2011, Liu, Liu et al. 2017, Qi, Xia et al. 2017). Among

them, the N atom has an atomic radius like the C atom, which enables it to easily replace the C atom in the carbon-based material. The electrical conductivity, chemical reactivity, and surface wettability for a carbon-based electrode can be modified greatly when it doped by N atoms. These chemical modifications are necessary for the electrochemical energy storage (Wang, Sun et al. 2014). It's worth noting that co-doping could further enhance the electrochemical performances of single-heteroatom-doped carbon materials. The enhanced performances of co-doped carbon materials are generally assigned to the synergistic effect of multiple heteroatoms doping (Liu, Liu et al. 2017, Qi, Xia et al. 2017, Xia, Huang et al. 2017).

There are serval methods for preparing heteroatoms doped carbon materials: in-situ doping (Ren, Li et al. 2018) and direct pyrolysis (Song, Yang et al. 2016). The commonly used nitrogen-rich precursors are biomass (Zhong, Gong et al. 2015), polymers (Hu, Zhu et al. 2018) and small nitrogen-containing molecules(Barzegar, Bello et al. 2015).

Polyphosphazenes is a class of polymeric materials in which alternate phosphorus and nitrogen atoms are arranged to form a backbone, provide the promising candidates for formation of N, P co-doped carbon as electrodes materials (Allcock 2006, Chen, Huang et al. 2016). Most of polyphosphazenes polymers were prepared from hexachlorotricyclophospazene (HCCP) as a monomer, linked to various organic nucleophiles bearing O, N, and S as nucleophilic sites (Rhili, Chergui et al. 2021). Their relative porosity and high surface area rendered them as good targets with various applications including but not limited to flame retardant materials, Iodine adsorbents, gas and energy storage materials, and metallic ions sorption agents. Among other applications, studies of supercapacitance properties of polyphosphazenes matrices have recently gained particular attention (Dasari, Yu et al. 2013, Zhou, Qiu et al. 2020).

In this work, a nitrogen/phosphorus co-doped porous carbon material was synthesized through the simple carbonization/activation process. Hexachlorocyclotriphosphazene

and *p*-phenylenediamine (or Tris(4-aminophenyl) amine) were chosen to prepare cyclomatrix polyphosphazenes by a polymerization reaction. These polyphosphazenes contain a considerable amount of carbon, nitrogen, and phosphorus at the same time. The morphology, composition and structure of the carbon materials were investigated by SEM, TEM, XRD, BET, XPS, etc. The capacitive performance of the obtained samples of nitrogen/phosphorus co-doped porous carbon material is analyzed in detail.

5.4   Experimental methods

5.4.1   Materials

Hexachlorocyclotriphosphazene (HCCP), *p*-Phenylenediamine (*p*-PDA), Tris(4-aminophenyl) amine (TAPA), 1.4-Dioxane, ethanol, acetone, triethylamine (TEA) were supplied from Sigma-Aldrich (Oakville, ON, Canada). De-ionised (DI) water was produced by a water purification machine (Milli-Q® Reference). 1.4-Dioxane was dried by 4 Å molecular sieves before being used.

5.4.2   synthesis of Cyclomatrix polyphosphazenes (C-POPs1 and C-POPs2)

The synthesis procedure is shown in figure 5.1. Typically, *p*-PDA (1.5 mmol) (or 1.0 mmol TAPA) and 1.0 mmol HCCP were dissolved in 20 mL dioxane to form grayish suspension, after which 1.74 mL of TEA was added. The suspension was transferred to an 80 mL Teflon-lined stainless-steel autoclave and maintained at 200 ^{o}C for 24h. After the reaction mixture was left to cool to room temperature, the powders were filtered off and washed several times with deionized water, EtOH, and acetone sequentially until the filtrate was neutral and colorless. Then, the powders were dried overnight in a vacuum oven at 80 °C. The resulting materials were denoted as C-POPs1 and C-POPs2.
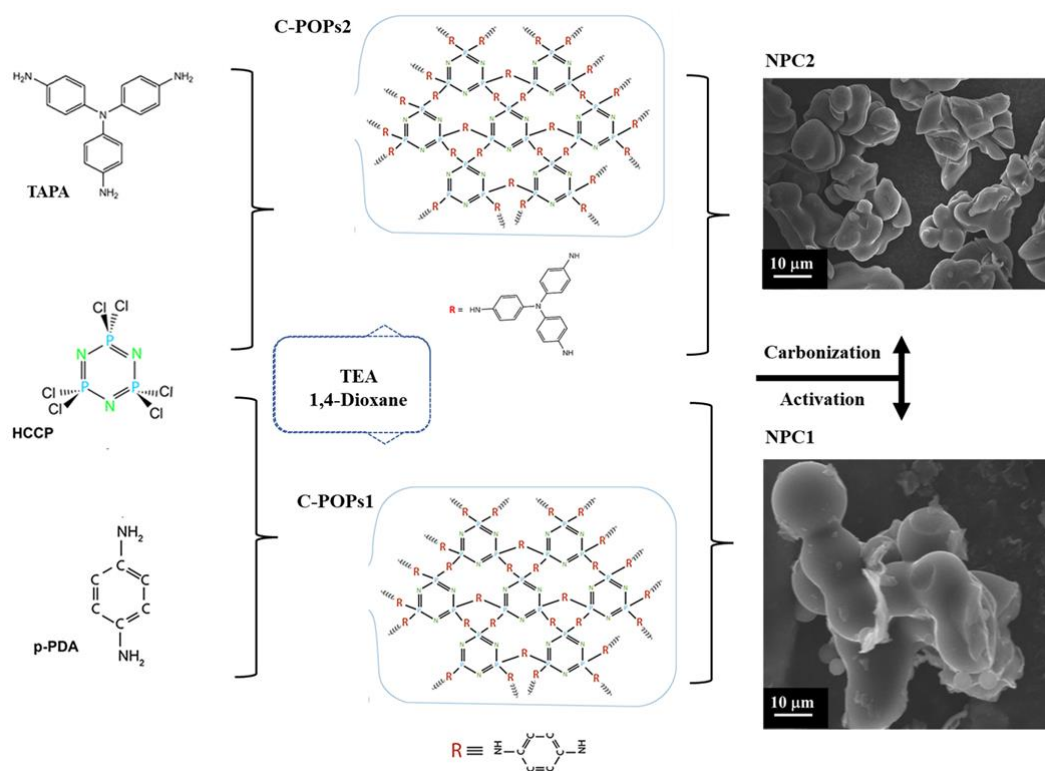
Figure 5.1   Synthetic route of the nitrogen and phosphorus co-doped carbon materials

5.4.3   Nitrogen-phosphorus co-doped porous carbon materials NPC1 and NPC2

The prepared materials C-POPs were physically mixed with K_2CO_3 as chemical activator (C-POPs and K_2CO_3 in a mass ratio of 1:3), and the mixture was carbonized under N_2 atmosphere at 800 °C for 2 h with a heating rate of 5 °C/min and then cooled to room temperature. Finally, the obtained samples were washed with 1 M HCl solution followed by deionized water and ethanol for several times until neutral pH was obtained, and the products were dried at 80 °C under vacuum for 24 h to yield the NPCx (x=1,2) samples.

5.4.4   Characterization Methods

The X-ray diffraction (XRD) was performed using a diffractometer (Bruker D8 Advance) with Cu-Kα radiation ($\lambda = 1.54182$ Å) in an angular interval from 20° to 100° at room temperature. X-ray photoelectron spectroscopy (XPS) data for elemental composition and valence information was collected with XPS PHI 5600-ci (Physical Electronics, Eden Prairie, MN, USA). The morphology of materials was obtained with a scanning electron microscope (SEM) by utilizing a JEOL (JSM7600F) operated at 10 kV accelerating voltage and a working distance of 14 mm using secondary electron imaging mode. Transmission electron microscopy (TEM) and Energy-dispersive X-ray spectroscopy (EDS) was performed on a Joel JEM-2100F. Raman measurements were acquired on a Renishaw in Via microspectrometer using a 50X objective and a 514 nm laser wavelength.

5.4.5   Preparation of electrodes and electrochemical measurements

Electrochemical measurements, including cyclic voltammetry (CV), galvanostatic charge–discharge (GCD) and electrochemical impedance spectroscopy (EIS), were

performed on a Biologic SP-200 potentiostat (Pine Research Instrumentation, Durham, NC, USA), controlled by EC-Lab software in a conventional three-electrode system with 6 M KOH aqueous solution as the electrolyte. The modified glassy carbon electrodes (GC, S = 0.1256 cm^2) was used as the working electrodes. The Ag/AgCl electrode and the platinum wire were employed as a reference electrode and counter electrode, respectively.

The working electrode was prepared by mixing the as prepared materials NPC with 10 μL of Nafion™ solution (5 wt %), dispersing into 1 mL water-ethanol solution with a volume ratio of 4:1 by at least 30 min sonication to form a homogeneous ink. Then 18 μL of the resulting suspension was dropped onto the carbon-working electrode and dried in the air at room temperature. The CV curves were obtained at the scan rates ranging from 5 to 100 mV s^{-1} with the voltage ranging from -1 V to 0 V. The GCD curves were obtained at the current density ranging from 0.5 to 20 A g^{-1}. The (EIS) tests were measured in the frequency range from 0.01 Hz to 100 kHz. The symmetric supercapacitor device was fabricated by using the NPC as both the positive and negative electrodes and graphite layer acted as a collector. Filter paper was used as separator and 6 M KOH acted as electrolyte, respectively. The total mass loading of NPC of positive and negative electrodes were 2 mg.

The specific capacitance (F g^{-1}) was determined from GCD curves according to Eq. (1)

$$C = \frac{I * \Delta t}{m * \Delta V} \tag{1}$$

where 'I' is the charge-discharge current (A); Δt is the discharge time (s); ΔV is the potential window (V); and m is the active material loading in the working electrode (g).

The energy (E, W h kg^{-1}) and power (P, Wkg^{-1}) densities were calculated from charge–discharge measurement using Eq. (2) and Eq. (3) respectively.

$$E = \frac{1}{2}C(\Delta V)^2 \tag{2}$$

where 'C' is the specific capacitance; 'ΔV' is the voltage window of the assembled device.

$$P = \frac{E}{\Delta t} \tag{3}$$

where 'Δt' is the discharge time.

5.5   Results and Discussion

The as-prepared C-POPs1 and C-POPs2, were characterized with FTIR, Solid-state Nuclear Magnetic Resonance (ssNMR). The FTIR spectra of the monomers and the products are displayed in figure 5.2. The absorption peaks of 3360 cm^{-1} and 1622 cm^{-1} were ascribed to the stretching vibration of N-H and C=C groups in p-PDA (Zhang, Zhao et al. 2016). The characteristic peaks at 1156 cm^{-1} and 870 cm^{-1} were assigned to the stretching vibration of P=N and P-N groups in HCCP, respectively, and the peak of 650 cm^{-1} was attributed to P-Cl groups (Rhili, Chergui et al. 2021). The absorption peaks of TAPA at 3335, 1602, and 1500 cm^{-1} were attributed to the N-H stretching vibration, C=C stretching vibration and the C-C bending vibration of aromatic ring, respectively (Zhao, Jiang et al. 2021). In the curves of C-POPs1 and C-POPs2, the absorption peaks were very close to the corresponding positions of p-PDA, HCCP or TAPP, which meant that the nitrogen and phosphorus co-doped material was synthesized successfully. In addition, the peaks at 914 and 924 cm^{-1} are assigned to the stretching vibration of P-NH-Ph (Rhili, Chergui et al. 2021).
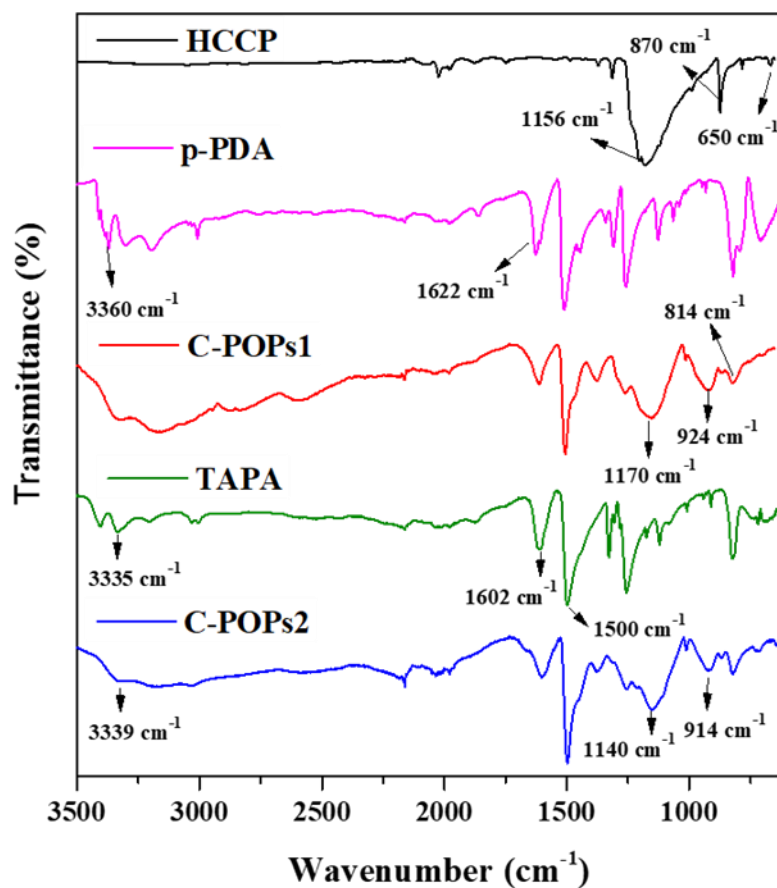
Figure 5.2   FTIR spectra of HCCP, *p*-PDA, TAPA, C-POPs1, and C-POPs2

Cross-Polarization Magic-Angle-Spinning NMR spectroscopy (CP/MAS NMR) for ^{13}C and ^{31}P was performed to characterize the molecular structures. The ^{13}C CP/MAS NMR spectrum of C-POPs 1 showed clearly only two single peaks in the aromatic region at 118 ppm and 134 ppm corresponding to the carbons (C=C) and (=C-N-P) respectively (figure 5.3a). However, there are three main peaks in the spectra of C-POPs 2

The peaks located at 118 and 129 ppm, with different chemical environments can be assigned to the signal of the carbons of (C-H) in benzene ring. The peak at around 141 ppm can be attributed to the carbons (=C-N-P) and (=C-N-C). These results confirm that all (NH$_2$) groups of p-PDA and TAPA have reacted with HCCP. The solid-state ^{31}P NMR spectra (figure 5.3b) exhibit a single sharp peak appears at 2.8 and 6.2 ppm corresponding to the phosphorus of P−N bonds in C-POPs 1 and C-POPs 2, respectively, indicating one phosphorous chemical environment and a complete substitution reaction of all the Cl atoms by *p*-PDA and TAPA (Wan and Huang 2017).
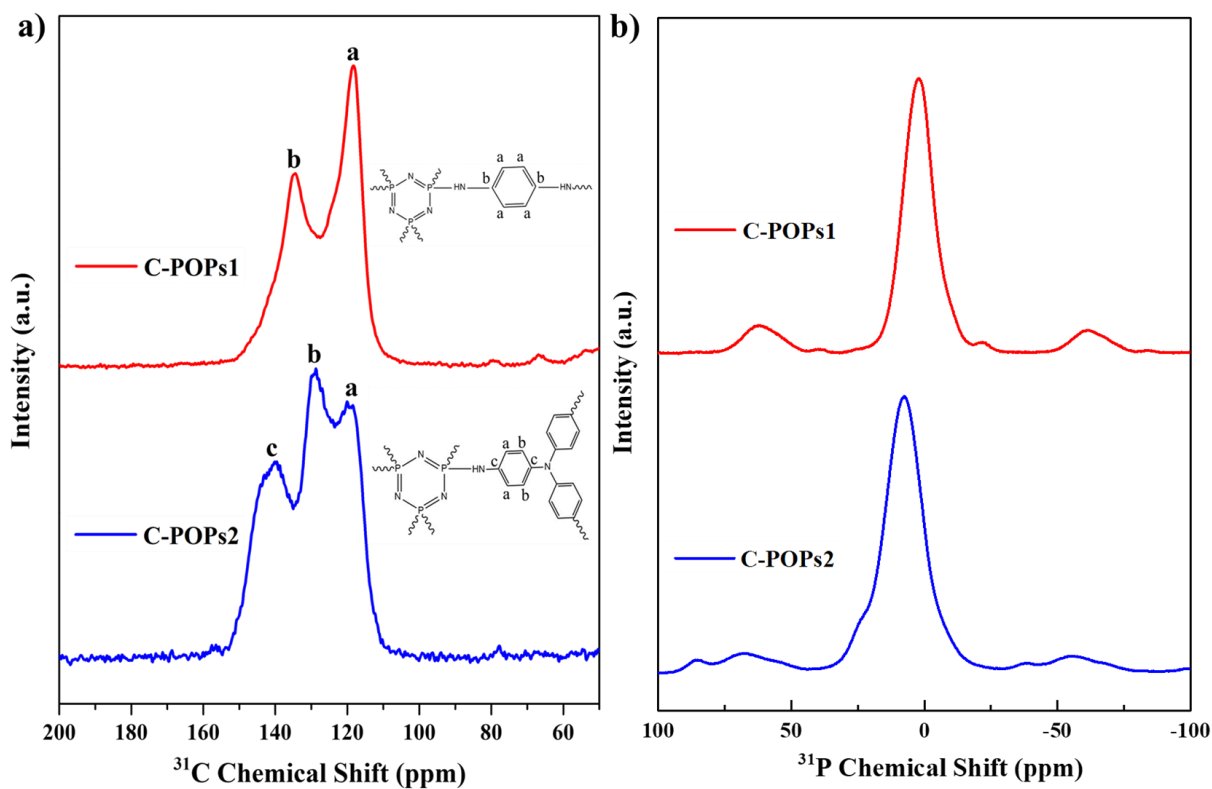
Figure 5.3   Solid‑state (a) ^{13}C and (b) ^{31}P CP/MAS NMR spectrum of POPs1 and POPs2

The morphology of the as synthesized NPC1 and NPC2 products were investigated by scanning electron microscopy (SEM) and transmission electron microscopy (TEM) (figure 5.3). It can be observed that NPC1 exhibits spherical morphology with some cracked ends (figure 5.4a). Whereas NPC2 displayed a clusters morphology (figure 5.3b). TEM and HR-TEM (figure 5.3 c-f) results show a highly mesoporous structure of NPC1 and NPC2. This morphology with the pore structure can increase the specific surface area and their capacitance of storing electrons and ions, which provide more active sites to obtain a higher specific capacitance (Zou, Zhang et al. 2020, Zeng, Miao et al. 2021).

In addition, the elemental mapping (see appendix D, figure D1) confirms the existence of C, N, O, and P, indicating the successful N, P co-doping into the carbon materials.
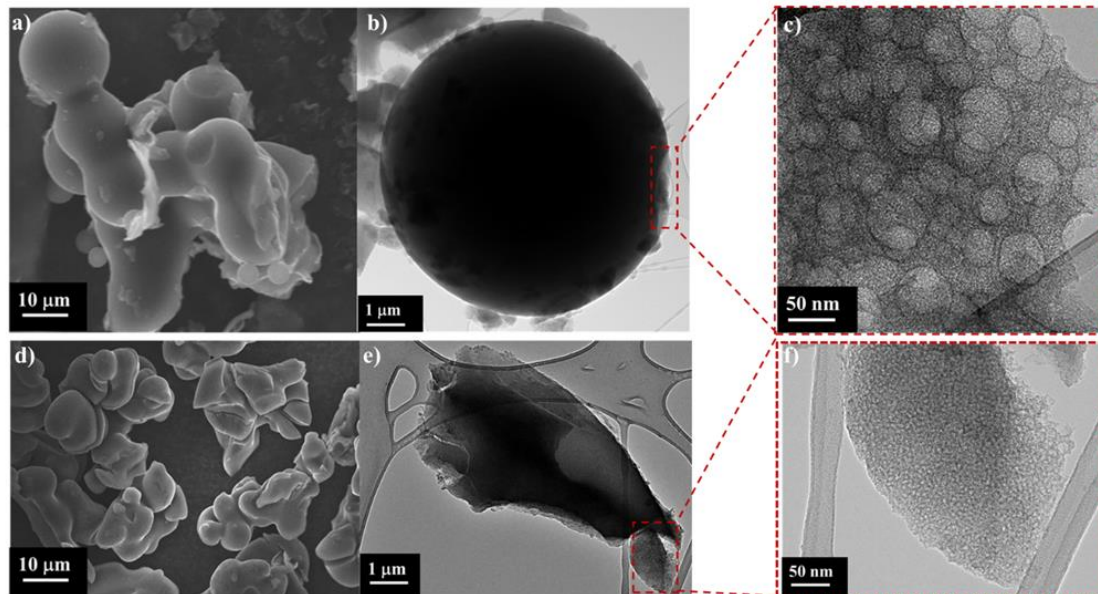
Figure 5.4   SEM images of (a) NPC1, (d) NPC2, TEM and HRTEM images of (b, c) NPC1 and (e, f) NPC2

The phase structure of the carbon samples was tested by using power X-ray diffraction (XRD) patterns, as shown in Figure 5.5a. The NPCx (x = 1,2) samples show two broad diffraction peaks at 2θ values of around 25° and 44°, corresponding to (0 0 2) and (1 0 0) planes of carbon materials, respectively (Liu, Liu et al. 2017). The appearance of broad peaks confirmed the amorphous structure of the carbon materials (Abbas, Basharat et al. 2020).The graphitization degrees for the carbon samples were studied by the Raman analysis.

As shown in figure 5.4b, the Raman spectra have two peaks located at around 1352 cm^{-1} and 1593 cm^{-1}, corresponding to the D-band peak and the G-band peak, respectively. The D band reflects the defects and disorder of carbon materials while the G band is associated with the bond stretching of the pair of sp2 carbon atoms (Lin, Ma et al. 2018, Rhili, Chergui et al. 2021). The intensity ratio (I_D/I_G) of the G band and D band reflects the graphitization degree of carbon materials (Chen, Liu et al. 2018, Wan, Xiao et al. 2020). The I_D/I_G values of NPC1 and NPC2 are 0.96 and 0.98, respectively, and their ratios are all less than 1, indicating that the C-POPs samples had a high degree of graphitization (Zeng, Miao et al. 2021). Moreover, the I_D/I_G value of NPC2 is higher than NPC1, indicating that more defective sites were created through the incorporation of heteroatoms into the carbon network (Li, Qin et al. 2019).
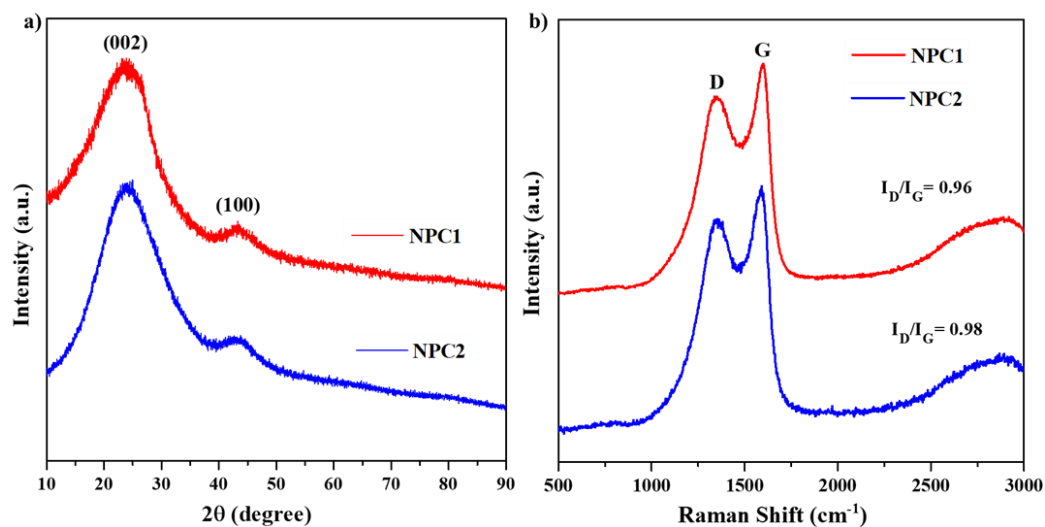
Figure 5.5   (a) XRD patterns and (b) and Raman spectra of NPC1 and NPC2

The pore structures of the obtained samples were studied by nitrogen adsorption/desorption isotherms and the results are shown in table D1 (see appendix D). Figure 5.6a displays the nitrogen adsorption-desorption isotherms of NPC1 and NPC2 samples. It can be seen that the adsorption-desorption isotherms of the samples could be a composition of type I and type IV according to the International Union of Pure and Applied Chemistry (IUPAC) classification, indicating the presence of micropores and mesopores (Carja, Serbezeanu et al. 2014, Zhang, Sun et al. 2019, Wan, Xiao et al. 2020). As can be seen from table D1, the surface areas (SSAs) calculated by the Brunauer-Emmett-Teller (BET) method and total pore volumes (V_{total}) of samples increased from 943.3 $m^{2.}$ g^{-1} to 1042.7 $m^2.$ g^{-1} and from 0.51 to 0.68 cm^3 g^{-1}, respectively. It could be explained that the C-POPs2 material has a higher graphitic structure due to its larger aromatic ring structure and higher carbon content.

On the other hand, during the carbonization process, the gases released from the decomposition of nitrogen and phosphorus expand carbon sheets, leading to an increase

in the specific surface area of carbon materials (Lotsch and Schnick 2007, Cheng, Yi et al. 2019). Figure 5.6b also shows the pore size distributions of the samples based on the Barret-Joyner-Halenda (BJH) method. The samples exhibited sharp peaks ranging from 2 to 10 nm and a distribution of pores in the range of 10-50 nm, which confirm the coexistence of mesopores and micropores characteristics in these samples. The electrode material with a high specific surface area can provide abundant electrochemical active sites and enhance the effective charge storage area between electrode and electrolyte, thus improving the performance of supercapacitor (Xu, Li et al. 2018, Li, Lv et al. 2021).
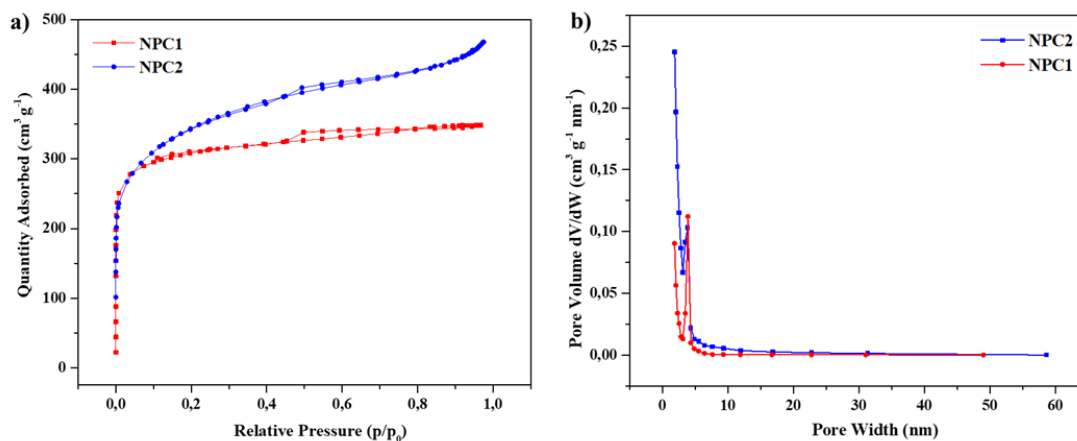
Figure 5.6   (a) N_2 adsorption-desorption isotherms, (b) pore size distribution of NPC1 and NPC2

To evaluate the electrochemical performance of produced samples as supercapacitor electrodes to reveal the functions of nitrogen and phosphorus functionalities, CV, EIS and galvanostatic charge/discharge (GCD) measurements were carried out in a three-electrode configuration using 6 M KOH. Figure 5.6a displays CV curves of NPC1 and NPC2 electrodes at a scan rate of 50 mV s^{-1} within the potential window of -1 V to 0 V. It can be observed that the CV profile of NPC2 shows typical rectangular-like shape compared with NPC1, which indicates that the electrode possesses both electrochemical double-layer capacitors (EDLC) and Faradaic pseudo-capacitance (Panja, Bhattacharjya et al. 2015, Gao, Fu et al. 2018, Zhang, Mo et al. 2019).

Moreover, the CV curve area of NPC2 is bigger, revealing that NPC2 possessed the relatively highest specific capacitance. The GCD curves of NPC1 and NPC2 measured at a current density 1 A g^{-1} are presented in figure 5.6b. The curves exhibit a quasi-triangular shape, indicating good electrochemical reversibility (Liu, Chang et al. 2019). Moreover, the longer charging/discharging time is clearly obtained for NPC2 compared to NPC1, implying higher capacitance behaviors, which in agreement with the CV results (figure 6.6a). The specific capacitance was calculated at different current densities (0.5 to 20 A g^{-1}) from the GCD curves (see Appendix D, figure D2b) for NPC1 and (figure 5.7b) for NPC2 according to Eq. (1). the specific capacitance of NPC2 can attain 483 F g^{-1} at 0.5 A g^{-1}, which is much higher than NPC1 (275 F g^{-1}).
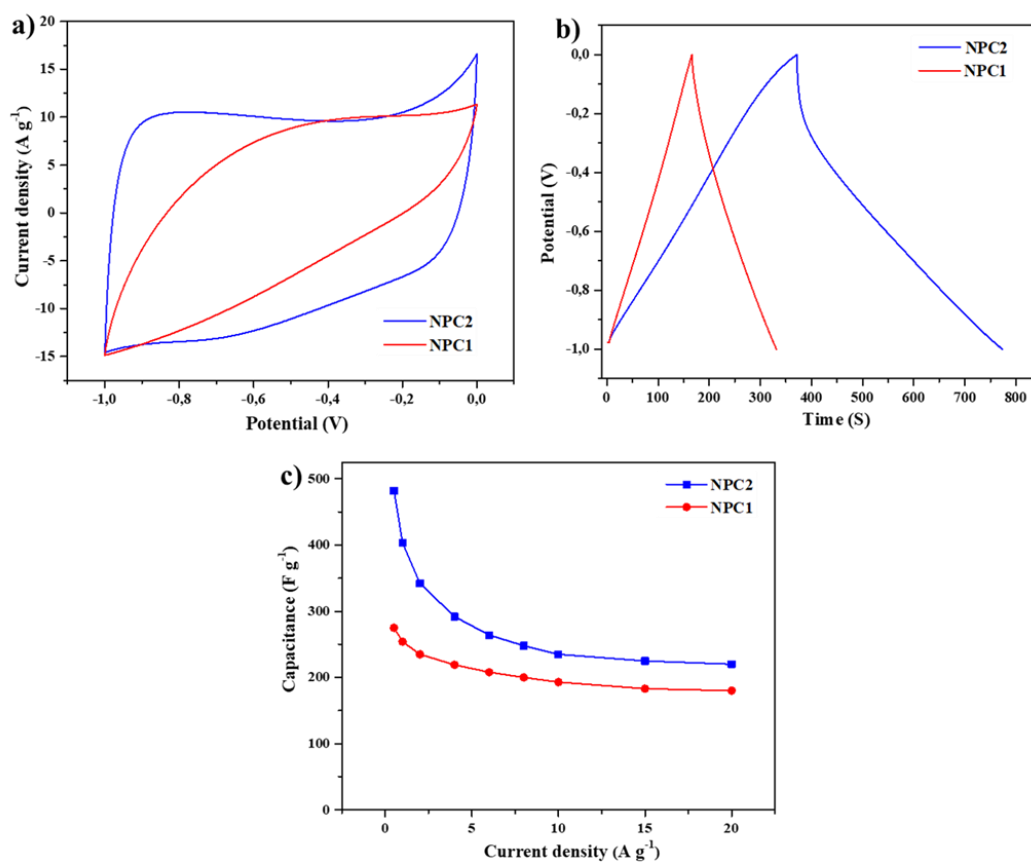
Figure 5.7   (a) CV curves at the scan rate of 50 mV s^{-1}, (b) GCD curves at the current density of 1 A g^{-1}, (c) the specific capacitance at various current densities in the range 0.5-20 A g^{-1} NPC1 and NPC2

Figure D.1a and figure 5.8a are the cyclic voltammograms of NPC1 and NPC2 respectively, at different scan rates ranging from 5 to 100 mV s^{-1}. The shape of the CV curve gradually changes from an irregular rice-grain shape for NPC1(Appendix D, figure D.1b) to a nearly symmetrical rectangular shape for NPC2, indicating that charge and ion transfer are effectively improved through the elevation of the graphitic structure (Barzegar, Bello et al. 2015, Chaudhary, Nayak et al. 2018). This is due to the enhancement of conductivity, and enlarged microporous and mesoporous surface area (Zeng, Miao et al. 2021).

The GCD curve (figure 5.8b) presents the shape of a nearly symmetrical triangle, and its current density ranges from 0.5 to 20 A g^{-1}, representing highly reversible charge-discharge behavior. The effect of pore structure and the ion diffusion/electron on the performance of the electrode NPC2 was investigated by electrochemical impedance spectroscopy (EIS). The imaginary part of the impedance tends to zero, and a semicircle with small diameter is displayed at high frequencies in figure 5.8c, whereas at low frequencies it increased sharply, thus approaching the variation of impedance.

The EIS results show that the electrode had a good electron transfer process and indicated satisfactory capacitive behavior (Kouchachvili, Yaïci et al. 2018, Momodu, Sylla et al. 2019, Sun, Xue et al. 2020). Besides, the cycling stability of the NPC2 has been resulted to 98% of the initial specific capacitance after 10000 charge/discharge cycles at current density of 10 A g^{-1} (figure 5.8d), suggesting higher stability and excellent cycle performance. These results confirm the excellent synergistic effect of heteroatom doping in the carbon materials.
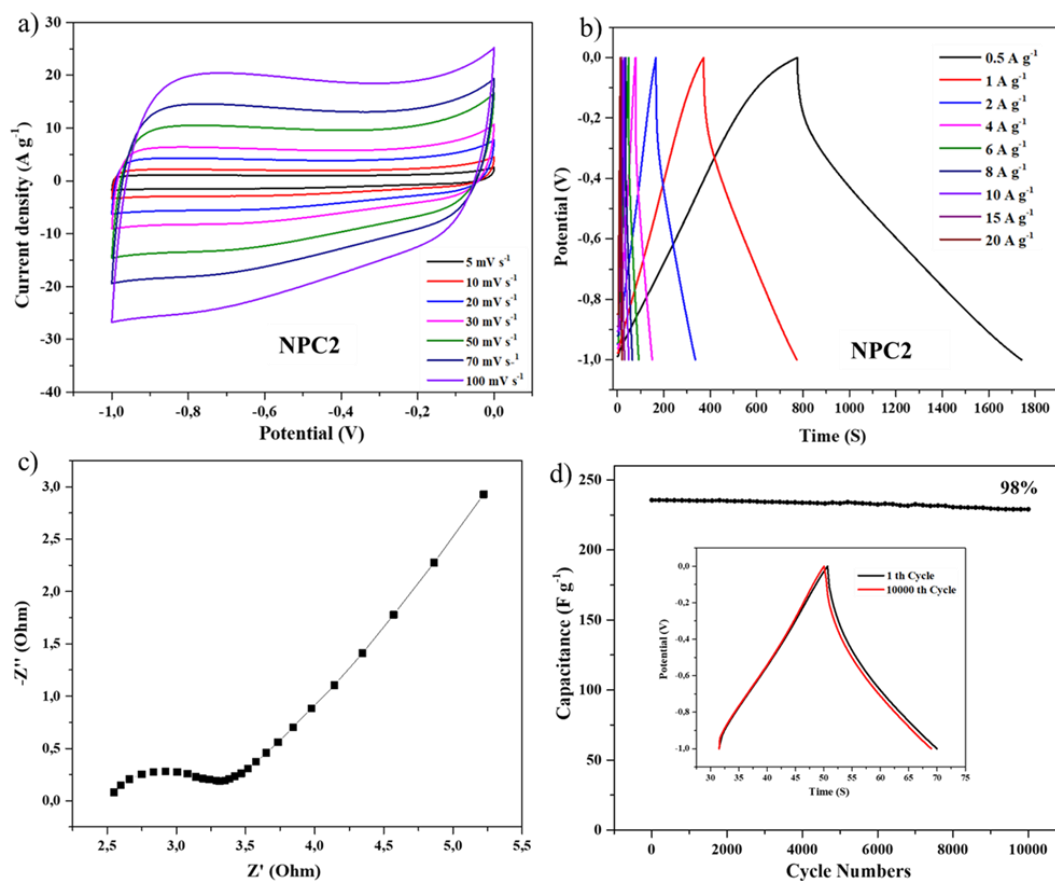
Figure 5.8   (a) CV curves of the NPC2 electrode in 6 M KOH aqueous solution at different scan rates, (b) GCD curves of the NPC2 electrode at different current densities, (c) Nyquist plots of NPC2, (d) Cycling stability of the NPC2 at a current density of 10 A g^{-1} and the inset showing first and last cycles of GCD curves

To demonstrate the practical application of as-prepared NPC2 sample for supercapacitors, a symmetrical two-electrode device was assembled using an electrolyte of 6 M KOH under a potential range of 0-0.8 V. CV and GCD measurements were employed to evaluate the electrochemical performance of the devices, as shown in figure 5.9. The schematic illustration of the assembled symmetric supercapacitor is shown in figure 5.9a. As depicted in figure 5.8a, all the CV curves of the symmetric supercapacitor display quasi-rectangular shapes various scan rates from $5\,\mathrm{mV\,s^{-1}}$ to $100\,\mathrm{mV\,s^{-1}}$. Obviously, When the scanning speed reaches $100\,\mathrm{mV\,s^{-1}}$, the curve still maintains the shape of rectangle, indicating that NPC1 has an ideal capacitive behavior (Xue, Zhu et al. 2019).

GCD curves show good symmetrical triangle at various current densities from 0.5 to $10\,\mathrm{A\,g^{-1}}$, revealing highly reversible charge-discharge behavior (figure 5.9c). The specific capacitance, energy and power density of the supercapacitor were calculated from the GCD curves. As shown in figure 5.8d, the calculated specific capacitance of NPC2 is $193\,\mathrm{F\,g^{-1}}$, even when the current density increased up to $10\,\mathrm{A\,g^{-1}}$, the specific capacitance still maintains $147\,\mathrm{F\,g^{-1}}$ with the retention of 77.0%, demonstrating the good rate capability of the NPC2. Besides, the Ragone plot of the NPC2 symmetric supercapacitor device was calculated from the discharge curves using the equations (3) and (4). As presented in figure 5.9e, the NPC2 delivered the energy density of $13.2\,\mathrm{W\,h\,kg^{-1}}$ at a power density of $700\,\mathrm{W\,kg^{-1}}$ under $0.5\,\mathrm{A\,g^{-1}}$, and retained the energy density of $7.4\,\mathrm{W\,h\,kg^{-1}}$ at $6800\,\mathrm{W\,kg^{-1}}$, which is better than many carbon materials reported previously (Guo and Gao 2009, Le, Yang et al. 2015, Chen, Huang et al. 2016, Yuan, Hu et al. 2017, Xue, Zhu et al. 2019, Shen, Mo et al. 2020, Sun, Xue et al. 2020).
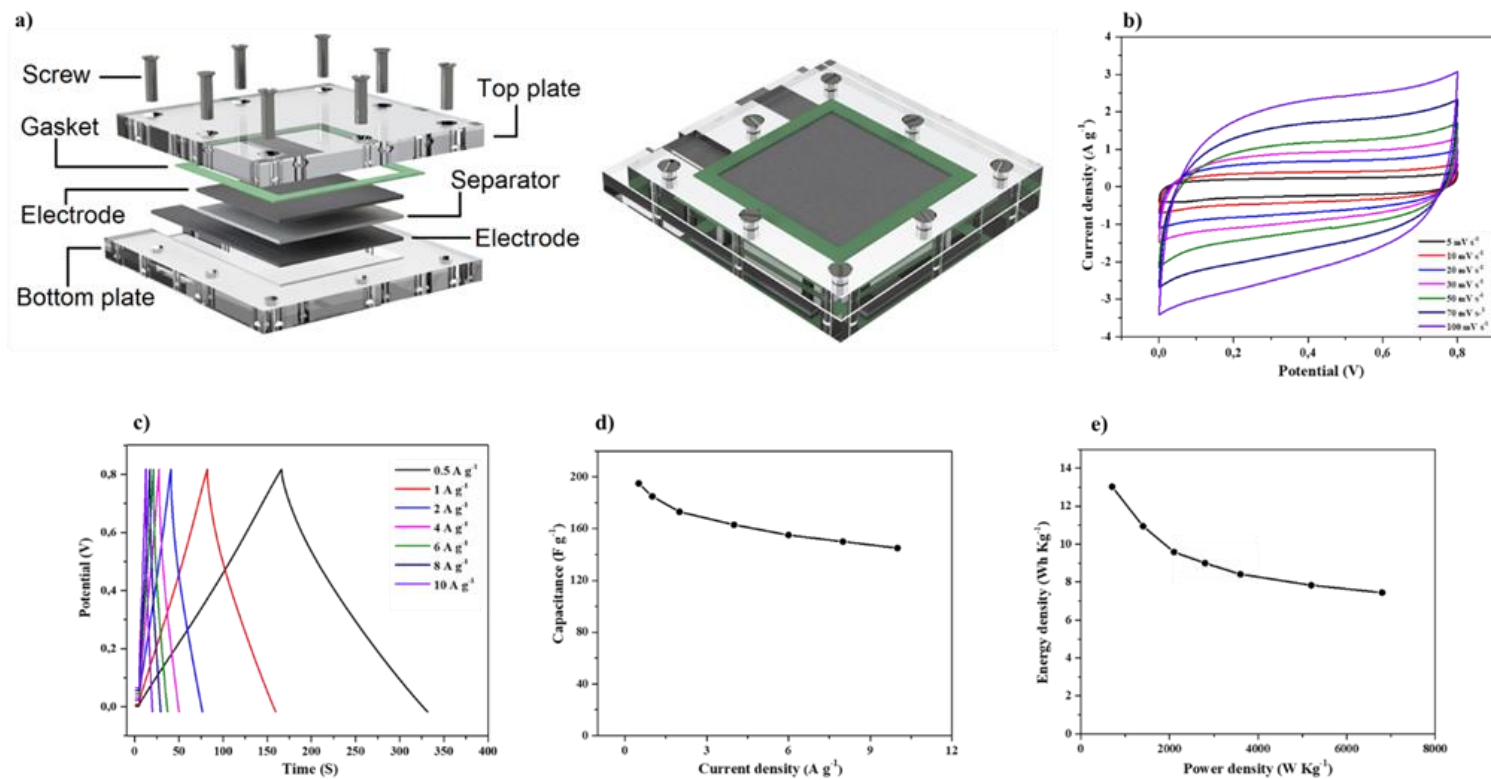
Figure 5.9 (a) The schematic illustration of the assembled symmetric supercapacitor, (b) CV curves of the symmetric supercapacitor measured at different scan rates under a potential range of 0-0.8 V in 6 M KOH electrolyte, (c) GCD curves of the symmetric supercapacitor at different current densities, (d) Specific capacitance of NPC2 under variable current densities and (e) Ragone plot of the NPC2 device

5.6   Conclusion

In summary, NPCx have been successfully prepared by means of carbonizing cyclomatrix polyphosphazene, which is synthesized by a polymerization technique between hexachlorocyclotriphosphazene and *p*-phenylenediamine (or Tris(4-aminophenyl) amine). The obtained N/P co-doped carbon materials have a hierarchical porous structure, providing a channel for the transport and storage of electrons and ions as supercapacitor electrode, the specific capacitance of the NPC2 displays a high specific capacitance of 483 F g^{-1} at 0.5 A g^{-1} in a 6M KOH electrolyte, revealing a superior performance rate. The capacity retention after 10,000 consecutive charge-discharge cycles at 20 A g^{-1} is 98%, demonstrating excellent cycling stability. The assembled symmetric supercapacitor exhibits an energy density of 13.2 W h kg^{-1} at a power density of 700 W kg^{-1}. These results indicated that the heteroatoms doped in carbon sheets would enhance electrochemical performance, which opens the pathway for fabrication of high-surface-area hierarchical activated carbon for energy storage devices with high performance.

CHAPITRE VI

CONCLUSION ET PERSPECTIVES

L'oxyde de graphène (OG) est l'un des derniers nés de lignée d'allotropes de carbone, il est un excellent candidat pour la fabrication de nanocomposites en raison de la présence de groupes oxygène.

Dans cette thèse, nous avons présenté l'historique de la synthèse de l'OG, sa structure et les fondements théoriques des techniques de caractérisation de pointe des matériaux. Une brève description des matériaux carbonés dopés aux hétéroatomes et leurs applications comme retardataires de flamme et comme supercondensateurs (Chapitre I).

Ensuite, nous avons présenté le Chapitre II, présentant un manuscrit publié dans *ACS Omega* (2020). Une nouvelle méthode de préparation d'oxyde de graphène fonctionnalisé (FGO). Le FGO obtenu a été préparé par une réaction d'hexachlorocyclotriphosphazène et de *p*-phénylendiamine avec GO. Ce matériaux (FGO) a démontré une excellente stabilité thermique par l'analyse TGA et une excellente capacité ignifuge par les tests de flamme. L'incorporation de résines époxy sur GO et FGO a démontré que EP@FGO présentait une résistance au feu beaucoup plus élevée. De plus, la fonctionnalisation de l'oxyde de graphène par HCCP et *p*-PDA a été étroitement analysée par différentes techniques spectroscopiques, notamment FTIR, spectroscopie Raman et RMN à l'état solide. D'autres techniques telles que le SEM, EDX et TEM haute résolution ont été utilisées pour démontrées les différences structurelles entre GO et FGO et ont confirmées la présence d'azote et de phosphore sur le FGO. Finalement, l'incorporation des anneaux de phosphazène dans la résine

époxy offre une bonne inflammabilité grâce à la combinaison unique de phosphore et d'azote.

Le Chapitre III, présentant un manuscrit publié dans ACS Omega (2023). Ce manuscrit a couvert une nouvelle voie pour la synthèse des microsphères de type polyphosphazène cyclomatrix par polymérisation en un seul pot d'hexachlorocyclotriphosphazène (HCCP) et de *p*-phénylènediamine (*p*-PDA) en présence de triéthylamine (TEA) comme retardateur de flamme. De plus, des résines époxy thermodurcissables ont été préparées en incorporant l'éther diglycidylique de bisphénol A (DGEBA) et divers pourcentages (2, 5 et 10%) de C-PPZ. Les résultats obtenus ont démontré que la taille et la morphologie des microsphères changent progressivement en fonction de l'augmentation de la température (100, 120 °C et 200 °C) avec un diamètre de 3,12 μm, 4,9 μm à 7,7 μm successivement. Nous avons observé aussi que les microsphères C-CPPZ avaient une bonne stabilité thermique jusqu'à 900 °C, avec une perte de masse d'environ 10% en poids pour le C-CPPZ formé à 200 ° C.

Le Chapitre IV, a été consacré à l'étude des dispositifs de stockage d'énergie comme les supercondensateurs avec leurs diverses applications. Comme précurseur clé, le GO a été synthétisé avec de l'hexachlorocyclotriphosphazène et du p-phénylènediamine. Les résultats ont démontré que le PN-rGO a une structure poreuse avec une morphologie de couche mince transparente et ridée. De plus, le test électrochimique du a révélé que le PN-rGO possède des propriétés capacitives améliorées (capacité spécifique élevée de 292 F g^{-1} à 0,5 A g^{-1}) et une capacité de débit remarquable par rapport au rGO non dopé et une excellente stabilité de cycle. Le supercondensateur symétrique composite PN-rGO développé présente aussi une densité d'énergie relativement élevée de 8,2 Whkg^{-1} à une densité de puissance de 570 Wkg^{-1} dans l'électrolyte KOH.

Le Chapitre V, couvre la préparation du carbone poreux co-dopé azote/phosphore comme matériau d'électrode efficace pour les supercondensateurs avec une méthode simple et efficace. L'électrode de courant NPC2 a révélé une capacité spécifique élevée de 483 F g^{-1} à 0,5 A g^{-1} et présente d'excellentes performances électrochimiques avec une excellente stabilité de 98% après 10 000 cycles continus de charge-décharge à 20 A g^{-1}. Nous avons assemblé aussi un supercondensateur symétrique.

Comme perspectives, de nouveaux catalyseurs pour le dégagement ou la réduction d'oxygène (OER/ORR) à base de matériaux carbonés fonctionnalisés au polyphosphazène seront à synthétiser. L'étude de ces réactions électrochimiques sur des surfaces aux structures bien définies représente un outil important pour élucider les mécanismes réactionnels, identifier les sites actifs et permettre la déconvolution des réponses électrochimiques de surface. De plus, la présence d'une structure carbonée favorise le passage des électrons ainsi que des groupements phosphorés et azotés pouvant catalyser cette réaction.

Ce travail pourrait être effectué par une analyse plus approfondie des surfaces de carbone modifiées et par l'étude de la cinétique par des méthodes électrochimiques classiques telles que les électrodes tournantes à disque et à anneau, ce qui permet de déterminer le pourcentage de peroxyde produit et d'évaluer la constante de vitesse de réaction.

APPENDIX A

SUPPORTING INFORMATION FOR:
HEXACHLOROCYCLOTRIPHOSPHAZENE FUNCTIONALIZED GRAPHENE
OXIDE AS HIGHLY EFFICIENT FLAME RETARDANT

Khaled Rhili[a], Siham Chergui[a], Ahmad Samih El Douhaibi[b] and Mohamed Siaj [a],*

[a]Department of Chemistry and Biochemistry, Université du Quebec à Montréal, Montréal QC, H3C 3P8, Canada

[b] Department of Chemistry, Lebanese University, College of Science III, Campus Mont Michel, 1352, Tripoli, Lebanon

*Corresponding author at: Email: siaj.mohamed@uqam.ca
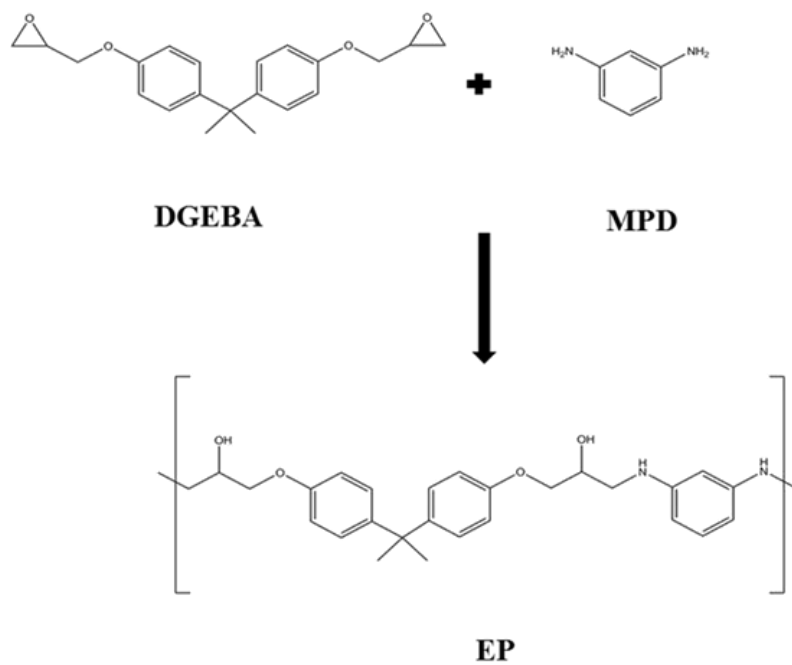
Figure A.1   Illustration of synthetized thermoset epoxy resin
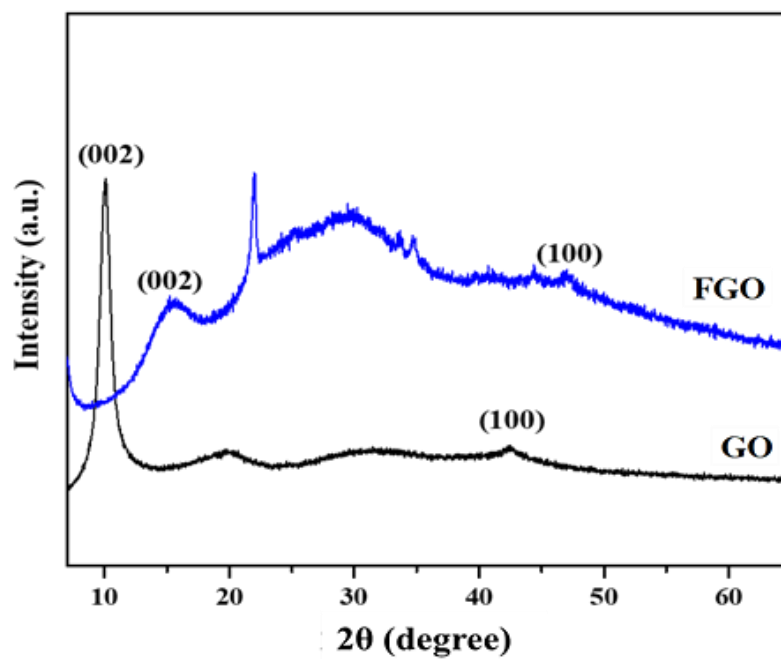
Figure A.2   XRD spectra of GO and FGO
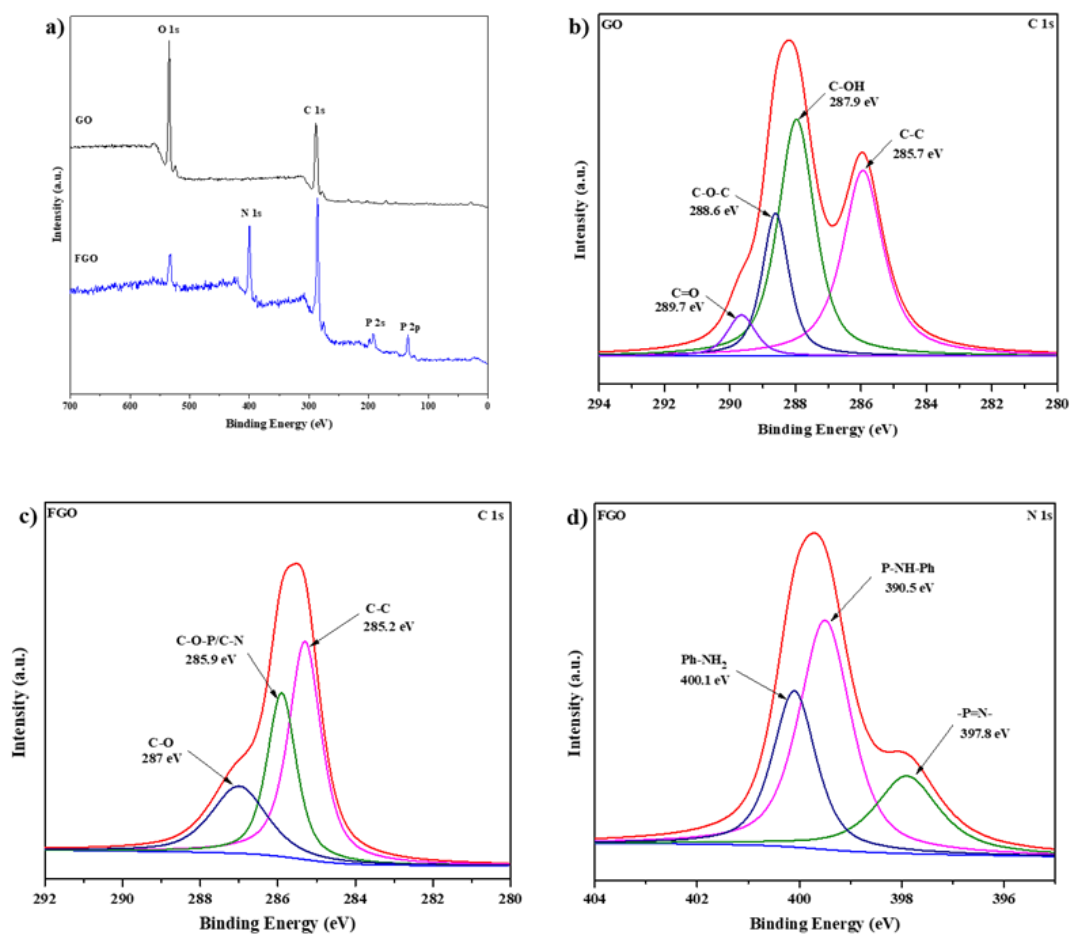
Figure A.3   a) survey spectra of GO and FGO; (b) C 1s spectrum of GO; (c) C 1s and (d) N 1s spectra of FGO
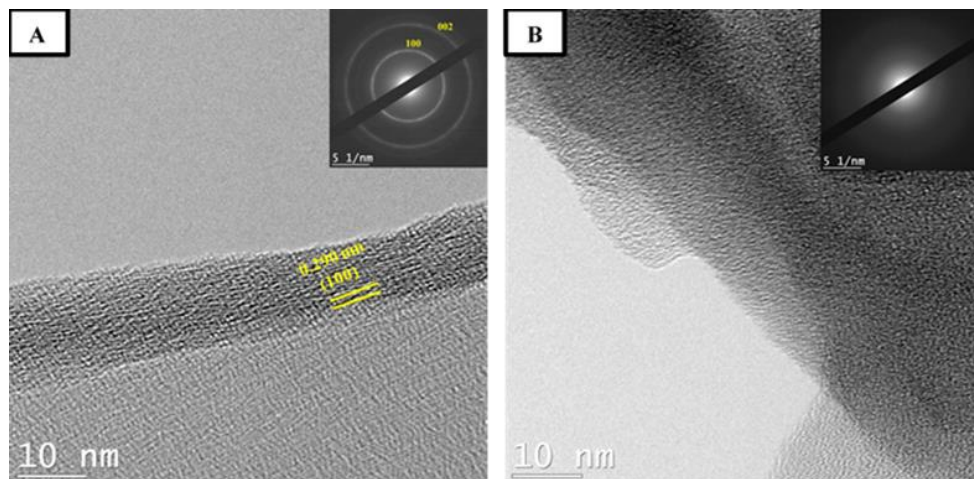
Figure A.4   High-resolution transmission electron microscopy (HRTEM) image with the corresponding SAED pattern (top insert) of (A) (GO) and (B) (FGO)

Tableau A.1   Element content of GO and FGO measured from XPS analysis

Samples	C (at.%)	O (at.%)	P (at.%)	N (at.%)
GO	64.3	35.7	-	-
FGO	63.7	7.9	6.0	22.5

Tableau A.2   Detailed TGA data for EP and its composites under N2 atmosphere

Samples	T_{10}/°C	T_{max} (wt%/°C)	Residue at 800 °C (wt%)
EP	370	-1.85	14
EP@GO2%	341	-1.57	14.7
EP@FGO2%	342	-1.36	18.3
EP@FGO5%	359	-1.18	20.1
EP@FGO10%	317	-0.85	23

APPENDIX B

SUPPORTING INFORMATION FOR: ONE-POT SYNTHESIS OF
CYCLOMATRIX TYPE POLYPHOSPHAZENE MICROSPHERES AND THEIR
HIGH THERMAL STABILITY

Khaled Rhili[a], Siham Chergui[a], Ahmad Samih ElDouhaibi[b], Ahmed Mazzah[c] and

Mohamed Siaj[a]*

[a] Department of Chemistry, University of Quebec at Montreal, Montreal QC, H3C3P8,
Canada

[b] Department of Chemistry, Lebanese University, College of Science III, Campus Mont
Michel, 1352, Tripoli, Lebanon

[c] Université de Lille, CNRS, USR 3290, MSAP, Miniaturisation pour la Synthèse
l'Analyse et la Protéomique, F-59000 Lille, France
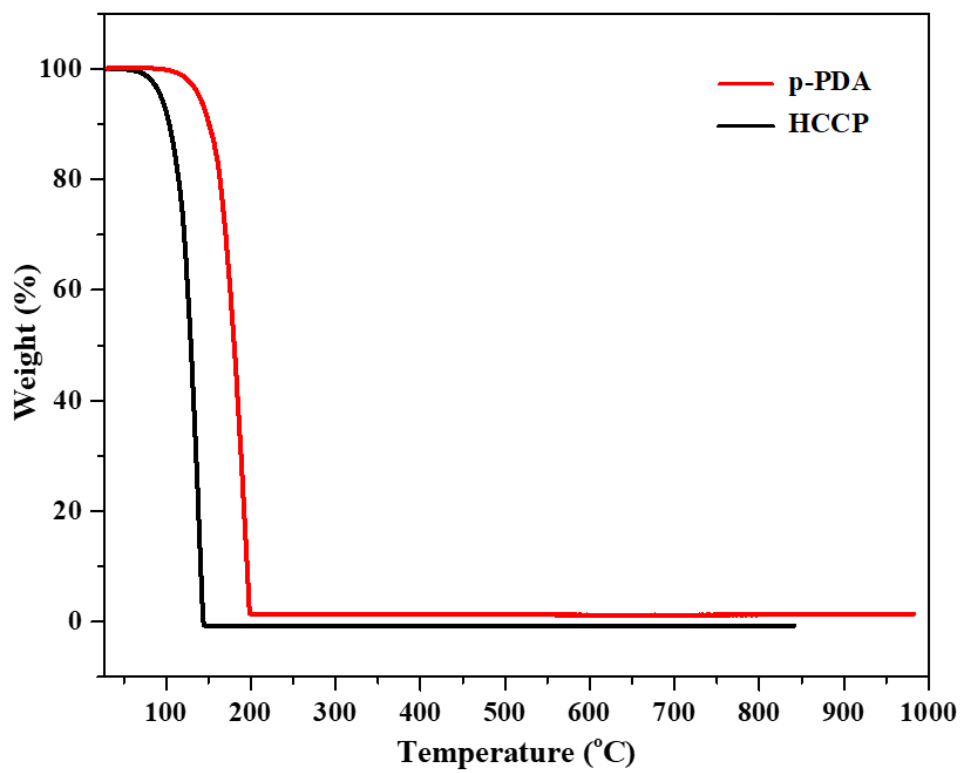
Figure B.1   TGA curve of *p*-PDA and HCCP
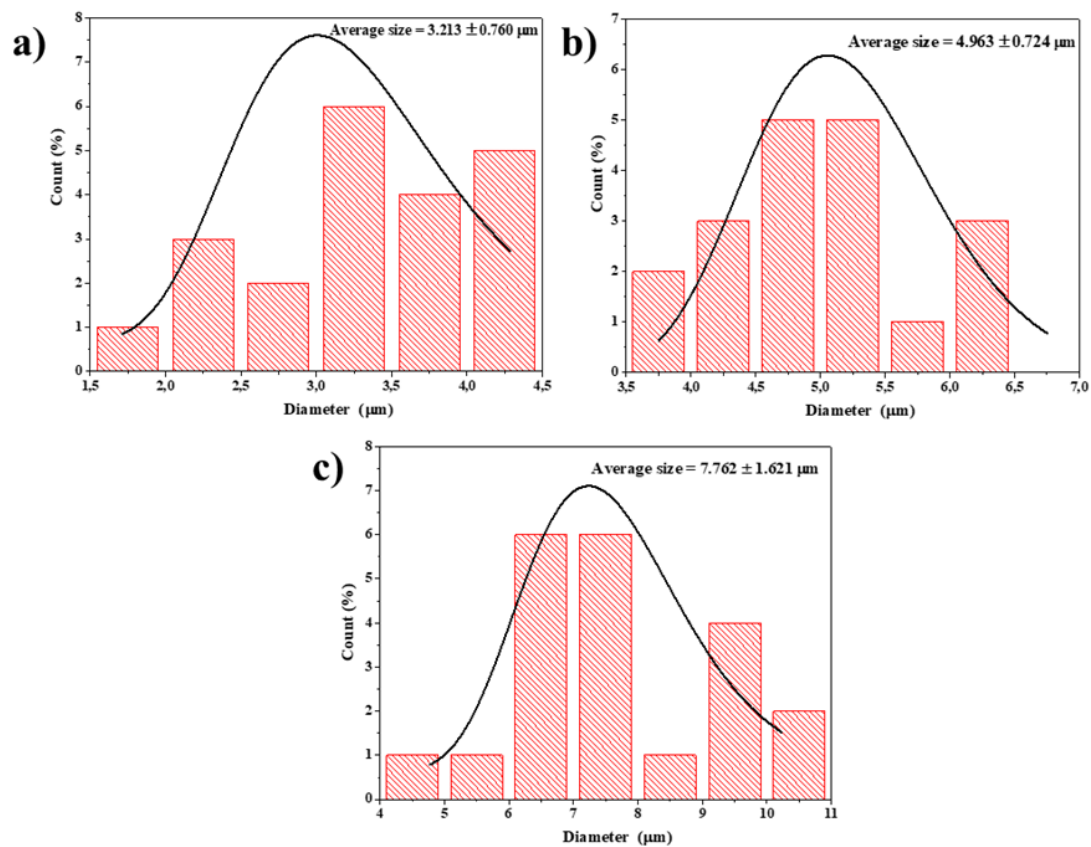
Figure B.2   Particle-size distributions of the C-PPZs microspheres at (a) 100 °C, (b) 120 °C, and (c) 200 °C

APPENDIX C

SUPPORTING INFORMATION FOR: PHOSPHORUS AND NITROGEN CO-
DOPED REDUCED GRAPHENE OXIDE AS SUPERIOR ELECTRODE
MATERIALS FOR SUPERCAPACITORS

Khaled Rhili[a], Siham Chergui[a], Juan Carlos Abrego-Martinez[b], Ahmad Samih
ElDouhaibi[c] Mohamed Mohamedi[b] and Mohamed Siaj[a]*

[a]Department of Chemistry and Biochemistry, University of Quebec at Montreal,
Montreal QC, H3C 3P8, Canada

[b]Énergie, Matériaux et Télécommunications (EMT), Institut National de la Recherche
Scientifique (INRS), 1650 Boulevard Lionel Boulet, Varennes, QC J3X 1P7, Canada

[c] Department of Chemistry, Lebanese University, College of Science III, Campus Mont
Michel, 1352, Tripoli, Lebanon

*Corresponding author at: Email: siaj.mohamed@uqam.ca

C.1   Synthesis of reduced graphene oxide (rGO)

Graphene oxide (GO) was synthesized following a modified Hummer's method, as reported by our group using natural graphite as raw material (Brisebois, Izquierdo et al. 2020, Chergui, Rhili et al. 2020, Rhili, Chergui et al. 2021). Reduced graphene oxide (rGO) was prepared by ultrasonication for 1h of the GO powder (100 mg) in deionised water (100 mL) to achieve a concentration of (1 mg mL^{-1}). Then, the GO suspension was transferred to a 100 mL Teflon-lined autoclave and hydrothermally treated at 200 ^{o}C for 24 h. the obtained product was further pyrolyzing under the same annealing processes.
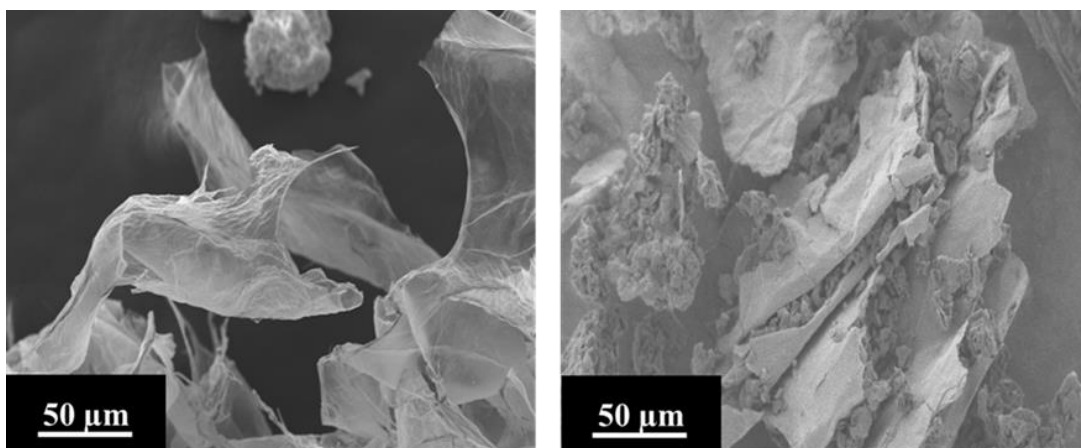
Figure C.1   SEM images of (a) GO and (b) FGO

Tableau C.1   Element content of P, N-rGO measured from XPS analysis

Sample	C (at.%)	O (at.%)	P (at.%)	N (at.%)
P, N-rGO	81.2	12	2.3	4.5
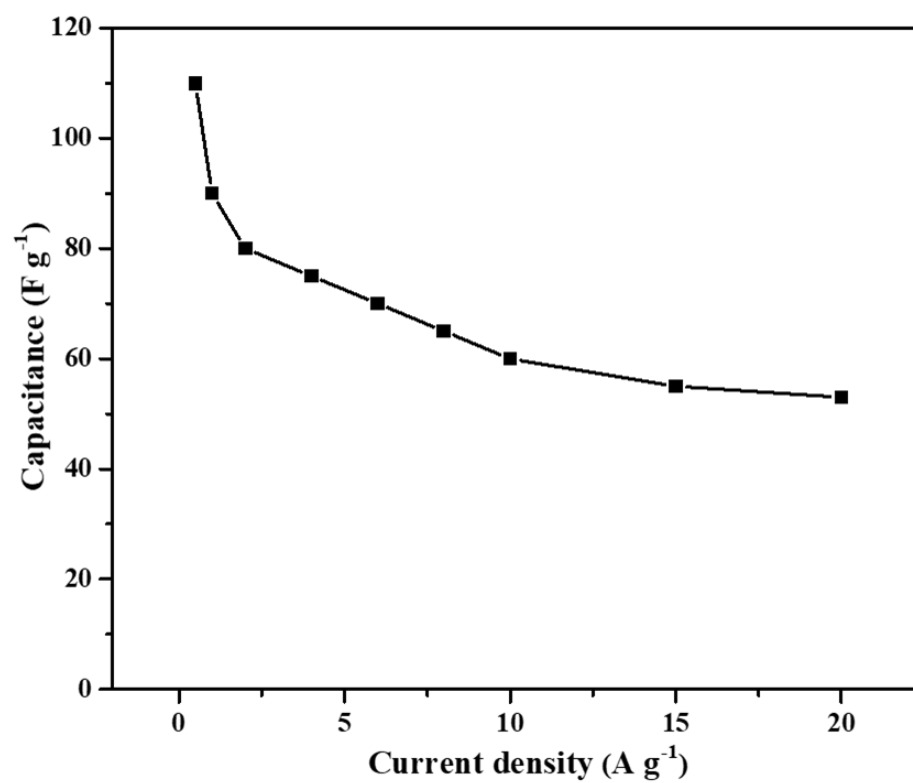
Figure C.2   Specific capacitances of rGO at different current densities

APPENDIX D

SUPPORTING INFORMATION FOR: NITROGEN/PHOSPHORUS CO-DOPED POROUS CARBON AS AN EFFICIENT ELECTRODE MATERIAL FOR SUPERCAPACITORS

Khaled Rhili[a], Siham Chergui[a], Ahmad Samih ElDouhaibi[b] and Mohamed Siaj[a]*

[a] Department of Chemistry, University of Quebec at Montreal, Montreal QC, H3C3P8, Canada

[b] Department of Chemistry, Lebanese University, College of Science III, Campus Mont Michel, 1352, Tripoli, Lebanon
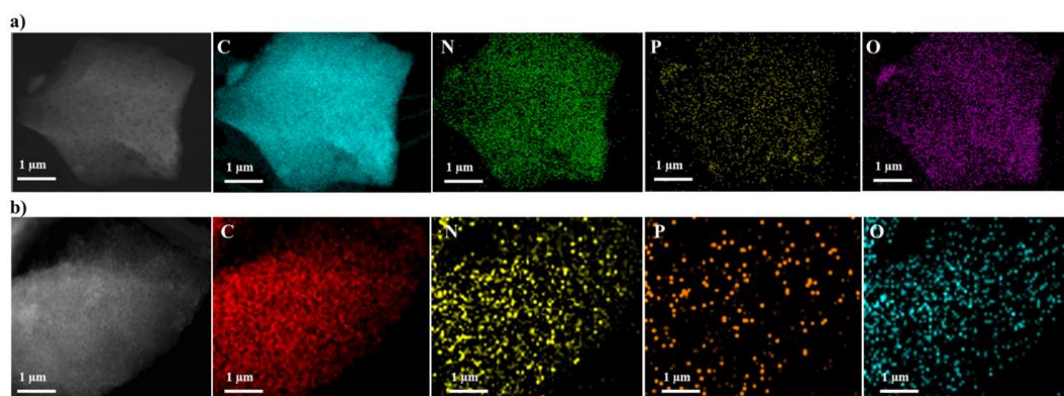
Figure D.1   TEM elemental mapping images of (a) NPC1 and (b) NPC2 with C, N, P and O elements
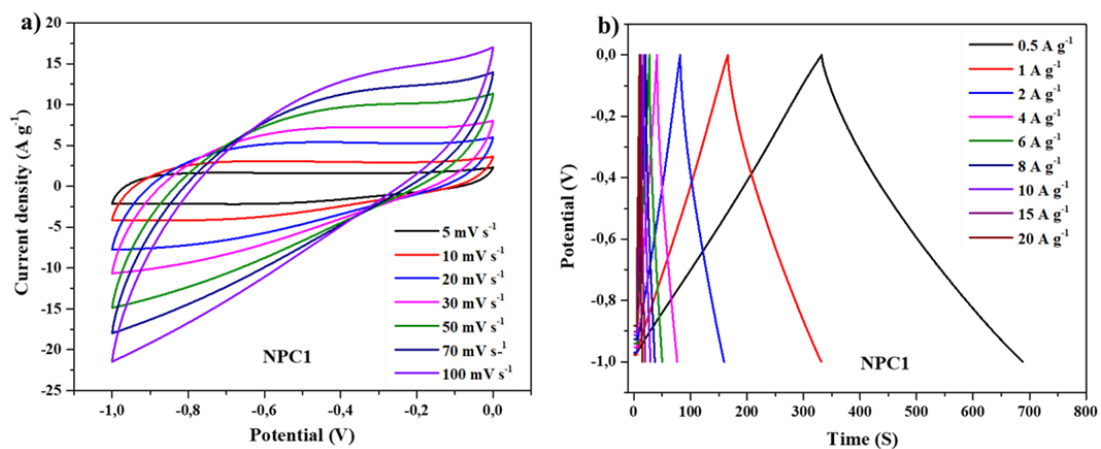
Figure D.2   (a) CV curves of the NPC1 electrode in 6 M KOH aqueous solution at different scan rates and (b) GCD curves of the NPC1 electrode at different current densities

Tableau D.1 BET surface area and pore structure characterization of NPC1 and NPC2

Samples	S_{BET} (m².g⁻¹)	Pore Volume (cm3.g-1)	Average Pore Size (nm)
NPC1	943.3	0.51	2.28
NPC2	1042.7	0.68	2.75

RÉFÉRENCES

Abbas, Y., et al. (2020). "Substantial role of nitrogen and sulfur in quaternary-atom-doped multishelled carbon nanospheres for the oxygen evolution reaction." ACS Sustainable Chemistry & Engineering **8**(10): 4284-4291.

Aliyev, E., et al. (2019). "Structural characterization of graphene oxide: Surface functional groups and fractionated oxidative debris." Nanomaterials **9**(8): 1180.

Allcock, H. R. (2006). "A perspective of polyphosphazene research." Journal of Inorganic and Organometallic Polymers and Materials **16**: 277-294.

Allcock, H. R. (2006). "A perspective of polyphosphazene research." Journal of Inorganic and Organometallic Polymers and Materials **16**(4): 277-294.

Allcock, H. R. (2016). "The expanding field of polyphosphazene high polymers." Dalton Transactions **45**(5): 1856-1862.

Allcock, H. R., et al. (1990). "Influence of different organic side groups on the thermal behavior of polyphosphazenes: Random chain cleavage, depolymerization, and pyrolytic cross-linking." Chemistry of Materials **2**(4): 425-432.

Allcock, H. R. and N. L. Morozowich (2012). "Bioerodible polyphosphazenes and their medical potential." Polymer Chemistry **3**(3): 578-590.

Ananthanarayanan, A., et al. (2015). "Nitrogen and phosphorus co-doped graphene quantum dots: synthesis from adenosine triphosphate, optical properties, and cellular imaging." Nanoscale **7**(17): 8159-8165.

B, S. F. a. C. (2018). "Glucose-Reduced Nano-Graphene Oxide with Excellent Accumulation

Removal of Pharmaceuticals and Personal Care Products from Water." Journal of Environmental Analytical

Chemistry.

Bai, Y., et al. (2013). "Effect of pH-induced chemical modification of hydrothermally reduced graphene oxide on supercapacitor performance." Journal of Power Sources **233**: 313-319.

Bajjou, O., et al. (2018). "Charge Carrier Dynamics and pH Effect on Optical Properties of Anionic and Cationic Porphyrin–Graphene Oxide Composites." Journal of Electronic Materials **47**(5): 2897-2904.

Bao, C., et al. (2012). "Functionalized graphene oxide for fire safety applications of polymers: a combination of condensed phase flame retardant strategies." Journal of Materials Chemistry **22**(43): 23057-23063.

Bao, C., et al. (2012). "Graphite oxide, graphene, and metal-loaded graphene for fire safety applications of polystyrene." Journal of Materials Chemistry **22**(32): 16399-16406.

Barzegar, F., et al. (2015). "Synthesis of 3D porous carbon based on cheap polymers and graphene foam for high-performance electrochemical capacitors." Electrochimica Acta **180**: 442-450.

Berrueta, A., et al. (2019). "Supercapacitors: electrical characteristics, modeling, applications, and future trends." Ieee Access **7**: 50869-50896.

Bissessur, R. and S. F. Scully (2007). "Intercalation of solid polymer electrolytes into graphite oxide." Solid State Ionics **178**(11-12): 877-882.

Brisebois, P., et al. (2020). "Room-Temperature reduction of graphene oxide in water by metal chloride hydrates: A cleaner approach for the preparation of graphene@ metal hybrids." Nanomaterials **10**(7): 1255.

Brisebois, P. and M. Siaj (2020). "Harvesting graphene oxide–years 1859 to 2019: a review of its structure, synthesis, properties and exfoliation." Journal of Materials Chemistry C **8**(5): 1517-1547.

Brisebois, P. P., et al. (2016). "New Insights into the Diels–Alder Reaction of Graphene Oxide." Chemistry–A European Journal **22**(17): 5849-5852.

Brodie, B. C. (1859). "XIII. On the atomic weight of graphite." Philosophical transactions of the Royal Society of London(149): 249-259.

Burke, A. (2007). "R&D considerations for the performance and application of electrochemical capacitors." Electrochimica Acta **53**(3): 1083-1091.

Caminade, A.-M., et al. (2016). "The specific functionalization of cyclotriphosphazene for the synthesis of smart dendrimers." Dalton Transactions **45**(5): 1810-1822.

Cao, J. and A. Emadi (2011). "A new battery/ultracapacitor hybrid energy storage system for electric, hybrid, and plug-in hybrid electric vehicles." IEEE Transactions on power electronics **27**(1): 122-132.

Carja, I.-D., et al. (2014). "A straightforward, eco-friendly and cost-effective approach towards flame retardant epoxy resins." Journal of Materials Chemistry A **2**(38): 16230-16241.

Carriedo, G. A. (2007). "POLYPHOSPHAZENES WITH P (DIOXY-BIARYL) CYCLES IN THE REPEATING UNITS: A REVIEW." Journal of the Chilean Chemical Society **52**(2): 1190-1195.

Chang, Y., et al. (2019). "Flexible supercapacitor electrode with high performance prepared from graphene oxide films assembled in the presence of p-phenylenediamine and urea." Journal of Materials Science: Materials in Electronics **30**(8): 7216-7225.

Chapman, D. L. (1913). "LI. A contribution to the theory of electrocapillarity." The London, Edinburgh, and Dublin philosophical magazine and journal of science **25**(148): 475-481.

Chaudhary, M., et al. (2018). "Nitrogen-enriched nanoporous polytriazine for high-performance supercapacitor application." ACS Sustainable Chemistry & Engineering **6**(5): 5895-5902.

Chen, D., et al. (2012). "Graphene oxide: preparation, functionalization, and electrochemical applications." Chemical reviews **112**(11): 6027-6053.

Chen, H., et al. (2013). "Nitrogen doping effects on the physical and chemical properties of mesoporous carbons." The Journal of Physical Chemistry C **117**(16): 8318-8328.

Chen, J., et al. (2018). "N/P co-doped hierarchical porous carbon materials for superior performance supercapacitors." Electrochimica Acta **271**: 49-57.

Chen, K., et al. (2016). "Heteroatom–doped hollow carbon microspheres based on amphiphilic supramolecular vesicles and highly crosslinked polyphosphazene for high performance supercapacitor electrode materials." Electrochimica Acta **222**: 543-550.

Chen, W., et al. (2018). "Non-covalently functionalized graphene oxide-based coating to enhance thermal stability and flame retardancy of PVA film." Nano-micro letters **10**(3): 1-13.

Chen, W., et al. (2018). "Non-covalently functionalized graphene oxide-based coating to enhance thermal stability and flame retardancy of PVA film." Nano-micro letters **10**(3): 39.

Chen, W., et al. (2012). "High energy density supercapacitors using macroporous kitchen sponges." Journal of Materials Chemistry **22**(29): 14394-14402.

Chen, X., et al. (2015). "N-doped graphene as an electron donor of iron catalysts for CO hydrogenation to light olefins." Chemical Communications **51**(1): 217-220.

Chen, X., et al. (2016). "Three-dimensional activated carbon recycled from rotten potatoes for high-performance supercapacitors." Waste and biomass valorization **7**(3): 551-557.

Cheng, H., et al. (2019). "Supermolecule self-assembly promoted porous N, P Co-doped reduced graphene oxide for high energy density supercapacitors." ACS Applied Energy Materials **2**(6): 4084-4091.

Chergui, S. (2018). Fabrication et biofonctionnalisation d'une mousse d'oxyde de graphène par des aptamères pour une décontamination sélective en milieu aqueux.

Chergui, S., et al. (2020). "Graphene Oxide Membrane Immobilized Aptamer as a Highly Selective Hormone Removal." Membranes **10**(9): 229.

Chiang, C. and J. Yang (2015). Flame retardance and thermal stability of polymer/graphene nanosheet oxide composites. Fillers and Reinforcements for Advanced Nanocomposites, Elsevier**:** 253-272.

Compton, O. C. and S. T. Nguyen (2010). "Graphene oxide, highly reduced graphene oxide, and graphene: versatile building blocks for carbon-based materials." small **6**(6): 711-723.

Costa, L. and G. Camino (1988). "Thermal behaviour of melamine." Journal of Thermal Analysis and Calorimetry **34**(2): 423-429.

Covaci, A., et al. (2003). "Determination of brominated flame retardants, with emphasis on polybrominated diphenyl ethers (PBDEs) in environmental and human samples—a review." Environment international **29**(6): 735-756.

Crouzet, L. and D. Leclercq (2000). "Polyphosphazene–metal oxide hybrids by nonhydrolytic sol–gel processes." Journal of Materials Chemistry **10**(5): 1195-1201.

Dar, S. U., et al. (2016). "A facile synthesis, structural morphology and fluorescent properties of cross-linked poly (cyclotriphosphazene-co-1, 3, 5-tri (4-hydroxyphenyl) benzene) hybrid copolymer microspheres." New Journal of Chemistry **40**(10): 8418-8423.

Dasari, A., et al. (2013). "Recent developments in the fire retardancy of polymeric materials." Progress in Polymer Science **38**(9): 1357-1387.

Davy, R. D., et al. (1991). "Phosphoryl nitride isomeric dimers, trimers, and tetramers:(NPO) x (X= 2-4)." Journal of the American Chemical Society **113**(11): 4136-4138.

Dimiev, A. M., et al. (2012). "Graphene oxide. Origin of acidity, its instability in water, and a new dynamic structural model." ACS nano **7**(1): 576-588.

Döring, M. and J. Diederichs (2007). "Halogen-free flame retardants in E&E applications." Forschungszentrum Karlsruhe, Germany.

Dreyer, D. R., et al. (2011). "Graphite oxide: a selective and highly efficient oxidant of thiols and sulfides." Organic & Biomolecular Chemistry **9**(21): 7292-7295.

Du, F.-P., et al. (2012). "Water-soluble graphene grafted by poly (sodium 4-styrenesulfonate) for enhancement of electric capacitance." Nanotechnology **23**(47): 475704.

Eftekhari, A. (2018). "The mechanism of ultrafast supercapacitors." Journal of Materials Chemistry A **6**(7): 2866-2876.

El-Kaderi, H. M., et al. (2007). "Designed synthesis of 3D covalent organic frameworks." science **316**(5822): 268-272.

Fan, J., et al. (2014). "Layered double hydroxide–polyphosphazene-based ionomer hybrid membranes with electric field-aligned domains for hydroxide transport." Journal of Materials Chemistry A **2**(22): 8376-8385.

Friederich, B. (2011). Développement de Nouveaux systèmes retardateurs de flammes à base de nanocomposites plus respectueux de l'environnement, Université Paul Verlaine-Metz.

Fu, J., et al. (2008). "An attempt to prepare carbon nanotubes by carbonizing polyphosphazene nanotubes with high carbon content." Materials Letters **62**(25): 4130-4133.

Gadipelli, S. and Z. X. Guo (2015). "Graphene-based materials: Synthesis and gas sorption, storage and separation." Progress in Materials Science **69**: 1-60.

Gao, L.-P., et al. (2008). "A flame-retardant epoxy resin based on a reactive phosphorus-containing monomer of DODPP and its thermal and flame-retardant properties." Polymer Degradation and stability **93**(7): 1308-1315.

Gao, M., et al. (2018). "A self-template and self-activation co-coupling green strategy to synthesize high surface area ternary-doped hollow carbon microspheres for high performance supercapacitors." Journal of colloid and interface science **524**: 165-176.

Geim, A. K. and K. S. Novoselov (2007). "The rise of graphene." Nat Mater **6**(3): 183-191.

Geyer, R., et al. (2017). "Production, use, and fate of all plastics ever made." Science advances **3**(7): e1700782.

Gouy, M. (1910). "Sur la constitution de la charge électrique à la surface d'un électrolyte." J. Phys. Theor. Appl. **9**(1): 457-468.

Guo, D., et al. (2016). "Active sites of nitrogen-doped carbon materials for oxygen reduction reaction clarified using model catalysts." Science **351**(6271): 361-365.

Guo, H. and Q. Gao (2009). "Boron and nitrogen co-doped porous carbon and its enhanced properties as supercapacitor." Journal of power sources **186**(2): 551-556.

Guo, N., et al. (2016). "Soybean root-derived hierarchical porous carbon as electrode material for high-performance supercapacitors in ionic liquids." ACS applied materials & interfaces **8**(49): 33626-33634.

Guo, X., et al. (2018). "Synthesis and application of a dual functional P/N/S-containing microsphere with enhanced flame retardancy and mechanical strength on EP resin." Polymers for Advanced Technologies **29**(10): 2665-2673.

He, Y., et al. (2016). "Bifunctional nitrogen-doped microporous carbon microspheres derived from poly (o-methylaniline) for oxygen reduction and supercapacitors." ACS Applied Materials & Interfaces **8**(6): 3601-3608.

Helmholtz, H. v. (1879). "Studien über electrische Grenzschichten." Annalen der Physik **243**(7): 337-382.

Herbiet, R. (2000). New metal hydroxides with improved performance for flame retardancy in plastics. Addcon world 2000 (Basel, 25-26 october, 2000).

Hong, S., et al. (2018). "A facile approach to generate cross-linked poly (cyclotriphosphazene-co-oxyresveratrol) nanoparticle with intrinsically fluorescence." Journal of Inorganic and Organometallic Polymers and Materials **28**(6): 2258-2263.

Hu, L., et al. (2018). "Natural biomass-derived hierarchical porous carbon synthesized by an in situ hard template coupled with NaOH activation for ultrahigh rate supercapacitors." ACS Sustainable Chemistry & Engineering **6**(11): 13949-13959.

Hu, W., et al. (2014). "Effect of functionalized graphene oxide with hyper-branched flame retardant on flammability and thermal stability of cross-linked polyethylene." Industrial & Engineering Chemistry Research **53**(8): 3073-3083.

Huang, Z., et al. (2015). "Water-triggered self-assembly polycondensation for the one-pot synthesis of cyclomatrix polyphosphazene nanoparticles from amino acid ester." Chemical Communications **51**(39): 8373-8376.

Hulicova-Jurcakova, D., et al. (2009). "Combined effect of nitrogen-and oxygen-containing functional groups of microporous activated carbon on its electrochemical performance in supercapacitors." Advanced Functional Materials **19**(3): 438-447.

Hwang, M.-J., et al. (2019). "Cathodic electrophoretic deposition (EPD) of phenylenediamine-modified graphene oxide (GO) for anti-corrosion protection of metal surfaces." Carbon **142**: 68-77.

Iijima, S. (1991). "Helical microtubules of graphitic carbon." Nature **354**(6348): 56-58.

Inagaki, M. (2010). "H, Konno, O. Tanaike." J. Power Sources **195**: 7880-7903.

Islam, S. M., et al. (2014). "Graphene based material as a base catalyst for solvent free Aldol condensation and Knoevenagel reaction at room temperature." Journal of Molecular Catalysis A: Chemical **394**: 66-73.

Jacob, G. M., et al. (2009). "Composite electrodes for electrochemical supercapacitors." Journal of applied electrochemistry **39**(12): 2579-2585.

Jenkins, E. W. (1973). The polymorphism of elements and compounds, Taylor & Francis.

Jian, R., et al. (2016). "Synthesis of a novel P/N/S-containing flame retardant and its application in epoxy resin: thermal property, flame retardance, and pyrolysis behavior." Industrial & Engineering Chemistry Research **55**(44): 11520-11527.

Jiang, S., et al. (2014). "Bismuth subcarbonate nanoplates for thermal stability, fire retardancy and smoke suppression applications in polymers: a new strategy." Polymer degradation and stability **107**: 1-9.

Jin, L., et al. (2019). "Preparation of stable and high-efficient poly (m-phenylenediamine)/reduced graphene oxide composites for hexavalent chromium removal." Journal of Materials Science **54**(1): 383-395.

Kamila, S., et al. (2017). "Highly active 2D layered MoS 2-rGO hybrids for energy conversion and storage applications." Scientific reports **7**(1): 1-13.

Kandalkar, S. G., et al. (2010). "Chemical synthesis of cobalt oxide thin film electrode for supercapacitor application." Synthetic Metals **160**(11): 1299-1302.

Kandjou, V., et al. (2019). "Enhanced covalent p-phenylenediamine crosslinked graphene oxide membranes: Towards superior contaminant removal from wastewaters and improved membrane reusability." Journal of hazardous materials **380**: 120840.

Kaniyoor, A., et al. (2010). "Graphene synthesis via hydrogen induced low temperature exfoliation of graphite oxide." Journal of Materials Chemistry **20**(39): 8467-8469.

Katsnelson, M., et al. (2006). "Chiral tunnelling and the Klein paradox in graphene." Nature physics **2**(9): 620-625.

Kaviyarasu, K., et al. (2015). "Well-aligned graphene oxide nanosheets decorated with zinc oxide nanocrystals for high performance photocatalytic application." International Journal of Nanoscience **14**(03): 1550007.

Khandelwal, M. and A. Kumar (2015). "One-step chemically controlled wet synthesis of graphene nanoribbons from graphene oxide for high performance supercapacitor applications." Journal of Materials Chemistry A **3**(45): 22975-22988.

Kim, B.-H., et al. (2011). "Thin, bendable electrodes consisting of porous carbon nanofibers via the electrospinning of polyacrylonitrile containing tetraethoxy orthosilicate for supercapacitor." Electrochemistry Communications **13**(10): 1042-1046.

Kim, B. K., et al. (2015). "Electrochemical supercapacitors for energy storage and conversion." Handbook of clean energy systems: 1-25.

Kötz, R. and M. Carlen (2000). "Principles and Applications of Electrochemical Capacitors." Electrochimica Acta **45**: 2483-2498.

Kouchachvili, L., et al. (2018). "Hybrid battery/supercapacitor energy storage system for the electric vehicles." Journal of power sources **374**: 237-248.

Kroto, H. W., et al. (1985). "C60: Buckminsterfullerene." Nature **318**(6042): 162-163.

Kumar, A. V. and K. R. Rao (2011). "Recyclable graphite oxide catalyzed Friedel–Crafts addition of indoles to α, β-unsaturated ketones." Tetrahedron letters **52**(40): 5188-5191.

Kumar, D., et al. (1983). "Fire-and heat-resistant laminating resins based on maleimido-substituted aromatic cyclotriphosphazenes." Macromolecules **16**(8): 1250-1257.

Kumar, D., et al. (1993). "Synthesis and characterization of novel cyclotriphosphazene-containing poly (ether imide) s." Polymer **34**(14): 3025-3029.

Lai, L., et al. (2012). "Exploration of the active center structure of nitrogen-doped graphene-based catalysts for oxygen reduction reaction." Energy & Environmental Science **5**(7): 7936-7942.

Lai, L., et al. (2012). Preparation of supercapacitor electrodes through selection of graphene surface functionalities.

Le, T., et al. (2015). "Preparation of microporous carbon nanofibers from polyimide by using polyvinyl pyrrolidone as template and their capacitive performance." Journal of power sources **278**: 683-692.

Lee, J.-W., et al. (2012). "Phosphoric acid-functionalized mesoporous silica/nafion composite membrane for high temperature PEMFCs." Bulletin of the Korean Chemical Society **33**(4): 1397-1400.

Lei, E., et al. (2018). "CO2-activated porous self-templated N-doped carbon aerogel derived from banana for high-performance supercapacitors." Applied Surface Science **457**: 477-486.

Lei, L., et al. (2016). "Preparation and properties of amino-functional reduced graphene oxide/waterborne polyurethane hybrid emulsions." Progress in organic coatings **97**: 19-27.

Leikach, D. (2007). An assessment of the use of flame retardant plastics for museum applications, University of Maryland, College Park.

Li, B., et al. (2016). "Nitrogen-doped activated carbon for a high energy hybrid supercapacitor." Energy & Environmental Science **9**(1): 102-106.

Li, J.-C., et al. (2019). "Identification of active sites in nitrogen and sulfur co-doped carbon-based oxygen reduction catalysts." Carbon **147**: 303-311.

Li, J., et al. (2019). "Tunable stable operating potential window for high-voltage aqueous supercapacitors." Nano Energy **63**: 103848.

Li, J., et al. (2017). "Tuning the performance of nitrogen, phosphorus co-doped nanoporous carbon for oxygen reduction reaction." Journal of the Taiwan Institute of Chemical Engineers **80**: 728-737.

Li, R., et al. (2015). "Nitrogen and phosphorus dual-doped graphene/carbon nanosheets as bifunctional electrocatalysts for oxygen reduction and evolution." Acs Catalysis **5**(7): 4133-4142.

Li, X., et al. (2021). "N, P co-doped porous carbon from cross-linking cyclophosphazene for high-performance supercapacitors." Journal of Electroanalytical Chemistry **881**: 114952.

Li, Z., et al. (2020). "Nitrogen, phosphorus and sulfur co-doped pyrolyzed bacterial cellulose nanofibers for supercapacitors." Nanomaterials **10**(10): 1912.

Lin, G., et al. (2018). "KOH activation of biomass-derived nitrogen-doped carbons for supercapacitor and electrocatalytic oxygen reduction." Electrochimica Acta **261**: 49-57.

Lin, Z., et al. (2011). "Superior capacitance of functionalized graphene." The Journal of Physical Chemistry C **115**(14): 7120-7125.

Liu, B., et al. (2017). "Oxygen and nitrogen co-doped porous carbon nanosheets derived from Perilla frutescens for high volumetric performance supercapacitors." Journal of power sources **341**: 309-317.

Liu, C., et al. (2010). "Graphene-based supercapacitor with an ultrahigh energy density." Nano letters **10**(12): 4863-4868.

Liu, J., et al. (2012). "Synthesis, characterization and curing properties of a novel cyclolinear phosphazene-based epoxy resin for halogen-free flame retardancy and high performance." RSC advances **2**(13): 5789-5799.

Liu, W., et al. (2018). "Polyphosphazene-derived heteroatoms-doped carbon materials for supercapacitor electrodes." Carbon **129**: 420-427.

Liu, Y., et al. (2019). "Nitrogen/sulfur dual-doped sponge-like porous carbon materials derived from pomelo peel synthesized at comparatively low temperatures for superior-performance supercapacitors." Journal of Electroanalytical Chemistry **847**: 113111.

Liu, Z., et al. (2008). "PEGylated nanographene oxide for delivery of water-insoluble cancer drugs." Journal of the American Chemical Society **130**(33): 10876-10877.

Liu, Z., et al. (2013). "Graphene covalently functionalized with poly (p-phenylenediamine) as high performance electrode material for supercapacitors." Journal of Materials Chemistry A **1**(10): 3454-3462.

Lobato, B., et al. (2017). "Capacitance and surface of carbons in supercapacitors." Carbon **122**: 434-445.

Lotsch, B. V. and W. Schnick (2007). "New light on an old story: formation of melam during thermal condensation of melamine." Chemistry–A European Journal **13**(17): 4956-4968.

Lu, C. H., et al. (2009). "A graphene platform for sensing biomolecules." Angewandte Chemie **121**(26): 4879-4881.

Ma, Y., et al. (2019). "Nitrogen, phosphorus co-doped carbon obtained from amino acid based resin xerogel as efficient electrode for supercapacitor." ACS Applied Energy Materials **3**(1): 957-969.

MacDonald, G. A., et al. (2012). "Electrical property heterogeneity at transparent conductive oxide/organic semiconductor interfaces: Mapping contact ohmicity using conducting-tip atomic force microscopy." ACS nano **6**(11): 9623-9636.

Maqsood, M. and G. Seide (2020). "Biodegradable flame retardants for biodegradable polymer." Biomolecules **10**(7): 1038.

Marcano, D. C., et al. (2010). "Improved synthesis of graphene oxide." ACS nano **4**(8): 4806-4814.

Mariappan, T. (2016). "Recent developments of intumescent fire protection coatings for structural steel: A review." Journal of fire sciences **34**(2): 120-163.

Meyer, J. C., et al. (2007). "The structure of suspended graphene sheets." Nature **446**(7131): 60-63.

Mizouchi, S., et al. (2015). "Exposure assessment of organophosphorus and organobromine flame retardants via indoor dust from elementary schools and domestic houses." Chemosphere **123**: 17-25.

Mo, Z., et al. (2012). "Controllable synthesis of functional nanocomposites: Covalently functionalize graphene sheets with biocompatible L-lysine." Applied Surface Science **258**(22): 8623-8628.

Momodu, D., et al. (2019). "Stable ionic-liquid-based symmetric supercapacitors from Capsicum seed-porous carbons." Journal of Electroanalytical Chemistry **838**: 119-128.

Obodo, R. M., et al. (2020). "8.0 MeV copper ion (Cu++) irradiation-induced effects on structural, electrical, optical and electrochemical properties of Co3O4-NiO-ZnO/GO nanowires." Materials Science for Energy Technologies **3**: 193-200.

Oliveira, A. E. F., et al. (2018). "Thermally reduced graphene oxide: synthesis, studies and characterization." Journal of Materials Science **53**(17): 12005-12015.

Ospina, M., et al. (2018). "Exposure to organophosphate flame retardant chemicals in the US general population: Data from the 2013–2014 National Health and Nutrition Examination Survey." Environment international **110**: 32-41.

Pan, T., et al. (2012). "Intrinsically Fluorescent Microspheres with Superior Thermal Stability and Broad Ultraviolet-Visible Absorption Based on Hybrid Polyphosphazene Material." Macromolecular Chemistry and Physics **213**(15): 1590-1595.

Pandolfo, A. G. and A. F. Hollenkamp (2006). "Carbon properties and their role in supercapacitors." Journal of power sources **157**(1): 11-27.

Panja, T., et al. (2015). "Nitrogen and phosphorus co-doped cubic ordered mesoporous carbon as a supercapacitor electrode material with extraordinary cyclic stability." Journal of Materials Chemistry A **3**(35): 18001-18009.

Pédrot, P.-M. and N. Tabareau (2020). "The Fire Triangle." Proceedings of the ACM on Programming Languages: 1-28.

Pimenta, M., et al. (2007). "Studying disorder in graphite-based systems by Raman spectroscopy." Physical chemistry chemical physics **9**(11): 1276-1290.

Pisarevskaya, E. Y., et al. (2017). "Studies of chemical stage of synthesis of electroactive composite based on poly-o-phenylenediamine and graphene oxide." Russian Journal of Electrochemistry **53**(1): 70-77.

Poonam, et al. (2019). "Review of supercapacitors: Materials and devices." Journal of Energy Storage **21**: 801-825.

Pu, L., et al. (2013). "Simple method for the fluorinated functionalization of graphene oxide." RSC advances **3**(12): 3881-3884.

Qi, F., et al. (2017). "Nitrogen/sulfur co-doping assisted chemical activation for synthesis of hierarchical porous carbon as an efficient electrode material for supercapacitors." Electrochimica Acta **246**: 59-67.

Qi, J., et al. (2013). "Graphite oxide-catalyzed esterification and transesterification." Chinese J. Org. Chem **33**: 1839-1846.

Qiao, X., et al. (2015). "Phosphorus and nitrogen dual doped and simultaneously reduced graphene oxide with high surface area as efficient metal-free electrocatalyst for oxygen reduction." Catalysts **5**(2): 981-991.

Qu, T., et al. (2017). "Flame retarding epoxy composites with poly (phosphazene-co-bisphenol A)-coated boron nitride to improve thermal conductivity and thermal stability." RSC advances **7**(10): 6140-6151.

Rajagopalan, B., et al. (2017). "Redox synthesis of poly (p–phenylenediamine)–reduced graphene oxide for the improvement of electrochemical performance of lithium titanate in lithium–ion battery anode." Journal of Alloys and Compounds **709**: 248-259.

Raza, W., et al. (2018). "Recent advancements in supercapacitor technology." Nano Energy **52**: 441-473.

Ren, G., et al. (2018). "Sepia-derived N, P co-doped porous carbon spheres as oxygen reduction reaction electrocatalyst and supercapacitor." ACS Sustainable Chemistry & Engineering **6**(12): 16032-16038.

Renner, J. S., et al. (2021). "Fire behavior of wood-based composite materials." Polymers **13**(24): 4352.

Rhili, K., et al. (2021). "Hexachlorocyclotriphosphazene functionalized graphene oxide as a highly efficient flame retardant." ACS omega **6**(9): 6252-6260.

Sadak, O., et al. (2018). "Facile and green synthesis of highly conducting graphene paper." Carbon **138**: 108-117.

Sahyoun, J. (2014). Développement de nouveaux matériaux polymères ignifugeants par la voie extrusion réactive, Université Claude Bernard-Lyon I.

Sai, T., et al. (2022). "Recent advances in fire-retardant carbon-based polymeric nanocomposites through fighting free radicals." SusMat **2**(4): 411-434.

Sevilla, M. and R. Mokaya (2014). "Energy storage applications of activated carbons: supercapacitors and hydrogen storage." Energy & Environmental Science **7**(4): 1250-1280.

Shao, Y. El− Kady, MF.

Sharma, P. and V. Kumar (2020). "Current Technology of Supercapacitors: A Review." Journal of Electronic Materials **49**(6): 3520-3532.

Shen, K., et al. (2015). "Supercapacitor electrodes based on nano-polyaniline deposited on hollow carbon spheres derived from cross-linked co-polymers." Synthetic Metals **209**: 369-376.

Shen, Z., et al. (2020). "Nitrogen-enriched hierarchically porous carbon sheets anchored with ZIF-derived carbon for supercapacitors." Applied Surface Science **527**: 146845.

Shieh, J. Y. and C. S. Wang (2002). "Effect of the organophosphate structure on the physical and flame-retardant properties of an epoxy resin." Journal of Polymer Science Part A: Polymer Chemistry **40**(3): 369-378.

Singler, R., et al. (1974). "Synthesis and characterization of polyaryloxyphosphazenes." Journal of Polymer Science: Polymer Chemistry Edition **12**(2): 433-444.

Sinha Ray, S. and M. Kuruma (2020). Polymer combustion and flame retardancy. Halogen-Free Flame-Retardant Polymers, Springer**:** 5-9.

Song, B., et al. (2016). "Molecular level study of graphene networks functionalized with phenylenediamine monomers for supercapacitor electrodes." Chemistry of Materials **28**(24): 9110-9121.

Song, Y., et al. (2016). "In-situ synthesis of graphene/nitrogen-doped ordered mesoporous carbon nanosheet for supercapacitor application." Carbon **96**: 955-964.

Sparavigna, A. C. (2018). "The Invention of Carborundum, the Synthetic Silicon Carbide." Philica.

Stankovich, S., et al. (2006). "Graphene-based composite materials." nature **442**(7100): 282.

Stankovich, S., et al. (2007). "Synthesis of graphene-based nanosheets via chemical reduction of exfoliated graphite oxide." carbon **45**(7): 1558-1565.

Staudenmaier, L. (1898). "Verfahren zur darstellung der graphitsäure." Berichte der deutschen chemischen Gesellschaft **31**(2): 1481-1487.

Stern, O. (1924). "The theory of the electrolytic double-layer." Z. Elektrochem **30**(508): 1014-1020.

Stoller, M. D. and R. S. Ruoff (2010). "Best practice methods for determining an electrode material's performance for ultracapacitors." Energy & Environmental Science **3**(9): 1294-1301.

Sun, Y., et al. (2020). "Biomass-derived porous carbon electrodes for high-performance supercapacitors." Journal of Materials Science **55**(12): 5166-5176.

Tang, J., et al. (2016). "Bimetallic metal-organic frameworks for controlled catalytic graphitization of nanoporous carbons." Scientific reports **6**(1): 30295.

Tian, W., et al. (2016). "Renewable graphene-like nitrogen-doped carbon nanosheets as supercapacitor electrodes with integrated high energy–power properties." Journal of Materials Chemistry A **4**(22): 8690-8699.

Tian, Z., et al. (2015). "Phosphazene high polymers and models with cyclic aliphatic side groups: new structure–property relationships." Macromolecules **48**(13): 4301-4311.

Tiwari, S. K., et al. (2016). "Magical allotropes of carbon: prospects and applications." Critical Reviews in Solid State and Materials Sciences **41**(4): 257-317.

Verma, S. and R. K. Dutta (2015). "A facile method of synthesizing ammonia modified graphene oxide for efficient removal of uranyl ions from aqueous medium." RSC advances **5**(94): 77192-77203.

Wallace, P. R. (1947). "The band theory of graphite." Physical review **71**(9): 622.

Wan, C. and X. Huang (2017). "Cyclomatrix polyphosphazenes frameworks (Cyclo-POPs) and the related nanomaterials: Synthesis, assembly and functionalisation." Materials Today Communications **11**: 38-60.

Wan, L., et al. (2020). "A novel strategy to prepare N, S-codoped porous carbons derived from barley with high surface area for supercapacitors." Applied Surface Science **518**: 146265.

Wang, B., et al. (2011). "Electron beam irradiation cross linking of halogen-free flame-retardant ethylene vinyl acetate (EVA) copolymer by silica gel microencapsulated ammonium polyphosphate and char-forming agent." Industrial & Engineering Chemistry Research **50**(9): 5596-5605.

Wang, C., et al. (2013). "P/N co-doped microporous carbons from H3PO4-doped polyaniline by in situ activation for supercapacitors." Carbon **59**: 537-546.

Wang, D., et al. (2016). "A melt route for the synthesis of activated carbon derived from carton box for high performance symmetric supercapacitor applications." Journal of Power Sources **307**: 401-409.

Wang, G., et al. (2012). "A review of electrode materials for electrochemical supercapacitors." Chemical Society Reviews **41**(2): 797-828.

Wang, H., et al. (2017). "Preparation and electrochemical performance of polyimide-based activated carbons with high surface area." JOURNAL OF INORGANIC MATERIALS-BEIJING- **32**(11): 1181-1187.

Wang, J. and S. Kaskel (2012). "KOH activation of carbon-based materials for energy storage." Journal of materials chemistry **22**(45): 23710-23725.

Wang, J., et al. (2019). "Enhancing the capacitance of battery-type hybrid capacitors by encapsulating MgO nanoparticles in porous carbon as reservoirs for OH–ions from electrolytes." ACS applied materials & interfaces **11**(24): 21567-21577.

Wang, X., et al. (2015). "Hollow polyphosphazene microspheres with cross-linked chemical structure: synthesis, formation mechanism and applications." RSC advances **5**(43): 33720-33728.

Wang, X., et al. (2014). "Heteroatom-doped graphene materials: syntheses, properties and applications." Chemical Society Reviews **43**(20): 7067-7098.

Wang, Y., et al. (2019). "N-doped porous hard-carbon derived from recycled separators for efficient lithium-ion and sodium-ion batteries." Sustainable energy & fuels **3**(3): 717-722.

Wang, Y., et al. (2011). "Graphene and graphene oxide: biofunctionalization and applications in biotechnology." Trends in Biotechnology **29**(5): 205-212.

Wang, Y. and Y. Xia (2013). "Recent progress in supercapacitors: from materials design to system construction." Advanced materials **25**(37): 5336-5342.

Wang, Y., et al. (2017). "p-Phenylenediamine strengthened graphene oxide for the fabrication of superhydrophobic surface." Materials & Design **127**: 22-29.

Wei, D., et al. (2009). "Synthesis of N-doped graphene by chemical vapor deposition and its electrical properties." Nano letters **9**(5): 1752-1758.

Wei, J., et al. (2013). "A controllable synthesis of rich nitrogen-doped ordered mesoporous carbon for CO2 capture and supercapacitors." Advanced Functional Materials **23**(18): 2322-2328.

Wilkie, C. A. and A. B. Morgan (2009). Fire retardancy of polymeric materials, CRC press.

Willfahrt, A., et al. (2019). "Printable acid-modified corn starch as non-toxic, disposable hydrogel-polymer electrolyte in supercapacitors." Applied Physics A **125**(7): 1-10.

William, S., et al. (1958). "Preparation of graphitic oxide." J. Am. Chem. Soc **80**(6): 1339-1339.

Wisian-Neilson, P., et al. (1994). Inorganic and organometallic polymers II, ACS.

Wu, G., et al. (2016). "Carbon nanocomposite catalysts for oxygen reduction and evolution reactions: From nitrogen doping to transition-metal addition." Nano Energy **29**: 83-110.

Xia, J., et al. (2009). "Measurement of the quantum capacitance of graphene." Nature nanotechnology **4**(8): 505-509.

Xia, K., et al. (2017). "Facile and controllable synthesis of N/P co-doped graphene for high-performance supercapacitors." Journal of power sources **365**: 380-388.

Xiang, Z., et al. (2014). "Nitrogen-doped holey graphitic carbon from 2D covalent organic polymers for oxygen reduction." Advanced materials **26**(20): 3315-3320.

Xu, F., et al. (2011). "Fast ion transport and high capacitance of polystyrene-based hierarchical porous carbon electrode material for supercapacitors." Journal of Materials Chemistry **21**(6): 1970-1976.

Xu, K., et al. (2018). "Hierarchical hollow MnO2 nanofibers with enhanced supercapacitor performance." Journal of colloid and interface science **513**: 448-454.

Xue, D., et al. (2019). "Template-free, self-doped approach to porous carbon spheres with high N/O contents for high-performance supercapacitors." ACS Sustainable Chemistry & Engineering **7**(7): 7024-7034.

Yang, D.-S., et al. (2012). "Phosphorus-doped ordered mesoporous carbons with different lengths as efficient metal-free electrocatalysts for oxygen reduction reaction in alkaline media." Journal of the American Chemical Society **134**(39): 16127-16130.

Yang, J., et al. (2018). "p-Phenylenediamine Functionalization Induced 3D Microstructure Formation of Reduced Graphene Oxide for the Improved Electrical double Layer Capacitance in Organic Electrolyte." ChemistrySelect **3**(27): 7680-7688.

Yang, S., et al. (2012). "Efficient synthesis of heteroatom (N or S)-doped graphene based on ultrathin graphene oxide-porous silica sheets for oxygen reduction reactions." Advanced Functional Materials **22**(17): 3634-3640.

Yang, X., et al. (2008). "High-efficiency loading and controlled release of doxorubicin hydrochloride on graphene oxide." The Journal of Physical Chemistry C **112**(45): 17554-17558.

Yang, Z.-G., et al. (2019). "Supercapacitors based on free-standing reduced graphene oxides/carbon nanotubes hybrid films." SN Applied Sciences **1**(1): 1-9.

Yanilmaz, A., et al. (2017). "Nitrogen doping for facile and effective modification of graphene surfaces." RSC advances **7**(45): 28383-28392.

Yeşilot, S. and A. Uslu (2017). "Stereochemical Aspects of Polyphosphazenes." Polymer Reviews **57**(2): 213-247.

Yuan, B., et al. (2014). "Preparation of functionalized graphene oxide/polypropylene nanocomposite with significantly improved thermal stability and studies on the crystallization behavior and mechanical properties." Chemical Engineering Journal **237**: 411-420.

Yuan, B., et al. (2017). "Dual modification of graphene by polymeric flame retardant and Ni (OH) 2 nanosheets for improving flame retardancy of polypropylene." Composites Part A: Applied Science and Manufacturing **100**: 106-117.

Zeng, T., et al. (2021). "Nitrogen/phosphorus co-doped porous carbon materials for supercapacitor electrodes." New Journal of Chemistry **45**(16): 7239-7246.

Zhang, H., et al. (2019). "Facile preparation of three-dimensional honeycomb nitrogen-doped carbon materials for supercapacitor applications." Journal of Materials Research **34**(7): 1200-1209.

Zhang, J., et al. (2012). "Preparation of activated carbon from waste Camellia oleifera shell for supercapacitor application." Journal of Solid State Electrochemistry **16**(6): 2179-2186.

Zhang, J., et al. (2011). "Synthesis and capacitive properties of manganese oxide nanosheets dispersed on functionalized graphene sheets." The Journal of Physical Chemistry C **115**(14): 6448-6454.

Zhang, J., et al. (2011). Electrochemical Technologies for Energy Storage and Conversion, 2 Volume Set, John Wiley & Sons.

Zhang, L. L. and X. Zhao (2009). "Carbon-based materials as supercapacitor electrodes." Chemical Society Reviews **38**(9): 2520-2531.

Zhang, L. L. and X. S. Zhao (2009). "Carbon-based materials as supercapacitor electrodes." Chemical Society Reviews **38**(9): 2520-2531.

Zhang, M., et al. (2018). "Synthesis of microporous covalent phosphazene-based frameworks for selective separation of uranium in highly acidic media based on size-matching effect." ACS applied materials & interfaces **10**(34): 28936-28947.

Zhang, P., et al. (2019). "Covalently functionalized graphene towards molecular-level dispersed waterborne polyurethane nanocomposite with balanced comprehensive performance." Applied Surface Science **471**: 595-606.

Zhang, S., et al. (2016). "Preparation of poly (bis (phenoxy) phosphazene) and 31P NMR analysis of its structural defects under various synthesis conditions." The Journal of Physical Chemistry B **120**(43): 11307-11316.

Zhang, S., et al. (2016). ""Stereoscopic" 2D super-microporous phosphazene-based covalent organic framework: design, synthesis and selective sorption towards uranium at high acidic condition." Journal of hazardous materials **314**: 95-104.

Zhang, T., et al. (2005). "Phosphazene cyclomatrix network polymers: Some aspects of the synthesis, characterization, and flame-retardant mechanisms of polymer." Journal of applied polymer science **95**(4): 880-889.

Zhang, X., et al. (2014). "Grafting of amine-capped cross-linked polyphosphazenes onto carbon fiber surfaces: A novel coupling agent for fiber reinforced composites." RSC advances **4**(24): 12198-12205.

Zhang, X., et al. (2018). "Mechanically robust and highly compressible electrochemical supercapacitors from nitrogen-doped carbon aerogels." Carbon **127**: 236-244.

Zhang, Y., et al. (2009). "Progress of electrochemical capacitor electrode materials: A review." International Journal of Hydrogen Energy **34**(11): 4889-4899.

Zhang, Y., et al. (2019). "Facile synthesis of hierarchically porous N/P codoped carbon with simultaneously high-level heteroatom-doping and moderate porosity for high-performance supercapacitor electrodes." ACS Sustainable Chemistry & Engineering **7**(6): 5717-5726.

Zhang, Z. P., et al. (2018). "Polymer engineering based on reversible covalent chemistry: A promising innovative pathway towards new materials and new functionalities." Progress in Polymer Science **80**: 39-93.

Zhao, X., et al. (2021). "Behavior and mechanism of graphene oxide-tris (4-aminophenyl) amine composites in adsorption of rare earth elements." Journal of Rare Earths **39**(1): 90-97.

Zhao, X., et al. (2017). "Nitrogen and phosphorus dual-doped hierarchical porous carbon with excellent supercapacitance performance." Electrochimica Acta **247**: 1140-1146.

Zheng, L., et al. (2020). "High-yield synthesis of N-rich polymer-derived porous carbon with nanorod-like structure and ultrahigh N-doped content for high-performance supercapacitors." Chemical Engineering Journal **399**: 125671.

Zhong, C., et al. (2015). "Preparation of nitrogen-doped pitch-based carbon materials for supercapacitors." Materials Letters **156**: 1-6.

Zhou, J., et al. (2020). "Nitrogen and phosphorus co-doped porous carbon for high-performance supercapacitors." Frontiers in chemistry **8**: 105.

Zhou, M., et al. (2020). "Data-driven approach to understanding the in-operando performance of heteroatom-doped carbon electrodes." ACS Applied Energy Materials **3**(6): 5993-6000.

Zhou, X., et al. (2020). "Polyphosphazenes-based flame retardants: A review." Composites Part B: Engineering **202**: 108397.

Zhu, L., et al. (2007). "Fully crosslinked poly [cyclotriphosphazene-co-(4, 4′-sulfonyldiphenol)] microspheres via precipitation polymerization and their superior thermal properties." Macromolecular Reaction Engineering **1**(1): 45-52.

Zou, W., et al. (2020). "Structurally designed heterochain polymer derived porous carbons with high surface area for high-performance supercapacitors." Applied Surface Science **530**: 147296.

Zou, Y., et al. (2016). "Structure of functionalized nitrogen-doped graphene hydrogels derived from isomers of phenylenediamine and graphene oxide based on their high electrochemical performance." Electrochimica Acta **212**: 828-838.